Dissertation
submitted to the
Combined Faculties for the Natural Sciences and for Mathematics
of the Ruperto-Carola University of Heidelberg, Germany
for the degree of
Doctor of Natural Sciences

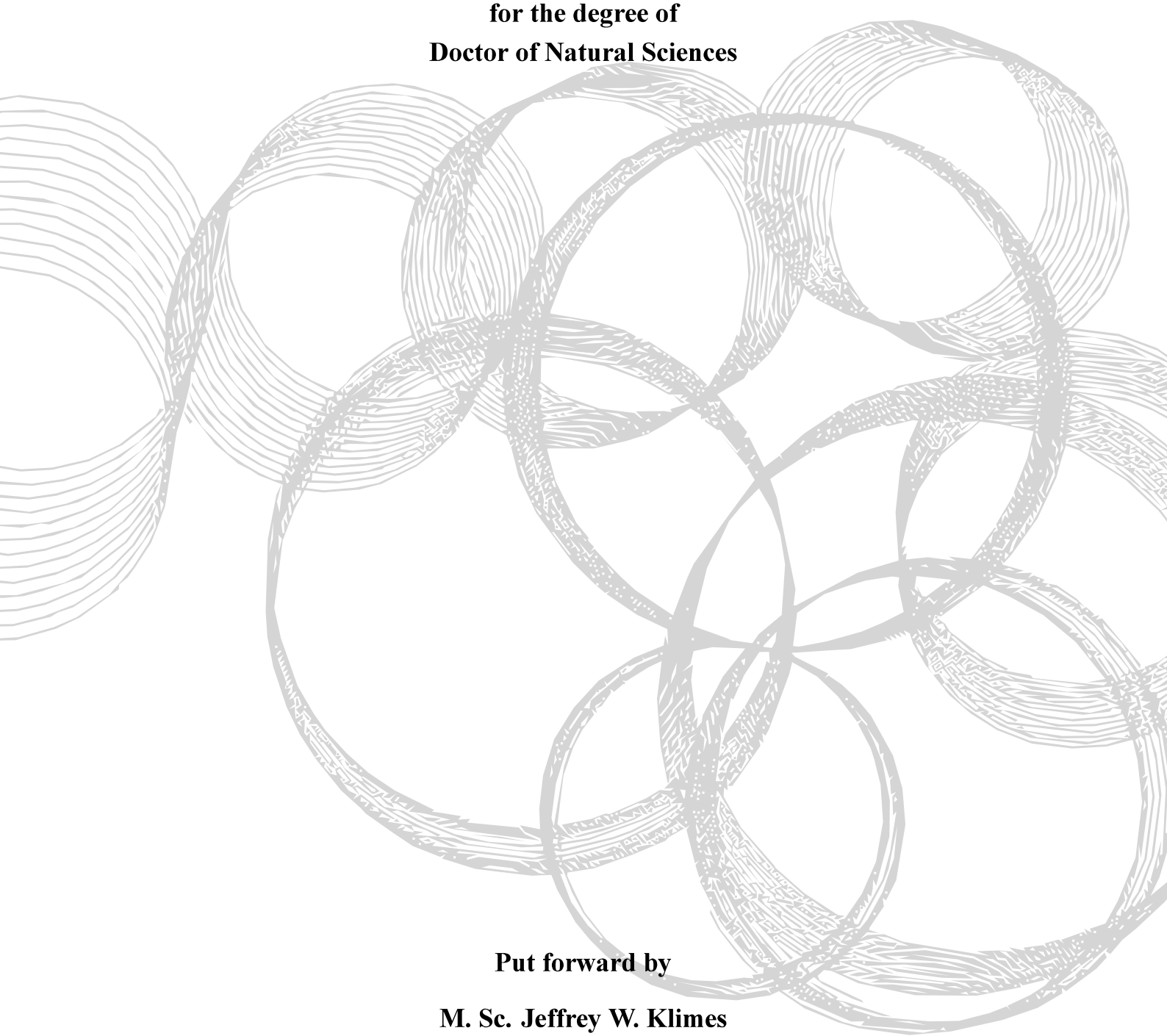

Put forward by

M. Sc. Jeffrey W. Klimes

Born in Indianapolis, IN, USA

Oral examination: 10.05.2023

Injection of Highly Charged Ion Ensembles for Spectroscopy of Magnetic Interactions in the ARTEMIS Penning Trap

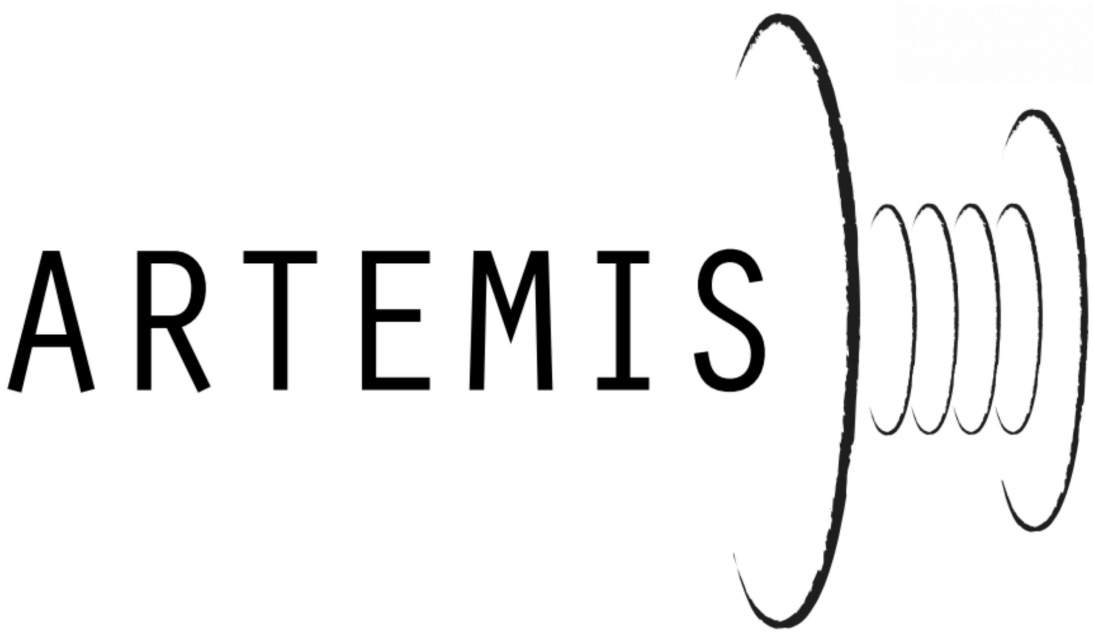

Referees: **Priv.-Doz. Dr. Wolfgang Quint**
apl. Prof. Dr. Yuri Litvinov

Injektion von Ensembles hochgeladener Ionen für spektroskopische Messungen magnetischer Wechselwirkungen in der ARTEMIS-Penningfalle

Die Quantenelektrodynamik (QED) ist die genaueste geprüfte Theorie der modernen Physik, ist aber in den extremsten Feldern weitgehend ungetestet. Atomkerne schwerer Atome bieten den Vorteil, dass sie stärkere elektromagnetische Felder erzeugen als es mit den modernsten und leistungsstärksten Magneten und Lasern heutzutage möglich ist. Daher bieten sich schwere, hochgeladene Ionen (HCIs) für die QED-Forschung mit starken Feldern an. ARTEMIS ist ein Penningfallen-Experiment zur Messung der magnetischer Momente von Elektronen und Kernen in schweren HCIs mittels Laser-Mikrowellen-Doppelresonanzspektroskopie (LMDR). Diese Technik ermöglicht die Messung magnetischer Momente in atomaren Systemen mit Hyperfeinstruktur, bei denen die Übergänge häufig im nahen Ultraviolett (UV) liegen, wie z. B. bei wasserstoffähnlichem Bismut, $^{209}Bi^{82+}$. Die Präzisionsspektroskopie solcher schweren HCIs erfordert extrem gute Vakuumbedingungen im Fallenbereich mit Drücken unter 10^{-15} mbar. In dieser Arbeit wird die Implementierung einer Ionenfalle vorgestellt, die schwere HCIs langfristig speichern kann, sowie das Design und die Konstruktion der dazugehörigen Injektionsstrahllinie. Die Ionenfalle is die erste die einen Restgasdruck von besser als $2,4 \text{x} 10^{-16}$ mbar hat und schnelle Zykluszeiten von 100 ms für die Bestrahlung mit UV-Laserlicht ermöglicht. Die guten Vakuumbedingungen im Fallenbereich wurde durch eine zerstörungsfreie Überwachung gespeicherter HCIs über einige Tage hinweg verifiziert, die letztendlich für etwa 2 Wochen gespeichert werden konnten. Der Betrieb eines solchen schnell öffnenden Kaltventils ist essentiell für die LMDR-Technik für viele Schwerionensysteme, in dem ausgezeichnete Umgebungsbedingungen im Einfangbereich und eine direkte Sichtlinie für die Laserbestrahlung erforderlich.

Injection of Highly Charged Ion Ensembles for Spectroscopy of Magnetic Interactions in the ARTEMIS Penning Trap

Quantum electrodynamics (QED) is the most precisely validated theory in modern physics, yet it remains mostly untested in the most extreme fields. In addition, atomic nuclei generate fields much stronger than can be made in even the most advanced laser and magnet facilities. Therefore, heavy highly charged ions (HCIs) present themselves as natural laboratories for investigating QED in strong fields. ARTEMIS is a Penning trap experiment designed for measurement of electron and nuclear magnetic moments in heavy HCIs using laser-microwave double-resonance (LMDR) spectroscopy. This technique enables measurement of magnetic moments in atomic systems with hyperfine structure, in which the transitions are often in the near ultraviolet (UV) regime such as hydrogenlike bismuth, $^{209}Bi^{82+}$. Precision spectroscopy of such heavy, HCIs requires an exceedingly well isolated trapping environment with vacuum pressure better than 10^{-15} mbar. This work presents the implementation of the first ion trap capable of long-term storage of heavy HCIs with a residual gas pressure better than $2.4x10^{-16}$ mbar and with rapid cycle times as fast as 100 ms for irradiation with UV laser light, as well as the design of the corresponding injection beamline. The trapping conditions are verified by non-destructive monitoring of trapped HCIs over a few days, which were ultimately stored for about 2 weeks. The operation of such a fast-opening cryogenic valve (FCV) is essential to the LMDR technique for many heavy ion systems where excellent environmental conditions in the trapping region and direct line of sight for laser irradiation are required.

Title page image: A stylized drawing of multiple charges executing the motion in a Penning trap.

Contents

Chapter 1

Introduction

In reference to the contemporary successes of quantum electrodynamics (QED), Richard Feynman called it 'the jewel of physics - our proudest possession' [1]. QED, at its most basic level, describes the fundamental interactions between light, and electrons. It stands today as one of the most rigorously proven domains of modern physics [2]. Nonetheless, QED still holds interesting mysteries about this fundamental interaction of nature, as was recently demonstrated in 2016 in the observation of light-by-light scattering at the ATLAS detector [3].

One specific manifestation of the interaction between electrons and light is the magnetic moment of the electron, the fundamental magnetic field that it generates. In the early twentieth century, before QED, the electron was hypothesized to have an intrinsic angular momentum with two possible values [4, 5]. This was demonstrated by Alfred Landé in his account of spectral lines of electrons in atoms by spin-orbit coupling [6] and Wolfgang Pauli by finalizing the role of the electron spin in describing the occupancy of electrons in atomic shells [7]. However, the semi-classical picture of the magnetic moment arising from this quantum spin of a fundamental charge interacting with the classical electromagnetic field could not explain the measured strength of the interaction.

The connection between the electron's magnetic moment and its angular momentum was explained theoretically by Paul Dirac in 1928 with the introduction of a relativistic form of the Schrödinger equation with conserved probability current [8]. This new theory was the first description of the time evolution of a four component vector field, a major shift in the understanding of quantum mechanics that can only be fully appreciated in hindsight. It naturally gives rise to the electron spin and predicts the existence of positrons. Moreover, when coupled to the electromagnetic field by the charge of the electron, it predicts the so-called g-factor or gyromagnetic ratio, the first theoretical prediction of the free electron's magnetic moment, $g_s = 2$.

Development of QED would come with the inclusion of vacuum fluctuations and renormalization of higher-order perturbative terms, which would yield explanations for the Lamb shift of the 1s state in Hydrogen [9], the first prediction of QED. The complete description of the QED Lagrangian includes the Dirac and electromagnetic fields as well as their interactions and gauge invariance. QED would become the model quantum field theory for quantum chromodynamics, electroweak theory, and ultimately a critical component of the standard model. Despite its success QED still lacks much verifying experimentation in the high field regime [10–12].

On the precision frontier in QED, measurements of magnetic moments are currently the best effects for experimental investigation. Heavy, highly charged ions provide excellent candidates for extending these precision measurements into the high field regime, where the field strengths reach above 10^{16} Vcm^{-1} and 10^{7} T . The current values for the measured and predicted g-factors are presented below for the free electron as well as the 1s state in Hydrogenlike Bismuth [2, 13–15].

$$g_{ex}(free) = 2.00231930436118(13) \qquad g_{ex}(\mathrm{Bi}^{82+}) = 1.7294(40)$$
$$g_{th}(free) = 2.00231930436406(144) \qquad g_{th}(\mathrm{Bi}^{82+}) = 1.731014(1)$$

There are two major techniques for studying magnetic moments of bound systems, the continuous Stern-Gerlach method [16] and laser-microwave double-resonance spectroscopy, which has yet to be completely implemented for precision microwave spectroscopy on bound systems [17]. These combine the proven high sensitivity of magnetic moment measurements in a precision Penning trap with the field strength of the atomic nucleus to improve understanding of QED in extreme fields. Determination of the strength of the magnetic interaction comes from measurement of the transition between spin states of the bound electron in the presence of an external magnetic field. Both techniques utilize sensitive detection of the alternating current induced by the ion as it passes near the trap electrodes, but where the continuous Stern-Gerlach method maps changes in the electron spin to this motion directly, the double-resonance method maps the transition to the luminous intensity of a closed cycle of the hyperfine structure. The double-resonance technique thus enables the measurement of magnetic moments of electrons bound to atomic nuclei with non-zero spin, and uniquely the magnetic moments of the nuclei themselves as well.

The main challenge of such experiments is to produce and maintain the requisite environment for high precision measurements of highly charged ions. This requires excellent rejection of interference from the external environment, cryogenic conditions of the ion trap and its nearby electronics, and vacuum pressures on the order of 10^{-15} mbar or lower.

This is on top of the already great task of producing such ionic systems to begin with, which is currently only possible in large accelerator facilities at a significant fraction of the speed of light for the highest charge states. ARTEMIS is a precision experiment for measuring the magnetic moments of electrons and nuclei in heavy, highly charged ions, by the laser-microwave double-resonance method. The experiment implements a novel trap design for improved performance of the laser spectroscopy measurement [18], as well as a new fast-opening cryogenic valve that enables the laser spectroscopy measurement with ultraviolet light and ion injection while maintaining the environmental isolation of the trap.

The experiment is currently in its commissioning phase. It has recently been upgraded to allow injection of heavy, highly charged ions from the HITRAP low-energy beamline and is working toward measurement of the magnetic moments of the hyperfine states of hydrogenlike Bismuth. In this work the theory of magnetic moments of electrons bound to highly charged nuclei will be presented as well as a method for their measurement in a precision Penning trap using laser microwave double-resonance spectroscopy. The main contribution is the implementation of the injection beamline. A complete description of its design parameters is given as well as proposals for future work to further improve its function. Analysis of ions stored in ARTEMIS is used to characterize the requisite and achieved conditions inside the trap environment.

Chapter 2

Tests of QED with Heavy, Highly Charged Ions in Penning Traps

Measurements of particles' magnetic moments are still some of the most precise probes of the standard model or for physics beyond the standard model. QED and the standard model can be used to predict deviations from the Dirac value caused by interactions with the quantum vacuum to some 11 digits of precision [14, 19], and experimental uncertainties are even smaller [20]. When paired with the strong fields of atomic nuclei, predictions can be extended to include interactions with these fields, as well as the complex interaction with the orbital angular momenta of the bound electrons, fundamental constants such as the fine structure constant and the electron mass, and even nuclear properties that can constrain nuclear structure models. The most precise determinations of magnetic moments are performed in Penning trap experiments which can exert precise limits on the influence of measurement systematics. This chapter will introduce all of the requisite theory that will be used in the remainder of the text including calculation of particle magnetic moments within QED, the principle of their measurement, and the operation of Penning traps and their associated injection beamlines.

2.1 Magnetic moment of the free electron

The g-factor for free electron, g_s can be formally written as

$$\frac{\boldsymbol{\mu}}{\mu_b} = -g_s \frac{\boldsymbol{S}}{\hbar}, \tag{2.1}$$

where $\boldsymbol{\mu}$ is the electron's magnetic moment, $\boldsymbol{S}$ is its angular momentum, and $\hbar$ is the reduced Planck constant.

$$\mu_b = \frac{e\hbar}{2m_e} = 9.274\,010\,078\,3(28) \times 10^{-24}\,\frac{J}{T} \tag{2.2}$$

is the Bohr magneton, where e and m_e are the charge and mass of the electron respectively; it is the magnetic dipole moment generated by an electron in orbit in Bohr's atomic model.

Within the standard model the corrections to the Dirac value can be predicted by perturbative treatment of the free electron's interactions with the quantum vacuum. These collectively are referred to as the anomalous magnetic moment of the free electron, a.

$$a = \frac{g_s - 2}{2} = a_{QED} + a_{Hadronic} + a_{Weak} \tag{2.3}$$

Contributions from the QCD and weak sectors of the standard model are predicted to be less than 2 ppt [21]. QED corrections dominate at more than 0.1% and are calculated according to expansion over all relevant interactions between the electrons and the electromagnetic field at the specified order of the fine structure constant, $\alpha \approx 1/137$, where each coefficient is determined by the method of Feynman diagrams.

$$\begin{aligned} a_{QED} &= \sum_{i=1}^{\infty} C_{2i}\left(\frac{\alpha}{\pi}\right)^i, \\ C_{2i} &= a_{2i} + b_{2i}\left(\frac{m_e}{m_\mu}\right) + c_{2i}\left(\frac{m_e}{m_\tau}\right) + d_{2i}\left(\frac{m_e}{m_\mu}, \frac{m_e}{m_\tau}\right) \end{aligned} \tag{2.4}$$

As QED describes the interactions between all leptons and light, contributions with virtual mu- and tau-lepton loops, coefficients b_{2i} and c_{2i}, occur fourth order on, and contributions with both, d_{2i}, from sixth. These interactions are scaled by the relative masses of the heavier leptons, and therefore highly suppressed in electron magnetic moment interactions.

The leading correction, $O(\alpha)$, was calculated by Julian Schwinger in 1948 as $C_2 = 0.5$ [23]. The single Feynman diagram for the second order self-energy correction is shown in figure 2.1. Higher order terms can be considered in the same manner, but the number of diagrams at each order grows rapidly. Table 2.1 shows the number of terms in each order up to C_{10}, which is the highest order calculated so far using numerical methods [19]. Currently, the precision of the calculation is limited by the precision of α[1].

[1] $\alpha = 7.297\,352\,569\,3(11) \times 10^{-3}$ is the currently accepted value of the fine structure constant. $\frac{\delta\alpha}{\alpha} = 1.5\times 10^{-10}$ [24]

Table 2.1: Comparison of the number of terms at each order of perturbation in the QED calculation of the g-factor for free and bound electrons [22]. The number of diagrams in the bound state case depends on the specific atomic system, and is dominated by other uncertainties already at third order.

Order	Number of diagrams	
	Free electron	Bound electron
0	1	1
1	1	6
2	7	>50
3	72	?
4	891	?
5	12 672	?
	...	

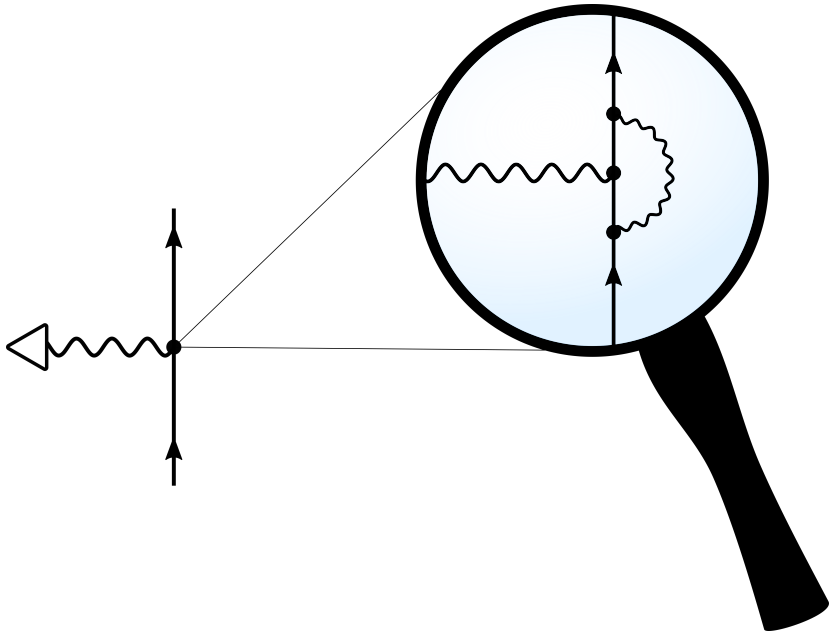

Figure 2.1: The Feynman diagram representing a free electron interacting with an external magnetic field (black triangle). This is the Dirac value, which upon closer inspection reveals a more complex interaction with the emission and reabsorption of a virtual photon. This is the Schwinger term.

2.2 Magnetic Moments in Heavy, Highly Charged Ions

Electrons bound in atomic systems undergo interaction with light in the presence of the strong fields generated by the nearby atomic nucleus. In particular, the field strengths in heavy, highly charged ions (HCIs) such as U^{92+} can reach as high as $E \approx 2 \cdot 10^{19}$ V/cm at the nuclear surface [25]. Figure 2.2 shows the radial probability distribution of the 1s electron in Hydrogenlike ions (ions with one electron) compared to the nuclear coulomb potential, both scaled to the nuclear charge, Z. For Z above Pb^{81+}, these field strengths are on the order of the Schwinger limit, beyond which spontaneous creation of electron-positron pairs and therefore nonlinear electromagnetic effects are anticipated [10]. Moreover, precise measurements in the absence of shielding electrons in these HCI systems place stringent limits on QED in high fields. Increasing interest in the physics of electrons in the most extreme field strengths has pushed recent measurements toward higher Z, but more evidence is needed to fully understand these effects.

Additionally, the bound electron's intrinsic angular momentum may increase due to its orbit about the nucleus. Such a bound electron has total angular momentum, $\boldsymbol{j} = \boldsymbol{l} + \boldsymbol{s}$, where $\boldsymbol{l}$ is its orbital angular momentum and $\boldsymbol{s}$ its spin, each a vector quantity. Therefore, total angular momentum projects onto the external magnetic field axis as 2j+1 quantized values. The is the anomalous Zeeman effect. The Landé g-factor describes the ratio of the magnetic moment of this combined spin-orbit system to its total angular momentum:

$$g_j = g_l \frac{j(j+1) - s(s+1) + l(l+1)}{2j(j+1)} + g_s \frac{j(j+1) + s(s+1) - l(l+1)}{2j(j+1)}. \tag{2.5}$$

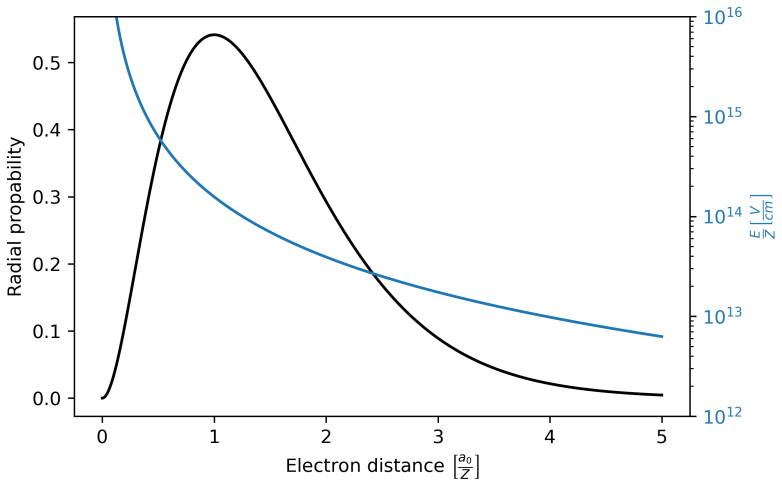

Figure 2.2: The radial probability distribution of the 1s electron in hydrogenlike ions (black) is compared to the distribution of the E field strength of the nuclear potential (blue).

The individual components g_l and g_s cannot be determined separately outside of the most extreme external magnetic fields where electron spin and orbit decouple.

Interactions in the bound case are significantly more complex, and additional corrections must be considered as outlined in equation 2.6. An explanation of each term is given below. Additionally, the coupling strength of the interaction between the bound electron and the electromagnetic field is proportional to the nuclear charge; therefore, for ions with $Z \ll 137$ the perturbative treatment of QED remains valid, if more complicated. However, the heaviest ions require non-perturbative methods for calculation of the interaction with the nuclear potential. The study of such interactions is the focus of bound-state quantum electrodynamics (BS-QED) and detailed explanations of the calculation methods and recent status can be found in [21, 22, 26–32] as well as references therein. Predictions from BS-QED calculations at the level of precision of experiments are extraordinary undertakings, and many of these authors introduce novel methods of calculation for the various contributions. An attempt is made to describe the relative contribution of these corrections, often in terms of the relative order of the interactions $O(\alpha Z)$, however as noted this will not always be a reliable metric, given the complexity of high-Z calculations. Equations in this section use $\hbar = c = m_e = 1$ unless otherwise specified.

$$g_j = g_D + \Delta g_{QED} + \Delta g_{elec} + \Delta g_{nucl} \tag{2.6}$$

g_D The parallel to the Dirac term of the free electron, but where the interaction takes place within the coulomb potential of the nucleus. For the 1s electron:

$$g_D(Z) = \frac{2}{3}\left(1 + 2\sqrt{1-(\alpha Z)^2}\right) \tag{2.7}$$

Δg_{QED} These are the corrections according to expansion over all relevant interactions, as in the case of the free electron. However, two complications exacerbate the calculation compared to the free electron. First, as the electron propagates in the vicinity of the nucleus they interact continuously. This interaction can be treated perturbatively by expanding the propagator term over $Z\alpha$ for $Z \ll 137$. Otherwise the full form of the propagator must be determined for a given form of the nuclear potential. Second, such a treatment of the bound state propagator causes the vacuum polarization and leg corrections to have non-vanishing contributions where they otherwise were vanishing at the same order in the free electron. For example at $O(\alpha)$ there are now six relevant diagrams as opposed to one (see table 2.1). Figure 2.3 summarizes both effects in the scheme of Feynman diagrams. Diagrammatically here the bound state propagator is represented by a double line.

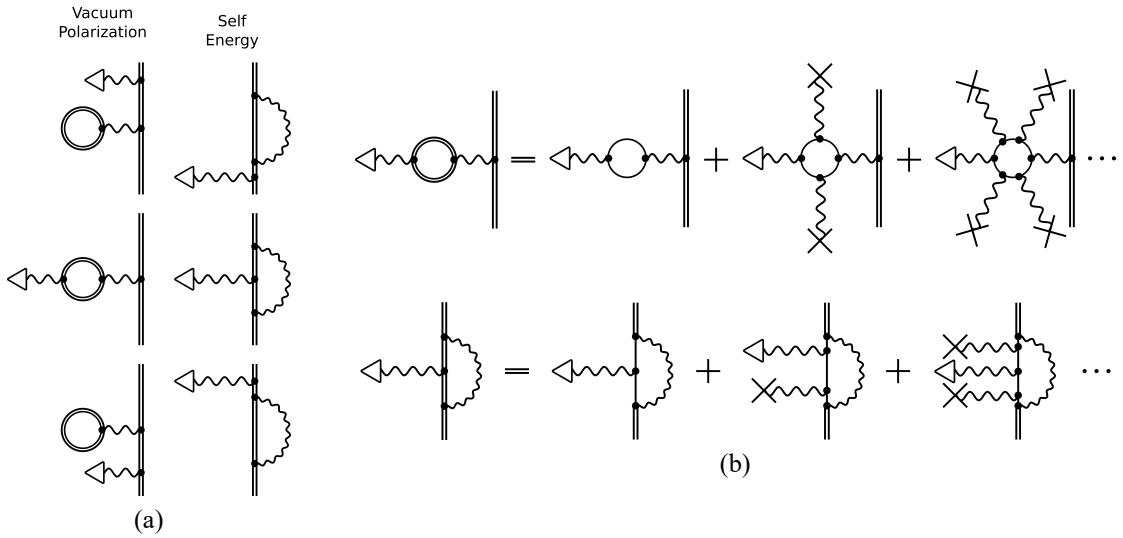

Figure 2.3: (a) The 6 Feynman diagrams representing the interactions of the bound electron with an external magnetic field at order $O(\alpha)$. (b) Diagrammatic example of perturbative $Z\alpha$ expansion for two of the one-loop interactions.

Δg_{elec} This correction arises from the presence of additional electrons within the atomic system. Perturbative treatment involves diagrams with interacting bound electrons as in figure 2.4a. These corrections appear at order $(\alpha Z)^2/Z^n$, where n is the number of exchanged photons. For light to medium mass lithium- and boronlike ions, with 3 or 5 bound electrons respectively, it can be as high as 0.1%. Thus its uncertainty must be well controlled for investigation of nuclear and QED effects in these systems. In addition, the exchanged photons or other electrons may participate in vacuum polarization or self energy interactions. These are typically refereed as screened QED effects. Some of the two-electron one-loop terms are presented in figure 2.4b. Non-perturbatively the effective potential can be constructed to account for the potential of the other electrons. Since this effective potential is a result of the presence of electrons, its corresponding field for the screening electrons must itself be a valid solution to the resulting Dirac equation. In practice this can be achieved iteratively [21, 33].

Δg_{nucl} The nuclear corrections account for the earlier simplification of the nuclear potential or other interactions that involve the nucleus. These can be further divided into 4 effects: nuclear size, nuclear recoil, nuclear polarization, and nuclear deformation.

Nuclear Size accounts for the non-pointlike distribution of the nuclear potential. Generally, experimental data is used to estimate the root-mean-square radius of the charge distribution of a nucleus which then gives the nuclear size correction. Equation 2.8 gives the simplest form of this correction for the 1s electron. It is currently

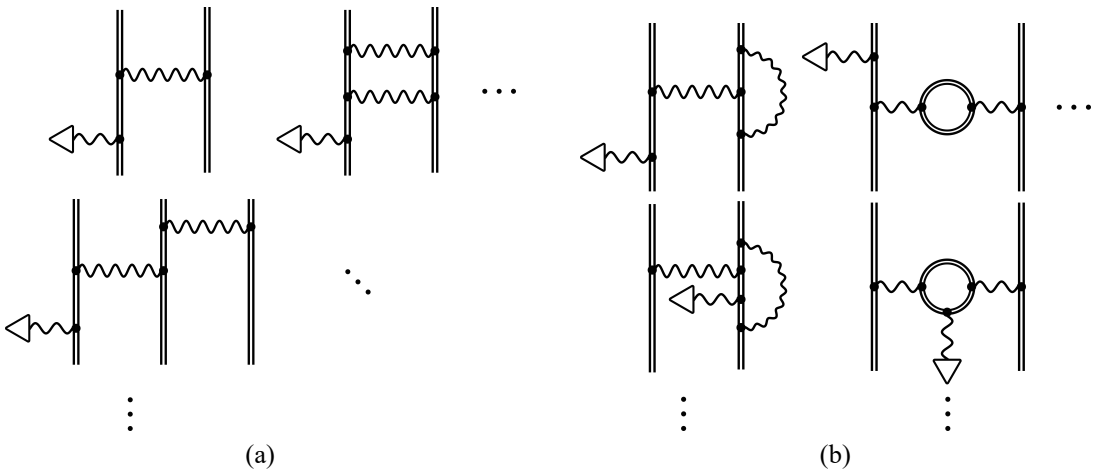

Figure 2.4: (a) Feynman diagrams representing the expansion over increasing number of electrons and increasing order in $Z\alpha$ (b) Feynman diagrams representing screened QED effects.

the dominant uncertainty for *ab initio* calculations of bound state g-factors in heavy ions [21]. However, [27] introduces the concept of the specific difference g-factor calculation. Enhanced precision for comparison with experiments can be obtained for the difference in g-factor of hydrogenlike and lithiumlike ions of the same isotope.

$$\Delta g_{ns}(1s) = \frac{8}{3}(\alpha Z)^4 \langle r^2 \rangle \tag{2.8}$$

Nuclear Recoil is the correction for the motion of the nucleus relative to the electron due to its finite mass. The leading order correction for the 1s electron is given in equation 2.9. Non-perturbative treatment is detailed in [28] where low-order terms of m_e/M, with nuclear mass M, are considered analytically and higher order numerically. The nuclear recoil effect has been precisely calculated to a few ppb which enables precise determination of the electron mass from g-factor measurements.

$$\Delta g_{nr}^{l.o.}(1s) = \frac{m_e}{M}(\alpha Z)^2 - \frac{m_e}{M}\frac{(\alpha Z)^4}{3[1+\sqrt{1-(\alpha Z)^2}]^2} \tag{2.9}$$

Nuclear Polarization involves the excitation of the nucleus by electromagnetic coupling to the bound electrons as in figure 2.5a. For multi-electron systems this can include screened nuclear polarization effects as in figure 2.5b. Nuclear polarization corrections are on the order of 100 ppb for heavy ions, and screened effects about 1 ppb. Additionally, interactions between the nucleus and the external mag-

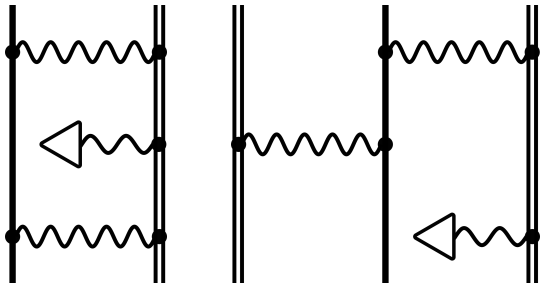

Figure 2.5: Feynman diagrams representing the nuclear polarization (a) and screened nuclear polarization effects (b). The solid black line indicates the nucleus.

netic field or that of the electron can induce nuclear polarization. Such interactions are referred to as nuclear magnetic susceptibility corrections. Note that these interactions are similar to but subtly distinct from the electron binding and hyperfine interactions. The description of the nuclear dynamics used in these calculations is phenomenological; therefore, magnetic susceptibility corrections set an ultimate limit on accuracy of BS-QED predictions from first principles. They are only anticipated at the level of 10 ppt in the bound electron g-factor [29–31]

Nuclear Deformation corrects for assumptions about the shape of the nuclear potential. Some calculations will include the uncertainty of the nuclear shape into the nuclear size, but more recent investigations have elucidated the deformation effect to improve the overall theoretical uncertainty. In heavy nuclei, ND corrections occur as high as the ppm level although it is significantly smaller near closed nuclear shells contributing around 10 ppb at $Z = 82, N = 126$ [32].

The relative strength of each of these corrections is best demonstrated in figure 2.6 which shows that for low Z access to nuclear properties is limited by the precision of QED calculations, whereas in high Z sufficient precision of nuclear effects is an important factor in understanding QED in high fields.

2.2.1 Other quantities

Aside from the underlying nature of electrodynamics in high fields, the magnetic moment of the bound electron is fundamentally linked to other quantities of experimental interest, as can be understood from the description of the various interactions that affect its calculation. This shows the breadth of physical understanding that can be gained from bound electron magnetic moment measurements in a range of atomic systems. Figure 2.7 summarizes the range of atomic systems that are relevant for measurement of a particular

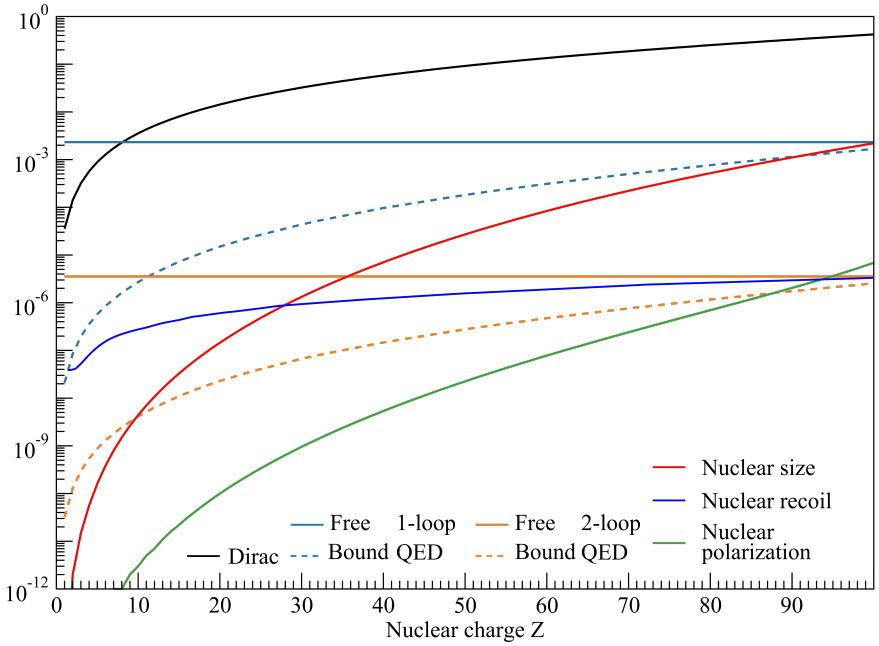

Figure 2.6: The individual effects of each correction to the 1s bound electron g-factor as a function of atomic charge Z. Lines represent overall trend not precise values. Figure modified from [34]

quantity or effect. For nuclear potential measurement or electron potential shielding effects, multi-electron systems and isotopic comparisons within a single nuclear charge are also of interest.

α The fine structure constant is intimately related to any interactions with the photon field, and scaling this interaction with Z means that the precision of the fine structure constant measurement is improved commensurately. However, the complete description of the theory of the nuclear interactions is required to improve the precision of α in high Z. Therefore measurements aiming to improve the precision of alpha via bound electron magnetic moments utilize medium Z systems. Measurements of optical transitions also benefit from enhancement in highly charged ions such as Pm^{14+} [35], or in low-lying nuclear transitions with exceptionally long lifetimes [36].

e_m As mentioned above, the bound electron g-factor calculation is sensitive to the electron mass at the same order as the nuclear recoil correction. The current limit on the precision of the electron mass comes from g-factor measurements in C^{5+} and O^{7+} [37]. Higher precision is sought in improved measurements in C^{5+}.

Nuclear Properties The sensitivity of the g-factor measurement to each of the nuclear corrections demonstrates its value as a probe of experimental determinations of those properties. Par-

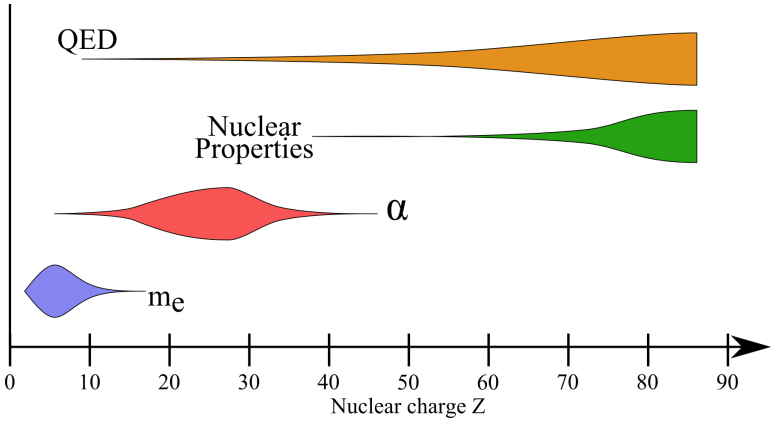

Figure 2.7: The sensitivity of bound electron g-factor measurements to various physical quantites or effects is dependent on the atomic system in which it is measured. The relative sensitivity is approximately indicated by the normalized width of labeled blobs as a function of the atomic charge of the measurement system for hydrogenlike ions.

ticularly in Hydrogenlike ions, the nuclear effects are not shielded by the inner electrons, making their determination from measurements more precise, or improving knowledge about electron shielding models. Additionally, in heavy HCIs with non-zero nuclear spin the electron magnetic moment is sensitive to the nuclear magnetic dipole moment at its current uncertainty [15].

2.2.2 High-order Zeeman Splitting

Experimental determination of the electron magnetic moment is done by measuring the strength of the interaction with an external magnetic field. The energy separation of two magnetic sub-states ΔE in the simple model of an electron magnetic dipole of constant strength and no higher multipole components is described in the anomalous Zeeman effect:

$$\Delta E(B) = \hbar\omega_L = g_j \mu_B B, \tag{2.10}$$

where ω_L the Larmor frequency. However, measurements of the Zeeman effect, particularly in high lying atomic shells, n, exhibit deviations from this linear splitting [38]. This effect has two physical causes: a component of the magnetic moment which is perpendicular to $\boldsymbol{j}$ (for $\boldsymbol{l} \neq 0$), and the diamagnetic effect on the electron orbit. Treatment of the shape of the magnetic moment at first order leads to the expected spin-orbit coupling, and an additional B^2 term in the interaction energy as an approximation at second order. The diamagnetic effect leads directly to a contraction of the semi-classical electron orbit with associated energy again proportional to B^2 [39]. These models are in good agreement with the quadratic nature of the measured effect and thus dubbed the *quadratic Zeeman*

Table 2.2: Some recent measurements of bound electron g-factors. Additional measurements listed in [22, 41] and references therein. Measurements of Ar and Ne were performed in precision penning traps, and Bi values were extracted from the lifetimes of the relevant hyperfine transition.

System	Measurement	Reference
$^{40}Ar^{13+}$	0.663 648 455 32(93)	[42]
$\Delta g(^{20}Ne^{9+} - ^{22}Ne^{9+})$	$13.475\ 24(53)_{stat}(99)_{sys}$ x 10^{-9}	[43]
$^{209}Bi^{82+}$	$1.729\ 4(3\ 5)_{stat}(1\ 9)_{sys}$	[13]
$^{209}Bi^{80+}$	$1.928(12)_{stat}(10)_{sys}$	

effect. In addition, transitions in high lying shells display significant broadening up to the point of an observed continuum before the ionization energy is reached. This may be interpreted as evidence of significant mixing of the magnetic sub-states at high n [40].

The modern QED treatment takes the magnetic sub-state, m_j, as an argument to the calculation of $g_j^{(i)}(m_j)$ at each order, i, and expands over the ratio of the magnetic energy to the electron rest energy as in equation 2.11. Thus precise measurement of the g-factors of electrons in multiple magnetic sub-states can improve models of the nature of the anomalous Zeeman effect.

$$\Delta E(B) = \sum_{i=1}^{\infty} g_j^{(i)}(m_j)\mu_B B\left(\frac{\mu_B B}{m_e c^2}\right)^i \tag{2.11}$$

2.2.3 Measurements of Bound State g-factors

Some of the existing measurement of bound electron g-factors have been mentioned already. Partial lists of existing measurements can be found in [22, 41] and the references therein. More recent measurements are listed in table 2.2. Here the measurements in Argon and Bismuth are highlighted as discussed below.

2.3 Laser-microwave Double Resonance Spectroscopy

Experimental measurement of the Zeeman separation energy is not directly observable as the transition has a natural lifetime of years or more. The effect of the stimulated transition can be effectively mapped onto another observable quantity. This is typically done in two ways. The first is by introduction of a non-linear magnetic field such that the magnetic sub-state can be determined from a small shift in the periodic ion motion. This was first demonstrated for the free electron [16], but can be extended to electrons bound to

spinless nuclei [44], and is known as the continuous Stern-Gerlach effect. The second is by generating a closed optical cycle between two energy levels of the bound electron, such that a spin transition moves the electron into a dark state and the monitored luminescence drops. This technique has achieved sub-Hz resolution in hyperfine splitting as well as microwave spectroscopy measurements and is referred to as the laser-microwave double-resonance (LMDR) technique [21, 30, 45]. However, it has yet to be successfully applied to microwave spectroscopy of Zeeman transitions in HCIs.

Laser-microwave double-resonance measurements rely on the availability of a laser-accessible transition within the atomic system that can be saturated. In HCIs the electron transition energies are shifted upward by the presence of the nuclear potential. The fine structure ΔE_{FS} and hyperfine structure splittings, ΔE_{HFS} depend on the nuclear charge as in equations 2.12 and 2.13 [22, 46]. This puts the fine structure separation in the near UV to near infrared range for nuclei from $Z = 10$ to $Z = 30$ depending on the particular transition [41]. Hyperfine transitions depend on the nuclear spin and are therefore are less predictable, but for hydrogenlike and lithium ions many transitions fall in this regime for Z from 60 to 100.

$$\Delta E_{FS} \propto \frac{Z^2}{r^2} : \langle r^2 \rangle \propto Z^{-2} \rightarrow \Delta E_{FS} \propto Z^4 \tag{2.12}$$

$$\Delta E_{HFS} \approx \frac{2(m_e c)^2}{3m_p}(2I+1)g_I \alpha^4 Z^3 \tag{2.13}$$

Here I is angular momentum of the nucleus and g_I its g-factor and m_p is the proton mass. Figure 2.8a shows the implementation of LMDR for measuring the Zeeman splitting in boronlike Argon and Figure 2.8b is the same in Bismuth. In either case the fluorescence of a saturated cycle transition is monitored while a microwave source is swept over the range of frequencies about the Zeeman separation energy. Successful stimulation of a spin flip of the bound electron is indicated by a drop in the fluorescence intensity as electrons are driven out of the closed cycle.

Fine and hyperfine transitions, while longer lived than principle atomic transitions, have a wide range of natural line widths. The chosen laser-accessible transition requires a sufficiently long lifetime for stimulation of the microwave transition, but not so broad as to make saturation unachievable. The Zeeman states are particularly long lived with lifetimes on the order of years or more with correspondingly narrow linewidths.

This method enables the measurement of the nuclear magnetic moment as the electron and nuclear angular momenta couple to produce the hyperfine spectrum, and the measured g_F of the Zeeman interaction is that of their combined momenta where $\boldsymbol{F} = \boldsymbol{I} + \boldsymbol{J}$. An

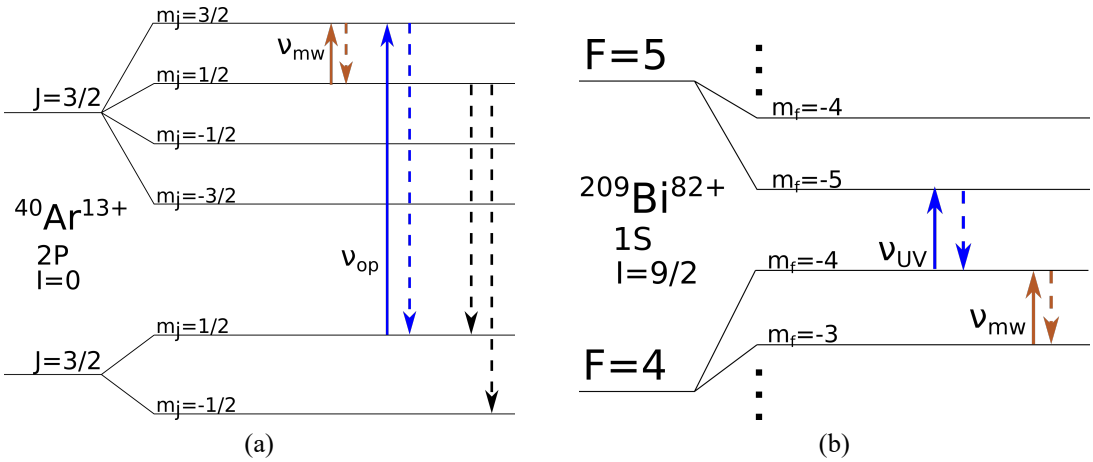

Figure 2.8: Application of the laser-microwave double-resonance technique to (a) boron-like Argon, where the Zeeman separated levels of the 2p fine structure are shown, and (b) hydrogenlike Bismuth, where the 1s hyperfine levels are shown with the nearest two Zeeman sub-states of each. The blue lines represent a saturated cycle. Introduction of microwave radiation at ν_{mw} stimulates a Zeeman transition. Black arrows indicate possible spontaneous decay paths.

explanation for decoupling the two terms through a measurement of Zeeman splitting in neighboring hyperfine states is provided in [17]. As the ions have one or few electrons, this provides an avenue for the first measurements of nuclear magnetic moments without significant diamagnetic shielding of the electron cloud.

$$g_F = g_j \frac{F(F+1)+J(J+1)-I(I+1)}{2F(F+1)} - \frac{m_e}{m_p} g_I \frac{F(F+1)+I(I+1)-J(J+1)}{2F(F+1)}. \quad (2.14)$$

Accounting for the available understanding laid out above. The ARTEMIS experiment aims at two initial candidates for the first application of LMDR spectroscopy of magnetic moments in HCIs: Ar^{13+} and Bi^{82+}

2.3.1 Ar^{13+} as a candidate

Ar^{13+} provides a reliable and well studied atomic system that can be produced directly inside the experiment due to a relatively low ionization potential 686.10 eV. The 2p fine structure transition is in the optical regime at 441.256 nm [47] with a lifetime of 9.573(6) ms [48]. The 2p doublet is also an attractive candidate for high-order Zeeman studies with reliable predictions on the sub-Hz scale. Figure 2.9 shows the calculated shifts to

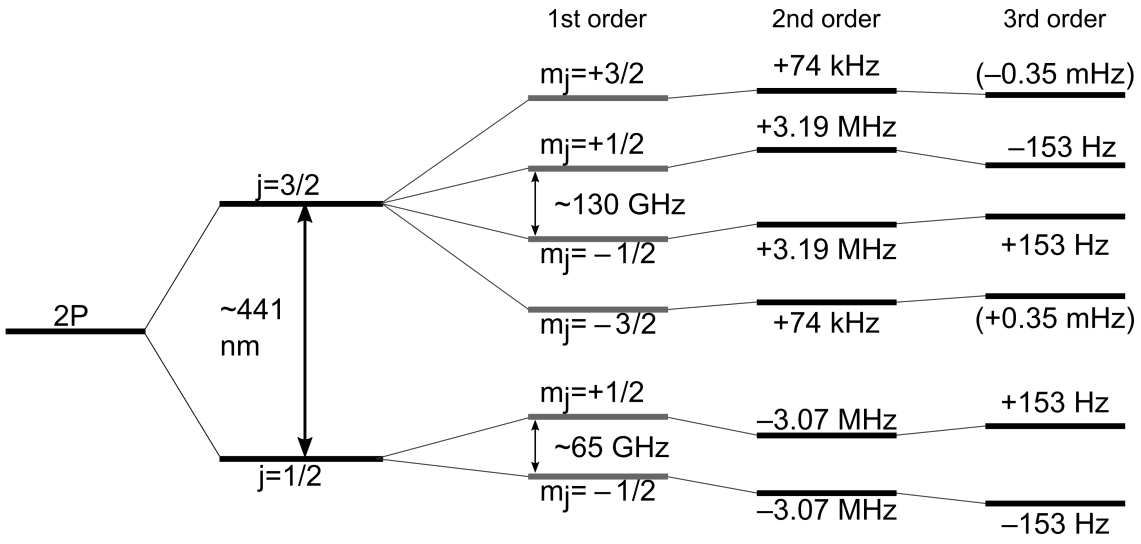

Figure 2.9: The Zeeman separation energies for the 2p fine structure of boronlike Argon are calculated to third order and represented here. Not to scale.

third order for a 7 T field. The microwave transitions are around 65 GHz and 130 GHz for the lower and upper fine structure states respectively at this field strength. Finally the theoretical predictions are precise already to the 100 ppb level for the ground state and 1 ppm for the upper fine structure level.

2.3.2 Bi^{82+} as a candidate

On the heavy HCI side, hydrogenlike Bismuth $Z = 83$ is an attractive candidate for LMDR spectroscopy. With nuclear spin $I = 9/2$, it has a hyperfine transition at 244 nm with a width of 2.5 kHz. This opens the possibility for resolved-sideband cooling of the trapped ions to below millikelvin temperatures [49]. Additionally the hyperfine transition in lithiumlike Bismuth is also laser accessible enabling the specific difference measurement as mentioned in section 2.2. The existing measurement of the g-factor of hydrogenlike bismuth is based on the lifetime of the hyperfine transition measured in an ion storage ring. It is therefore possible to improve the measurement by several orders of magnitude in a precision Penning trap. Such a measurement would be the first for heavy HCIs above $Z = 50$. The theoretical g-factors for hydrogen- and lithiumlike Bismuth are calculated in [15, 50].

$$\begin{aligned} g_j^{theo.}(\mathrm{Bi}^{82+}) &= 1.731\ 014(1) \\ g_j^{theo.}(\mathrm{Bi}^{80+}) &= 1.934\ 739\ 38 \end{aligned} \tag{2.15}$$

2.4 Ion Confinement in Penning Traps

Charged particle confinement allows prolonged experimental observation with minimal outside influence on the ionic system, thus charged particle traps are an ideal tool for precision fundamental physics studies [51]. Application of a strong, homogeneous external magnetic field to an ionic system for spectroscopy naturally yields radial confinement. Penning traps therefore lend themselves directly to studies of Zeeman splitting in HCIs. The Penning trap, so named after its inventor, Dutch physicist Frans Michel Penning, combines a static, uniform magnetic field and quadrupole electric potential well for full three-dimensional confinement. It was first demonstrated by Hans Dehmelt in 1968 [52], who shared the 1989 Nobel prize with Wolfgang Paul, inventor of the radio frequency quadrupole trap named after him [53], for 'their development of the ion trap technique' [54].

2.4.1 Design Considerations of Penning Traps

A charged particle in a Penning trap is confined in the radial plane by the static magnetic field which induces cyclotron motion of the charge with frequency:

$$\omega_c = \frac{qB}{m}. \tag{2.16}$$

An electrostatic field, Φ is introduced to confine the particles axially. In the ideal particle trap, the potential of this field is harmonic along the magnetic field axis such that the motion of the trapped particles is that of a simple harmonic oscillator. By Earnshaw's theorem the field must be repulsive in at least one dimension. Practically, this field configuration is created as a quadrupolar field which is radially repulsive and attractive axially:

$$\begin{aligned} \Phi(\boldsymbol{r}) &= \frac{V_0}{4d^2}(2z^2 - \rho^2) \\ d^2 &= \frac{1}{4}(2z_0^2 + \rho_0^2) \end{aligned} \tag{2.17}$$

Here cylindrical symmetry is manifest with the radial dimension ρ, and axial dimension z being the direction of the uniform magnetic field. The coefficients are chosen so that the potential is asymptotic to $z = \rho$. V_0 is the potential applied to the center trapping electrode, traditionally called the *ring*, relative to the *endcaps*, and d is the characteristic trap dimension in terms of the electrode dimensions as shown in figure 2.10. Such a field geometry is most easily realizable with hyperbolic electrodes. However, this geometry of the trapping electrodes significantly limits access to the interior trap volume. This is

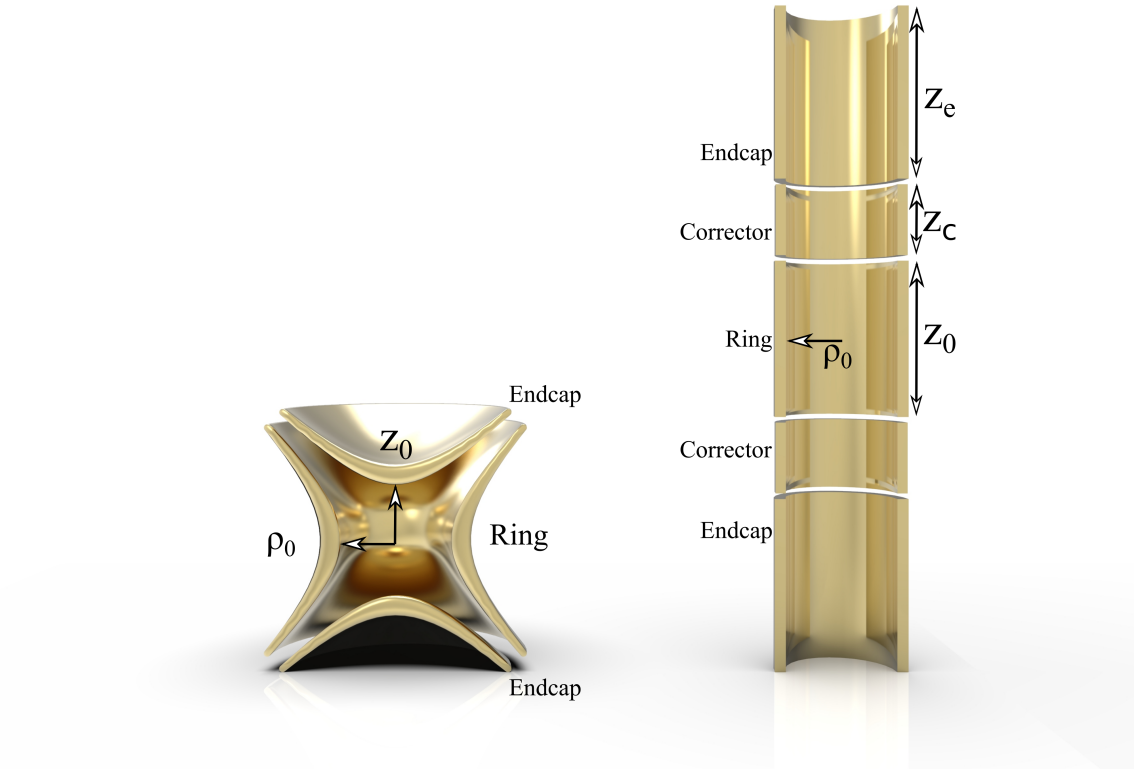

Figure 2.10: A hyperbolic Penning trap design is compared to an open cylindrical design. The electrodes are labeled according to their function, and the dimensions of the electrodes are labeled.

referred to as a closed trap design. Opening access to the trap interior requires compensation of the altered field geometry to restore harmonicity. This can be done by a particular choice of the electrode dimensions, which is referred to as mechanical compensation, or by the introduction of additional compensator electrodes to shape the field at the trap center, called electrical compensation. Figure 2.10 shows a comparison of a closed hyperbolic and an open cylindrical Penning trap design [41, 49].

For a discussion of the measure of a traps harmonicity, it is useful to write the electric potential as an expansion over the set of Legendre polynomials P_i:

$$\Phi(\boldsymbol{r}) = \frac{V_0}{2} \sum_{i=1}^{\infty} C_{2i} \left(\frac{r}{d}\right)^{2i} P_{2i}\left(\frac{z}{r}\right). \tag{2.18}$$

In this form the trap is exactly harmonic when all higher components of the field are zero ($C_{>2} = 0$). Cylindrical Penning traps usually have $C_2 \approx 0.5$. Most Penning traps have dimensions on the order of centimeters, and charged particle orbits of micrometers.

Therefore r/d is small and C_6 is highly suppressed relative to C_4, leaving it as the dominant electric field imperfection. Electrical compensation allows the values to be tuned by the choice of potentials. Equations 2.19 show the relationship between the coefficients of the potential expansion and the applied potentials to the ring and compensator electrodes, V_0 and V_c respectively, for the first two terms. [55]

$$\begin{aligned} C_2 &= C_2^{(0)} + C_2^{(1)} \frac{V_c}{V_0} \\ C_4 &= C_4^{(0)} + C_4^{(1)} \frac{V_c}{V_0} \end{aligned} \tag{2.19}$$

The coefficients C_i^j come directly from the electrode geometry. Thus a choice of U_c/U_0 can set C_4 to 0. Moreover, particular design of the compensator electrode geometry allows simultaneous tuning-out of C_4 and C_6. Finally, the geometry of the ring can be set such that $C_2^{(1)} = 0$. This prevents the ion motion from being dependent on the trapping potential, which is called an *orthogonalized* trap. As a last note, the length of the endcap electrodes must also be sufficiently long to limit imperfections at the trap center. This is usually at least $z_e > 3\rho_0$, but should be even higher for precision traps [55].

2.4.2 Ion motion in a Penning Trap

Directly from the fields and the Lorentz force law one can write the equations of motion for a charged particle in a Penning trap in Cartesian coordinates:

$$\begin{pmatrix} \ddot{x} \\ \ddot{y} \\ \ddot{z} \end{pmatrix} = \omega_c \begin{pmatrix} \dot{y} \\ -\dot{x} \\ 0 \end{pmatrix} + \omega_z^2 \begin{pmatrix} x/2 \\ y/2 \\ -z \end{pmatrix} \tag{2.20}$$
$$\omega_z^2 = \frac{qC_2V_0}{md^2}.$$

The axial harmonic motion is evident as expected with frequency ω_z, and the radial motion includes the velocity-dependent cyclotron orbit as well as the radially repulsive electrostatic field. The interaction of the two components of the radial motion can best be understood by looking at the radial trajectory [56].

$$\rho^2(t) = \rho_+^2 + \rho_-^2 + 2\rho_+\rho_- cos((\omega_+ - \omega_-)t) \tag{2.21}$$

Here the relative phases are ignored, $\rho_\pm$ are the constants of integration which depend on the initial condition, and $\omega_\pm$ are the roots of the characteristic equation. This shows both that the radial motion consists of two independent oscillations and that it is bounded

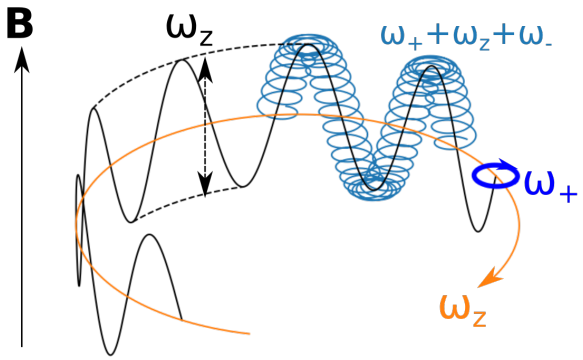

Figure 2.11: The three combined eigenmotions of an ion in a Penning trap are shown for typical operating conditions in light blue. Orange shows the magnetron motion alone, black the axial and magnetron combined and dark blue the reduced cyclotron motion centered on the magnetron orbit.

by $\rho_+ + \rho_-$ and $\rho_+ - \rho_-$. All together the charged particle performs three independent motions simultaneously, often simply denoted by their frequencies: reduced cyclotron motion, ω_+, axial motion, ω_z, and magnetron motion, ω_-. The frequencies are related by:

$$\omega_\pm = \frac{1}{2}\omega_c \pm \sqrt{\omega_c^2 - 2\omega_z^2} \tag{2.22}$$

Outside of extreme trapping potentials the three frequencies of motion follow a hierarchy $\omega_c > \omega_+ \gg \omega_z \gg \omega_-$. The complete motion of all three modes simultaneously is broken down in figure 2.11.

As these modes are independent (or only weakly coupled) each can have an independent energy and they can be individually manipulated by modulation of the confining field at the corresponding frequency. In this way it is easier to consider the quantum picture of the motion of the ion. Each motional mode behaves as a quantum oscillator with an energy difference of $\hbar\omega_i$ between states. Each reduced cyclotron level splits into many axial energy levels which in turn split into many magnetron energy levels. This effectively continues until the escape energy. However, in practice the quantum levels are only directly observable for ultracold stored particles. Figure 2.12 is a representation of this quantum picture of Penning trap motion near the ground state of the trapping potential. In most particle traps the ions are still at temperatures of a few Kelvin, and therefore have quantum numbers in the thousands to millions range. The quantum picture is still useful to explain the effects of sideband coupling the motional modes which can move ions up or down along the ladder of energy states of two motional modes. This is done by modulation of the trapping potential at the sum or difference frequency (i.e. $\omega_i \pm \omega_j$).

Imperfections of the confining fields or the presence of multiple particles can shift the

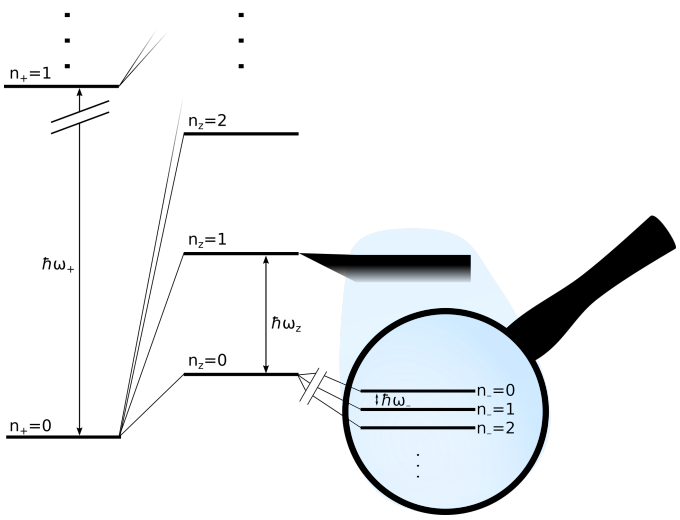

Figure 2.12: The notion of the motion in a Penning trap as a collection of quantum harmonic oscillators is depicted. Each eigenmode has a corresponding energy which is quantized with separation $\hbar\omega_i$ The reduced cyclotron levels split into axial levels which split into magnetron levels. The magnetron spectrum is inverted because the potential is repulsive.

individual eigenfrequencies, but their mutual relationship is more robust against imperfections. This is the Gabrielse invariance theorem [57]:

$$\omega_c^2 = \omega_+^2 + \omega_z^2 + \omega_-^2 \tag{2.23}$$

2.4.3 Temperature of Trapped Ions

Frequently throughout this work the temperature of an ion bunch will be referenced. Although the notion of temperature is generally well understood, within the context of a sparse ion cloud or especially an individual ion it is less clear. A trapped ion cloud can interact with its environment by coupling of the motional modes to, for example, charges in the conducting electrodes of the trap. Outside of thermal equilibrium the ions' temperature is merely hotter or colder as defining the mechanism of heat transfer defies the typical notions. At thermal equilibrium however, it is precisely defined. In this context the word ensemble is used to describe an ion bunch that fills the allowable phase space with probabilities proportional to their temperature. Therefore each mode of the ion's motion can have a different temperature and thermalization occurs proportionally to the strength of the interactions of multiple modes or to the environment (see sections 2.4.5 and 2.5).

2.4.4 Frequency shifts

Although the electrical compensation allows tuning-out of the non-harmonic components of the electric potential, this cannot necessarily be achieved at the desired level of precision. In addition, the magnetic field can similarly be considered in a multipole expansion. Although the real magnetic field is of course a dipole or higher in shape, at the scale of the trapped particles it can be considered a uniform field with dipole perturbation, B_2, at first order. The frequency shifts caused by $C_4 \neq 0$ and $B_2 \neq 0$ are dependent on the energy of the corresponding mode of motion as in equations 2.24.

$$\begin{pmatrix} \Delta\omega_+/\omega_+ \\ \Delta\omega_z/\omega_z \\ \Delta\omega_-/\omega_- \\ \Delta\omega_L/\omega_L \end{pmatrix} = (M_E + M_B) \begin{pmatrix} E_+ \\ E_z \\ E_- \end{pmatrix}$$
$$M_E = \frac{6C_4}{qC_2V_0} \begin{pmatrix} \eta^4/4 & -\eta^2/2 & -\eta^2 \\ -\eta^2/2 & 1/4 & 1 \\ -\eta^2 & 1 & 1 \\ 0 & 0 & 0 \end{pmatrix}, \tag{2.24}$$
$$M_B = \frac{B_2}{2B_0 m\omega_+\omega_-} \begin{pmatrix} -\eta^2 & 1 & 2 \\ 1 & 0 & -1 \\ 2 & -1 & -2 \\ -\eta^2 & 1 & 2 \end{pmatrix}$$

where $\eta = \omega_z/\omega_+ \ll 1$. Notably at higher energies of the axial motion, the dominant shift actually comes from the dodecapole term [58].

Aside from spatial distortions, temporal fluctuations of the confining fields must also be controlled to prevent the corresponding temporal drift of the measured frequencies. This is especially critical for the magnetic field where the temporal fluctuations can limit the precision of the magnetic moment measurement over the long time for sweeping the microwave frequency.

If the electric and magnetic fields experience a mutual tilt, θ, such that the axes of radially symmetry of each field are not parallel, the frequencies are shifted by:

$$\begin{aligned} \omega'_\pm &\approx \omega_\pm \frac{\omega_-}{2} sin^2\theta \\ \omega'_z &\approx \omega_z \left(1 - \frac{1}{4} sin^2\theta\right) \end{aligned} \tag{2.25}$$

2.4.5 Multiple particles in Penning traps

The presence of multiple particles in a region of space is often referred to as space charge. Space charge in a Penning trap modifies the spatial distribution of the trapping potential. The center of charge of all trapped particles, the point where the first moment of charge is zero, follows the same equations of motion as for a single particle because all interactions between particles are mutual, and the charge to mass ratio of the collection is the same as for an individual ion. In this context it is useful to consider a cloud of confined ions with charge state q and mass m as a non-neutral plasma. Ions within the plasma oscillate relative to the bulk motion of the plasma center at the plasma frequency:

$$\omega_p^2 = \frac{q^2 n}{\epsilon_0 m} \tag{2.26}$$

where ϵ_0 is the permittivity of free space and n is the ion density. The modified potential shifts the eigenfrequencies to:

$$\begin{aligned} \omega_z' &= \omega_z \sqrt{1 - \frac{\omega_p^2}{3\omega_z^2}} \\ \omega_\pm' &= \frac{\omega_c}{2}\left(1 \pm \sqrt{1 - \frac{2\omega_z^2}{\omega_c^2}(1 + \frac{2\omega_p^2}{3\omega_z^2})}\right). \end{aligned} \tag{2.27}$$

Above the so-called Brillouin limit of the ion density, n_{max}, the electric repulsion exceeds the magnetic confinement radially and no additional charges can be confined. This is typically billions of charges per cubic centimeter [59]:

$$n_{max} = \frac{\epsilon_0 B_0^2}{2m}. \tag{2.28}$$

One can consider the motions of the individual ions as the motions of the center of charge broadened by the plasma mode such that the axial mode has a population distribution according to equation 2.29. While it has no effect on the measurement of ω_z directly, it is a source of broadening in the emission spectrum of spectroscopic investigations of the ions with axial aligned lasers [60].

$$\frac{\delta\omega_z}{\omega_z} = 1 - \sqrt{1 - \frac{\omega_p^2}{3\omega_z^2}} \tag{2.29}$$

The density of the ion plasma also determines the correlation of the motion of the individual charges. This is typically characterized by the plasma parameter, Γ. In a gas like state $\Gamma \ll 1$ there is very little exchange of energy between the ions or their individual

motional modes. This in an important consideration when cooling a single mode in a state with low correlation as the thermalization time of an individual mode to its environment can be much less than between two modes. Ions in ARTEMIS have been successfully cooled to a liquid-like state $1 < \Gamma < 10$ [61] and cooling to crystal-like states is routinely achieved in systems with fewer ions [62, 63].

These effects and their implications are considered in the implementation of ARTEMIS and the beamline presented in chapters 3 and 4. For a complete discussion of the systematic shifts of particle frequencies in Penning traps see [41] and for further systematic study of their effects in ARTEMIS [64–67].

2.4.6 Pressure as a Limit on Ion Lifetime

A trapped ion bunch can be considered a stable system as long as care is taken to avoid exciting motional resonances of the ion or plasma. In such a case the dominant mechanism of particle loss is due to charge exchange interactions with the residual background gas atoms. Müller and Salzborn compiled the measured charge exchange cross sections for a range of atomic systems, background gases and interaction energies. They then fit an empirical formula to the data [68, 69]:

$$\begin{aligned}\sigma =& 1.43\text{x}10^{-12}\, q^{1.17} I^{-2.76} \\ &+ 1.08\text{x}10^{-12}\, q^{0.71} I^{-2.80} \\ &+ 5.50\text{x}10^{-14}\, q^{2.10} I^{-2.89} \\ &+ 3.57\text{x}10^{-16}\, q^{4.20} I^{-3.03}\end{aligned} \tag{2.30}$$

Here σ is the charge exchange cross section in cm^2, q is the integer charge state of the ion, and I is the ionization energy of the background gas in eV. Each term accounts for interactions exchanging one more electron than the last beginning with single charge exchange. The cross section scales somewhat more than linearly with the ion charge state. The collected data covers a range of interaction energies between keV to MeV, and little data is currently available in the eV range; therefore the cross sections estimated this way for measurements in particle traps may be overestimates due to the extremely low interaction energy. The single charge exchange cross section between Ar^{13+} and both helium and molecular hydrogen were measured in [70] at 198 eV/q. The measured value is about a factor of 2 less than as calculated by 2.30. The total charge exchange cross section between N^{4+}, which will be referenced in chapter 5, and atomic hydrogen was measured for a range of energies in [71]. For the lowest available energy (525 keV), the Müller-

Salzborn fit overestimates the cross section by a factor of 7. The Figure 2.13a shows the total cross section for charge exchange of up to four charges for a range of ion charge states and background gases.

Figure 2.13b shows the expected lifetime of some ion species as a function of the pressure of molecular hydrogen gas, which is the usually dominant residual gas at cryogenic temperatures. From this it can be observed that HCI storage for the highest charge states of only a few hours requires excellent vacuum pressure below 10^{-15} mbar. Creating such conditions usually requires hermetically sealed containers at cryogenic temperatures which in turn poses a challenge for ion injection (see section 4.1).

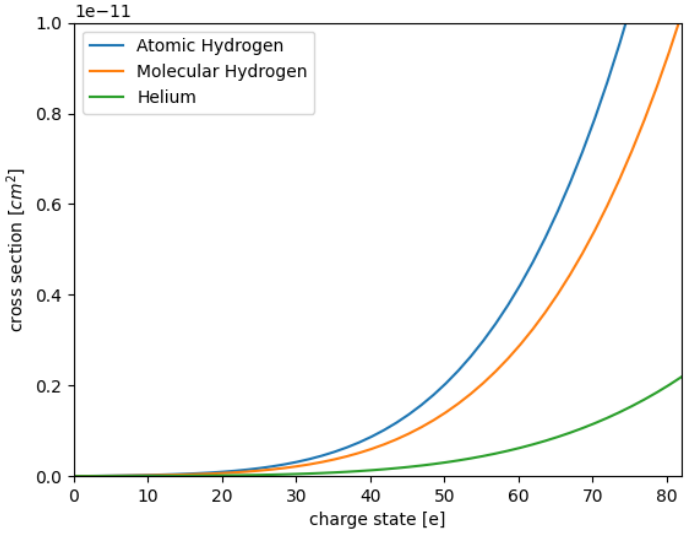

(a)

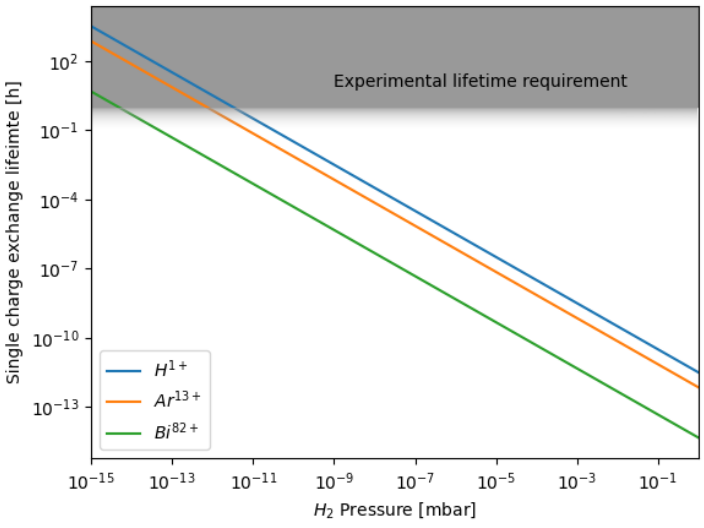

(b)

Figure 2.13: (a) The single-charge exchange cross sections for a range of charges in various background gases. (b) The expected lifetime of an ion cloud decaying due to charge exchange with a background gas of molecular hydrogen at 4 K. The shaded region shows the approximate required lifetimes for the g-factor measurements in ARTEMIS, usually more than a few minutes to a few hours depending on the cooling condition of the trapped ions and the complexity of the experiment.

2.5 Particle Detection and Cooling

From the method of image charges [72], it can be shown that a charged particle moving in the vicinity of a conductor at constant potential causes a current

$$I = q\nabla\Xi(\boldsymbol{r}) \cdot \frac{d\boldsymbol{r}}{dt} \tag{2.31}$$

where $\Xi \in [0, 1]$ is the unitless *geometry factor* of the electrode. It describes the fraction of a nearby charge which is induced in the conductor at each point in space. This can be extended directly to the center-of-charge motion of multiple charges. For ions in Penning traps, this is generally in the range of fA to pA depending on the conditions of the ion ensemble and the trap.

An ion ensemble in a cryogenic environment with effective suppression of electronic interference is well isolated and acts as an undamped oscillator [73, 74]. Detection of the ion motion can be considered as measurement of the energy dissipated by a damped oscillator coupled to the ion oscillations. The model of the detection circuit is that of a tuned, resonant tank circuit followed by amplification within the cryogenic environment to ensure a sufficient signal-to-noise ratio in the subsequent room temperature detection electronics. This detector scheme is depicted in figure 2.14.

On resonance the impedance of the resonator is maximized and the induced current is dissipated by the effective parallel resistance, $R_p = \omega_0 L Q$, where ω_0 is the resonance frequency, and Q is the resonators quality factor, defined as the ratio of the stored energy

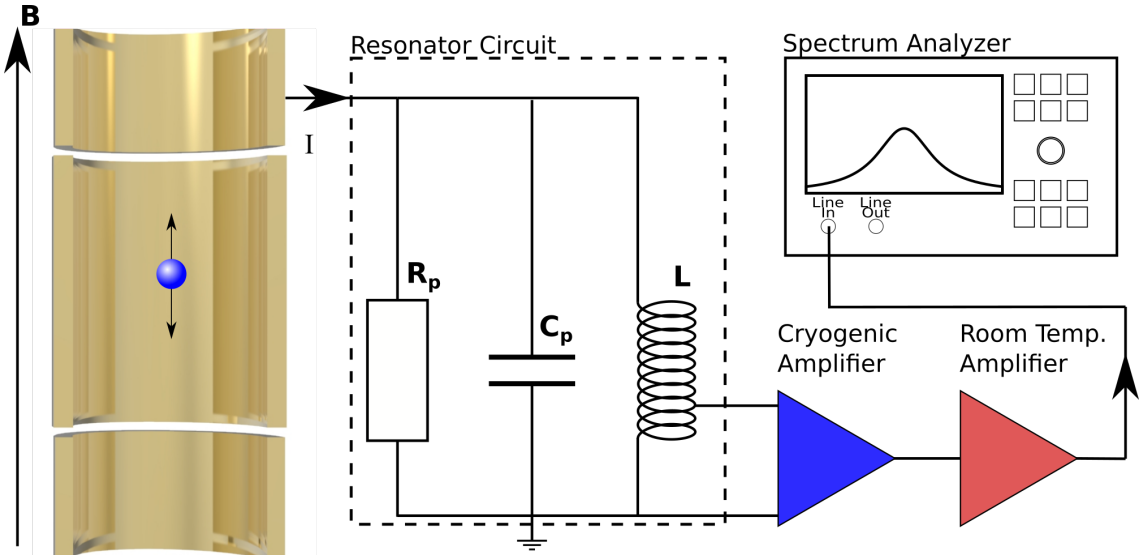

Figure 2.14: Schematic of the non-destructive particle detection circuit for axial motion in a cylindrical Penning trap.

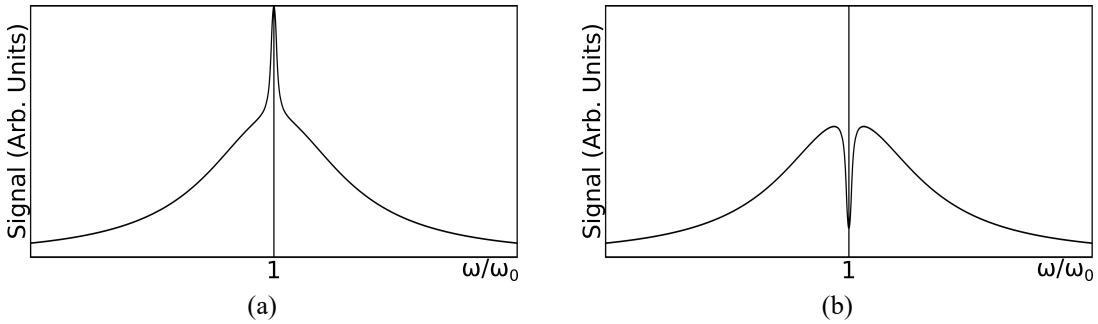

Figure 2.15: The frequency response of the detector system to an ion cloud appears (a) as an ion peak superimposed on the resonator spectrum for hot ions or (b) as a dip to the baseline for cold ions.

in the resonator to the energy loss per cycle. This causes a voltage difference across the resonator which is then amplified and detected, usually in a frequency spectrum as the signal is periodic.

For an ion bunch that is hotter than the detection circuit, the energy dissipation results in a peak superimposed on the resonator spectrum as shown in figure 2.15a. Although in some conditions the frequency of the ions can be as broad or even broader than the resonator (see 2.4.4). Because energy is dissipated, this process inherently cools the ions. As they approach thermal equilibrium, the peak is replaced by a dip to the baseline of the frequency distribution. Physically this corresponds to the ions acting as a high quality short-circuit of the thermal energy in the resonator at the frequency of their motion. The resulting spectrum appears in Figure 2.15b.

As described in section 2.4, the frequency of the axial motion is dependent on the applied potential to the trap electrodes. If the trap is orthogonalized, this allows a spectrum of multiple charge states or ion masses to be measured simultaneously by sweeping the applied potential over a range of values for a particular resonance frequency. As the frequency of motion of each trapped species approaches that of the resonator, the dip or peak will appear over the resonator peak. Integrating the signal over a window about the center of the resonator peak at each voltage produces a data set of ion signals picked up by the resonator for each step of the trap potential. This procedure is depicted graphically in figure 2.16 and the resulting spectra are referred to as charge to mass spectra (q/m spectra). These spectra are the most common method for determining the conditions of ions trapped inside ARTEMIS. The expected trap potential for a specific ion to be on resonance with the detection systems can be predicted by equation 2.20, with small corrections as described in 2.4.4. Ions with similar charge to mass ratios can be identified by considering chains of charge states of the same mass. The individual charge states can even be identified for

larger shifts as the spacing is quadratic.

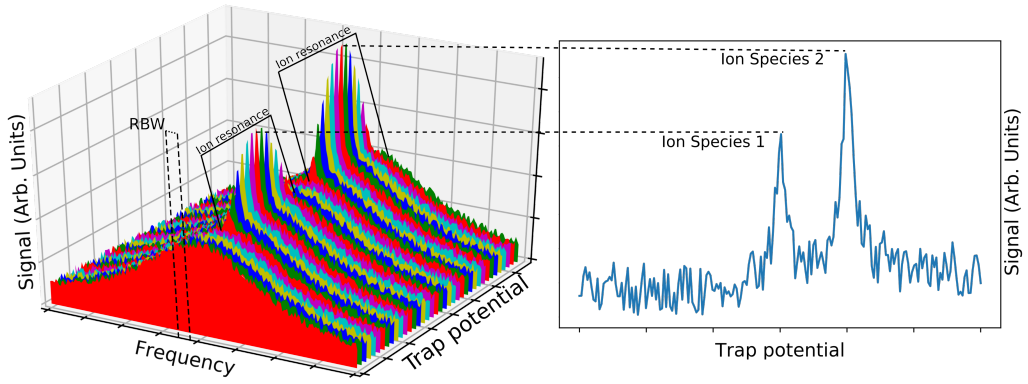

Figure 2.16: Graphical depiction of the method for measuring charge to mass spectra. As the trapping potential is swept, ions with different ratios of charge to mass will come into resonance with the detection circuit. Integration over the resolution band width (RBW) produces a spectrum of charge-to-mass states present in the trap.

2.6 Cryogenic Environments

Within an ultra high vacuum system, the density of residual gas atoms is so low that they interact many times with the chamber walls between mutual interactions. This is the free molecular flow regime. Further reduction of the gas density is generally limited by slow leaks (usually less than 10^{-11} mbar $\cdot$ m/s) as well as permeation, diffusion and desorption of molecules from the interior surfaces [75]. Leak rates and permeation are dependent on the pressure differential whereas diffusion and desorption can be limited by ultracold surfaces. Therefore the best vacuum conditions are created by hermetically sealed cryogenic environments that are themselves vacuum insulated.

2.6.1 Cryopumping

In cryogenic environments the residual gas atoms will condense onto the cold surfaces leading to a further reduction in the density of the gas phase. Figure 2.17 shows the theoretical equilibrium pressure of the gas phase for various gases as a function of temperature. A majority of the components of air sufficiently freeze out in the few Kelvin range leaving only Helium and Hydrogen. The condensation is further aided by the extremely low densities, which cause only a slow buildup of gas atoms on the cryogenic surfaces. This allows capture of gas on the surface by adsorption rather than condensation alone. Physically this means that interactions with the cold surface remove sufficient energy from the atoms that

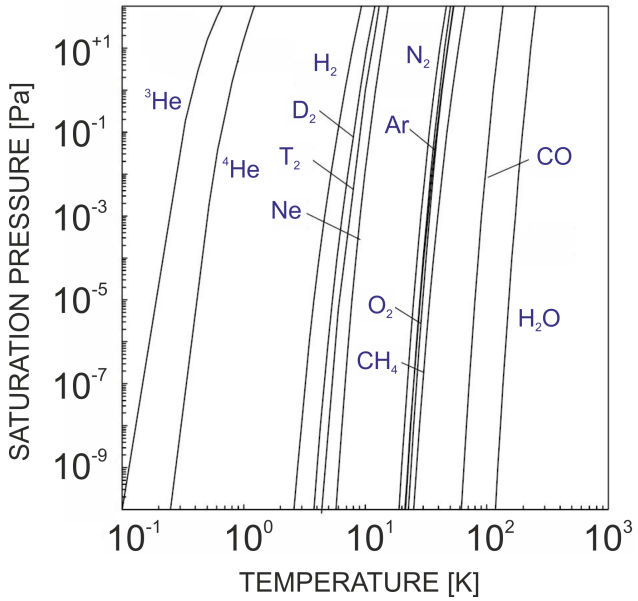

Figure 2.17: The vapor pressure at saturation of several gases is given as a function of temperature. Figure from [41].

they stick to the cryogenic surfaces by intermolecular forces, and pressures far below the saturation pressure can be reached. This effect is often referred to as *cryosorption* [76]. The pressure rises again slowly as layers of atoms accumulate on the cold surfaces which reduces the probability of adsorption. The time until monolayer saturation depends on the rate of molecular flux into the cryogenic region. This is a critical consideration at the interface between cryogenic and room temperature vacuum regions, where molecular flux is on the order of 10^9 molecules per square centimeter-second or more, leading to monolayer saturation times of only a few weeks or less [77]. Therefore it is often necessary to seal off the cryogenic region from the room temperature regions despite an otherwise strong cryopumping effect, either completely or when necessary by a small aperture or preferably a movable cryogenic valve. Sufficient reduction of the molecular flux enables effectively unlimited lifetime of the sub-saturated condition.

2.6.2 Heat Loads

Maintaining the temperatures of the cryogenic environment requires careful consideration of the maximum thermal power of the cryogenic pump. These are usually limited to less than 2 Watts at 4 K for compact cold heads such as the one at ARTEMIS. Heat transfer by convection is negligible for most systems which are vacuum insulated. Conduction can be limited by reducing the cross sectional areas of supporting components and increasing the distance between cold and warm regions of the apparatus as well as proper choice of

materials. The most challenging source of heat tends to be radiation. The radiative heat transfer rate between two surfaces is

$$\dot{q} = \sigma(T_1^4 - T_2^4)\left(\frac{1-\epsilon_1}{\epsilon_1 A_1} + \frac{1}{A_1 F_{12}} + \frac{1-\epsilon_2}{\epsilon_2 A_2}\right), \tag{2.32}$$

where σ is the Stefan-Boltzmann constant, T_i is the temperature of surface i, ϵ_i is its emissivity, and A_i its area. Finally F_{ij} is the *view factor* from surface i onto j. This is the fraction of radiated energy leaving surface i that impinges on surface j and is a property of the geometry.

The most notable part of this relationship is that the heat flux depends on the difference of the fourth power of temperature. For a sense of scale, the introduction of an intermediate surface which is actively cooled to 40 K between a 4 K region and room temperature, reduces the thermal load by a factor of more than 3000. Moreover, active cooling at 40 K can handle much higher heat loads, usually tens of Watts. This technique is essentially the *de facto* method for radiation shielding of cryogenic systems and commercial cryopumps usually include two temperature stages integrated into a single device.

This same trick can be applied to passively cooled surfaces as well. For a single passively cooled surface between the hot and cold ones the heat load is reduced by half as it reaches equilibrium at the average temperature of the two outer ones. For n layers this scales with $(n+1)^{-1}$. Such a method of radiation shielding is usually accomplished by multi-layer insulation (MLI) which is 10 to 20 layers of low emissivity material alternating with low thermal conductivity layers. Ensuring that the layers do not touch can reduce radiative heat loads to the 4 K surface to less than $100 mK/m^2$ [78].

2.6.3 Material Properties

Most thermal properties of materials are temperature dependent. Generally a good thermal conductor should be used on all cryogenic surfaces and poor ones for the surrounding supporting material. Care should be paid to ensure that thermal contraction doesn't isolate parts which are in good thermal contact at room temperature as this would disrupt the flow of heat to heat sinks.

Stainless steel or Polyether ether keytone plastic (PEEK) are good thermal insulators for use in vacuum environments. Copper, especially Oxygen-free High Conductivity (OFHC), is an excellent material for both thermal conduction of cryogenic components as well as electrical conduction for grounding electronics in the cold region. Brass or aluminum contract more than copper or stainless steel and can be used to ensure connections of components are maintained as they cool. Teflon is often used for insulation of AC sig-

Table 2.3: The thermal conductivity, k, and relative contraction , δL, and resistivity ρ for some materials used in cryogenic environments [79–86].

Material	$k(4K)$ $[\frac{W}{m \cdot K}]$	δL	$\rho(300K)$ $[\Omega \cdot cm]$
304 Stainless steel	0.2724	296	$7.2\text{x}10^{-5}$
OFHC copper	> 300	326	$1.72\text{x}10^{-6}$
6061 Aluminum	5.347	415	$2.65\text{x}10^{-6}$
Brass	1.974	384	$6\text{x}10^{-6}$
PEEK	$1.08\text{x}10^{-2}$	$1.3\text{x}10^{3}$	$16\text{x}10^{15}$
Macor	< 0.1	$100 - 200$	10^{17}
Sapphire	10^2	79	10^{16}
Teflon	0.04599	2127	$10^{25} - 10^{27}$
Constantan	0.878	$2.1\text{x}10^{2}$	$4.90\text{x}10^{-5}$
NbTi	0.176	> 188	$1.4\text{x}10^{-5}$

nal wires for its low dielectric loss and outgassing in vacuum. The wire core is often made of low conductivity constantan although a range of materials with different thermal and electrical conductivities are possible. Macor or sapphire combine good electrical isolation with good thermal conduction.

Table 2.3 list the thermal conductivity, k, thermal contraction δL, and electrical conductivity of these materials. Thermal contraction is reported in the form of equation 2.33, where L_T is the length of material at temperature T. The electrical conductivity at cryogenic temperatures is usually reported as the residual resistivity ratio (RRR), the ratio of the resistance at room temperature to the projected resistance at absolute zero. The RRR depends on the density of impurities and grain boundaries as well as the magnetoresistance induced by external magnetic fields, therefore the values in 2.3 are given at room temperature as a reference. Commercially available wires intended for cryogenic application are marketed by their RRR value. Thermal conductivity is also influenced by the RRR so values are approximate or ranges.

$$\delta L \equiv 10^5 \frac{L_{293} - L_4}{L_{293}} \tag{2.33}$$

2.6.4 Superconductors

Another major benefit of the cryogenic temperatures used in these experiments is that it allows detection circuitry to be superconductive. The presence of the magnetic field limits detection to type-II superconductors in the Schubnikov phase, where quanta of magnetic flux penetrate the superconductor material. Figure 2.18 shows a slice of the phase diagram

for superconducting materials at low currents. The most common material for detection circuits is Niobium-titanium in some form although Niobium-tin is used instead with high magnetic fields.

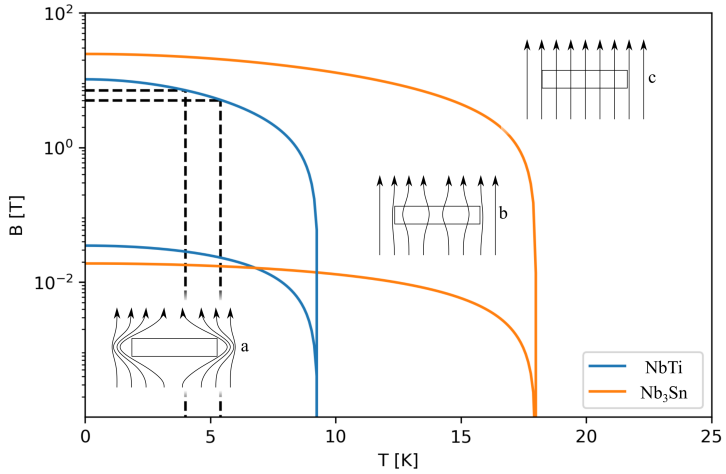

Figure 2.18: Phase diagrams of NbTi and Nb_3Sn. Phase transitions are indicated by solid lines and the inset graphics depict the extent of exclusion of the magnetic field lines by a superconductor in each phase: a, the Meisner phase, b the Schubnikov phase, and c the normal conducting phase. The values applicable to ARTEMIS's resonators made from NbTi are within the dotted lines.

2.7 Electrostatic Ion Optics and Injection into Penning Traps

At low energies ion bunches can be directed and decelerated using purely electrostatic components. The theory of ion optics was developed in [87, 88] and a matrix method based on the position and angle of electrostatic lenses was introduced in [89]. A full description of the matrix methods for the 6 dimensional model of an ion beam can be found in [90, 91]

The notion of ion optics is best understood in terms of an ion's deviation from a reference trajectory at a particular energy as depicted in figure 2.19, where its state can be defined by 6 parameters at each position, s, along the reference:

$$\boldsymbol{x}(s) = \begin{pmatrix} x \\ x' \\ y \\ y' \\ \delta s \\ \delta E \end{pmatrix} = \begin{pmatrix} Displacement\ along\ x \\ Angular\ deviation\ to\ x \\ Displacement\ along\ y \\ Angular\ deviation\ to\ y \\ Deviation\ along\ s \\ Relativeenergy\ difference \end{pmatrix} \tag{2.34}$$

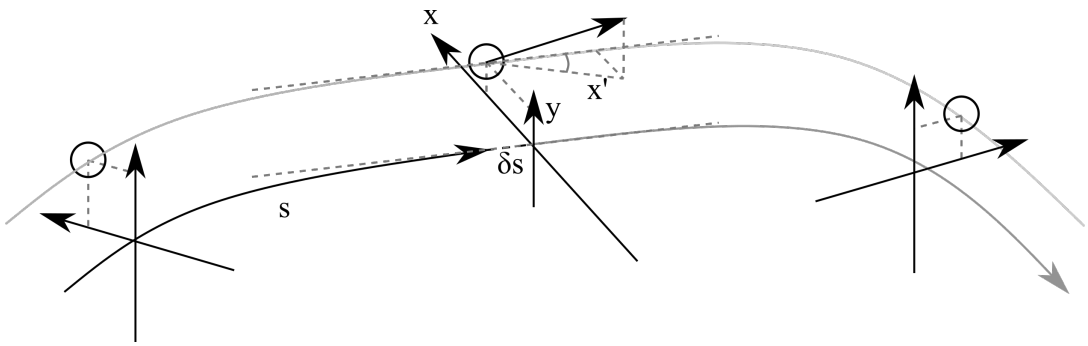

Figure 2.19: The position of an ion (black circle) at three positions along a trajectory (gray line). The ion kinematics are completely defined by comparison with a reference trajectory, $\boldsymbol{s}$, used in ion optics. Terms are defined in equation 2.34. Dotted lines depict tangential or orthogonal components of the trajectory or ion velocity vector.

The effect of a discrete electrostatic component can then be determined as a 6-dimensional square matrix, R(s), such that $x_j(s) = R_{ij}(s)x^i(0)$. This discretized treatment requires that there exists a well defined region before and after the element where the ions drift freely at the reference energy. The effects of multiple elements can then be described by the combination of matrix elements. Matrix descriptions have been determined for some common electrostatic elements such as lenses, multipoles, and benders, in terms of their geometry . Using rotational or planar symmetric components can help to reduce the coupling between horizontal and vertical motions, and beam tracking simulations can be used to minimize the dispersive elements $R_{i5} \forall i \in \{0, 1, 2, 3\}$ such that ions with different energies follow similar trajectories. This reduces many electrostatic matrices to the form

$$R_{ij} = \begin{pmatrix} R_{00} & R_{01} & 0 & 0 & 0 & 0 \\ R_{10} & R_{11} & 0 & 0 & 0 & 0 \\ 0 & 0 & R_{22} & R_{23} & 0 & 0 \\ 0 & 0 & R_{32} & R_{33} & 0 & 0 \\ R_{40} & R_{41} & R_{42} & R_{43} & R_{44} & R_{45} \\ 0 & 0 & 0 & 0 & 0 & 1 \end{pmatrix} \tag{2.35}$$

$$R_{hor} = \begin{pmatrix} R_{00} & R_{01} \\ R_{10} & R_{11} \end{pmatrix} R_{ver} = \begin{pmatrix} R_{22} & R_{23} \\ R_{32} & R_{33} \end{pmatrix}$$

where R_{hor} and R_{ver} are the horizontal and vertical focusing of the element.

For a single ion on a reference trajectory with a closed path, such as in a storage ring, a slice of the phase space, e.g. (x, x'), traces an ellipse. The area of this ellipse, known as the *emittance*, is a constant of motion as long as only conservative forces act on the beam, which do not have mixed dependence on transverse or longitudinal motions. Similarly, the conditions of the collective ion beam at a point along the trajectory can be monitored in terms of the emittance profile, ϵ. Figure 2.20 shows the emittance profile for an ion beam converging in the x direction.

Just as for trapped ions, bunched ion beams exhibit a mutual repulsion due to their charge. The repulsion acts non-conservatively and leads to an increase in emittance along the reference trajectory. This space charge effect is particularly strong for low-energy beams. In addition, non-conservative forces such as net deceleration within a pulsed electrostatic component can drastically increase the emittance.

2.7.1 Einzel lens

An einzel lens is an electrostatic component that focuses ions without changing their energy. This is generally accomplished by a cylinder at some potential that has grounded cylinders on either end to form two lens elements between the gaps. In this configuration, the transfer matrix can be considered the product of the matrix of the decelerating and accelerating fields (or vice versa for a lens of opposite polarity). Focusing in the vertical and horizontal directions are equivalent, and although there is no finite expression of the focusing strength of a real lens, their simplicity makes their implementation in electrostatic beamlines ubiquitous. Generally focal lengths of a few times the lens length occur for lens potentials a few times the beam potential, its kinetic energy per charge. Figure 2.21 shows the expected focal length in terms of the lens length for a range of lens potentials in terms of the beam potential. This also shows the effect of narrowing the ground electrodes to

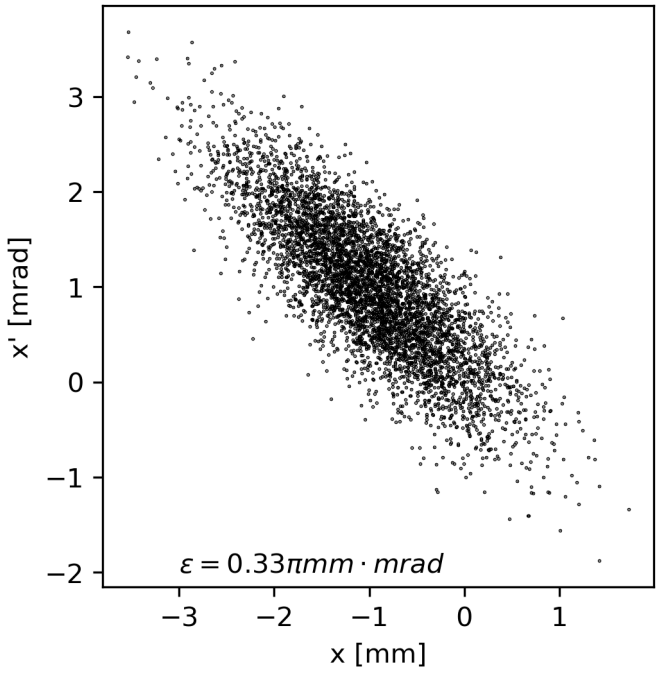

Figure 2.20: Typical emittance profile of a converging ion beam. Each point represents a slice of a particular ion's position vector. In the example the ion beam has a 2D emittance of 0.33π mm · mrad.

form an aperture. The focusing strength increases as the aperture size decreases. This is especially critical for accelerating lenses, where the lens potential is the opposite polarity to the beam, which provides weaker focusing but suffers lower spherical aberrations [92].

2.7.2 Quadrupole doublet

A quadrupole doublet is an ion focusing element that uses a quadrupolar field to focus in one plane while defocusing in the other, these elements are paired in alternating doublets to achieve net focusing in both directions. This is depicted in figure 2.22. The transfer matrix elements for the focusing and defocusing planes of a single quadrupole field at first order are given in 2.36 where $\pm V_{QD}$ is the potential applied symmetrically to the elements of the doublet and d is the dimension of the electrode as shown in figure 2.22 [93].

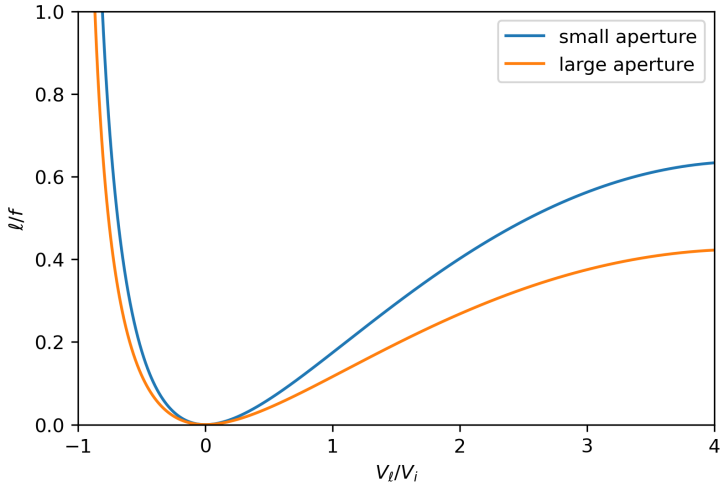

Figure 2.21: The focal length of an einzel lens, f, in terms of its length, ℓ. For a range of lens potentials V_ℓ in terms of the beam potential V_i. The effect of the aperture size is shown for apertures much smaller than the lens diameter and for apertures near the lens diameter.

$$R_{focus} = \begin{pmatrix} cos(sk^{1/2}) & k^{-1/2}sin(sk^{1/2}) \\ -k^{1/2}sin(k^{1/2}s) & cos(k^{1/2}s) \end{pmatrix}$$
$$R_{defocus} = \begin{pmatrix} cosh(k^{1/2}s) & k^{-1/2}sinh(k^{1/2}s) \\ -k^{1/2}sinh(k^{1/2}s) & cosh(k^{1/2}s) \end{pmatrix} \tag{2.36}$$
$$k = \frac{V_{QD}}{d^2 V_i}$$

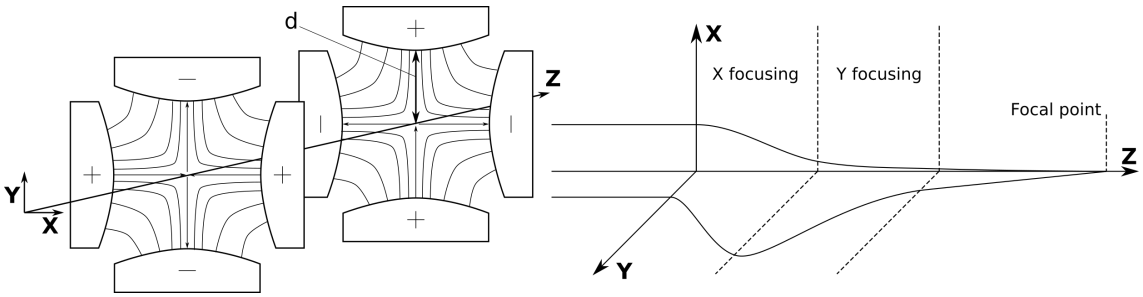

Figure 2.22: (left) the quadrupole fields of a quadrupole doublet transverse to the reference trajectory. (right) the ideal effect on the beam envelope first focusing in one dimension then the other.

2.7.3 Quadrupole bender

If the ion beam is instead in the plane of a quadrupole the net effect is bending the beam along the field lines. Quadrupole benders are particularly useful when switching the incoming or outgoing direction of the ion beam as this is a simple switch of the polarity or grounding of the electrodes for a given beam energy. Bending focuses the beam in the bending plane, and for bending elements sufficiently larger than the ion beam, acts like

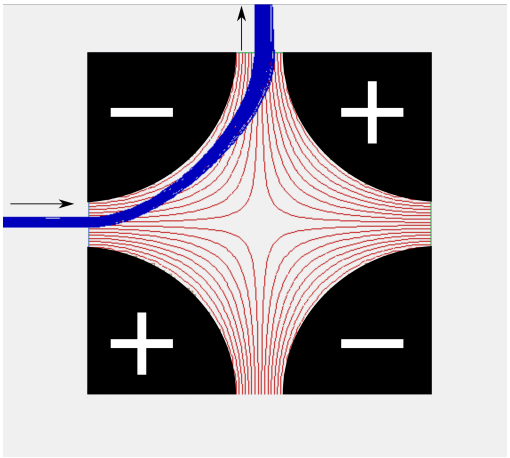

Figure 2.23: Simulation of an electrostatic quadrupole bender. The red lines are contours of the electrostatic potential created by the electrodes (black) with indicated polarity. The blue lines represent the individual trajectories of an ion bunch deflected by the electrostatic field.

a drift region in the transverse plane. This often contributes to astigmatism in the beam profile after bending. Figure 2.23 shows a simulation of a quadrupole bending element in SIMION [2]. Such simulations appear in the analysis of the design of beamline components in chapter 4.

2.7.4 Spherical bender

A spherical bender is made from sections of two concentric spherical surfaces, usually at 90° bending angle and a width that is a portion of the radius. The reference trajectory is taken at the midpoint between the two surfaces on the plane of symmetry with radius of curvature ρ. The focusing matrices are

$$R_{hor} = R_{ver} = \begin{pmatrix} cos\left(\frac{s}{\rho}\right) & \rho sin\left(\frac{s}{\rho}\right) \\ -\rho^{-1} sin\left(\frac{s}{\rho}\right) & cos\left(\frac{s}{\rho}\right) \end{pmatrix} \tag{2.37}$$

for a sufficiently large bending radius at low-energy. There is simultaneous focusing in the vertical and horizontal directions. Spherical benders also cause longitudinal separation for bending angles less than 90° . Taking the bending plane to be horizontal the values for the longitudinal separation are:

[2] SIMION is a finite difference solver for the Laplace equation with specified boundary conditions as well as for the trajectories of charged particles within those fields.

$$\begin{aligned} R_{40} &= -sin\big(\frac{s}{\rho}\big) \\ R_{41} &= \rho(cos\big(\frac{s}{\rho}\big) - 1). \end{aligned} \tag{2.38}$$

For an 80° bend at 200 mm this gives $R_{40} \approx 0.98$ and $R_{41} \approx -0.165$ mm $\cdot$ mrad^{-1}. That is to say, a bunch is elongated by 98% of its width and ions entering at an angle take an alternate path through the bender exiting 165 mm behind the reference for every radian below the reference they enter. Finally, the dispersion is also increased for smaller bending angles:

$$\begin{aligned} R_{05} &= 4\rho\big(1 - cos\big(\frac{s}{\rho}\big)\big) \\ R_{15} &= 4sin\big(\frac{s}{\rho}\big) \\ R_{45} &= 4\rho sin\big(\frac{s}{\rho}\big) - s \end{aligned} \tag{2.39}$$

Taking again an 80° bend at 200 mm this gives $R_{05} = 661$ mm, $R_{15} = 3.94$ rad, and $R_{45} = 509$ mm. This indicates that the change in path of ions of different energies can be quite drastic and control over the energy spread before bending is critical. For example an ion with 2‰ higher energy (1‰ higher momentum) relative to the reference is 1.3 mm and 7.8 mrad less deflected than the reference and 1.0 mm behind it.

2.7.5 The Magnetic Mirror

For injection of charged particles into the magnetic field of the Penning trap, it is important to also consider the alignment of the beamline to the magnetic field. Charged particles undergoing cyclotron motion exhibit a macroscopic magnetic moment μ due to their orbit, which is adiabatically invariant:

$$\mu = \frac{mv_\perp^2}{2B}, \tag{2.40}$$

where $v_\perp$ is the velocity of the particle perpendicular to the magnetic field. As the particle enters a region of higher magnetic field the perpendicular velocity increases. However, its total kinetic energy is unaffected, and the velocity parallel to the field must therefore decrease. This is known as the magnetic mirror effect and is the confinement principle behind a magnetic bottle. Particles with a pitch angle, θ above a critical value θ_c are decelerated completely and reflected. Here B_{last} is the magnetic field strength at the last electrostatic component after which ion trajectores are pinned to the magnetic field lines completely.

$$\begin{aligned} \sin\theta &\equiv \frac{v_\perp}{v} \\ \sin\theta_c &\equiv \sqrt{\frac{B_{last}}{B_{max}}} \end{aligned} \tag{2.41}$$

Chapter 3

The ARTEMIS Apparatus

The **a**symmet**r**ic **t**rap for the measurement of **e**lectron **m**agnetic moments in **i**on**s** (ARTEMIS), is a precision laser-microwave double-resonance spectroscopy experiment implemented in a Penning trap under low noise and cryogenic conditions. It consists of several subsystems that all must operate together for successful measurements. As an end user of the accelerator at GSI, it also relies heavily on the infrastructure of the facility. The scope and interconnection of the entirety of the experiment makes it difficult to provide a concise overview; however, figure 3.1 attempts to give a conceptual map of the various systems that contribute to the experiment as a whole. This chapter will then describe the systems and their interconnections in more detail.

Throughout the course of this work the design of the experiment was altered significantly to allow external injection. Prior reports on ARTEMIS extensively covered the method of gas injection using a cryogenic chamber that could release cryosorbed argon gas into the trap chamber, hereafter referred to as the cryovalve. [64–66]. This system was replaced by the fast-opening cryogenic valve (FCV) which allows injection of ions from external sources as well as repeated irradiation of light up to the UV range, while maintaining the excellent temperature and vacuum conditions of the experiment. The upgrades will be covered completely in chapter 4 although the descriptions of the apparatus throughout will inevitably reference both the old design as well components of the new beamline.

Figure 3.1: An abstract overview of the major subsystems of ARTEMIS and some of their components.

3.1 GSI Helmholtzzentrum für Schwerionenforschung

In order to measure the most highly charged systems ARETMIS will utilize the world unique capabilities of the accelerator facility at GSI which can produce ionic charge states up to bare Uranium. Figure 3.2 is a rendering of the complete facility and its surroundings.

Ionization energies for heavy hydrogenlike ions are on the order of 100 keV or more, although delivering this energy to the bound electrons requires significantly higher ion beam energies. This high charge ionization is accomplished by first accelerating the host

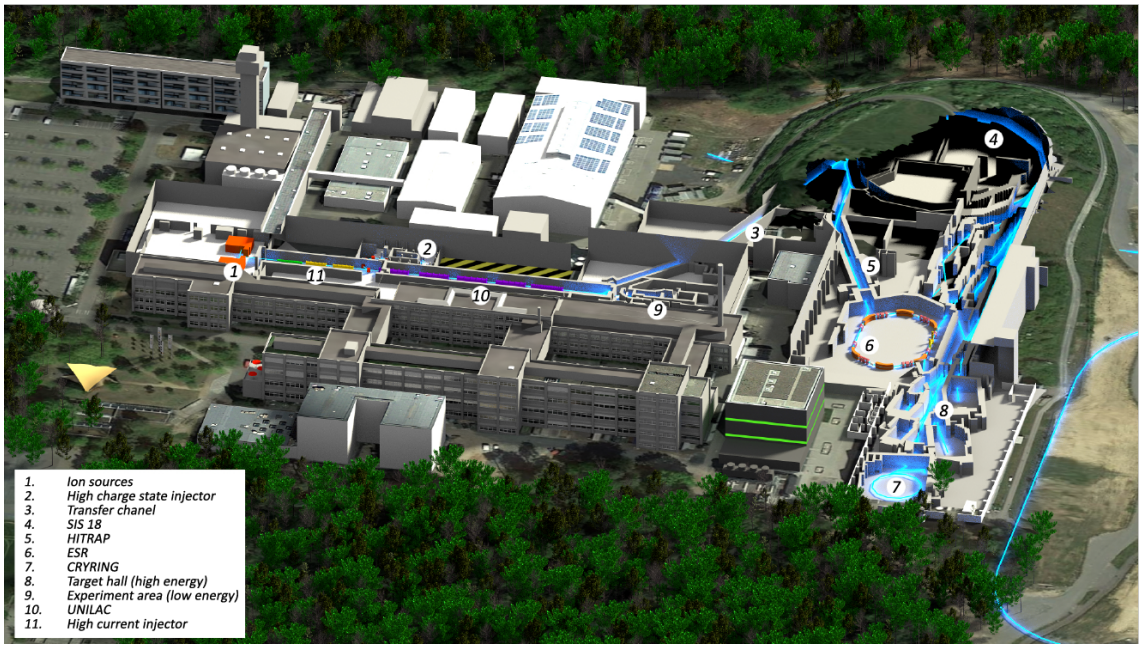

Figure 3.2: A rendering of the complete GSI accelerator facility, highlighted by the blue glow as well surrounding buildings. Some of the key accelerator components are labeled. ARTEMIS is on the platform above the HITRAP decelerator, labeled as 5.

ion then passing it through a thin foil target to remove electrons. As acceleration is easier at higher charge, this process can be repeated at higher energies to produce yet higher charge states. Long term study and storage of HCIs then requires deceleration after stripping. Providing a bunch of heavy highly charged ions for capture in ARTEMIS consists of several steps [94]:

- A source material is ionized in vacuum inside the one of the ion sources (1). GSI has 6 ion sources that can accommodate a wide range of source elements and beam conditions. The intensity of the sources are lower for higher charge states. Extraction from the sources produces a continuous beam of ions.
- The ion beam flows to the universal linear accelerator (UNILAC, 10). Here it is divided into discrete bunches and passed through a gas stripper target. Then 5 acceleration stages reach speeds up to 0.155c and additional stripper targets produce charge states up to 72+.
- The bunches are transferred to the heavy ion synchrotron (SIS 18, 4) for further acceleration up to a beam rigidity of 18 Tm or up to 0.90c.
- After extraction from the SIS, the final ionization takes place in strippers within the high energy beamlines that connect to the experimental storage ring (ESR, 6). Ionization up to bare uranium, 92+, is possible.

- The ESR decelerates ion bunches by sympathetic cooling with a parallel electron beam down to energies as low as 4 MeV per nucleon [95]. From here ions are extracted to the HITRAP decelerator (5).
- HITRAP decelerates ions to be captured in the cooler trap where cold electrons sympathetically cool them to 4 K. Extraction from the HITRAP cooler trap takes place at a few kV, and ions are transfered up one floor to the low-energy beamline.
- Finally ions from the low-energy beamline can be injected into ARTEMIS where they are captured in flight. This will be covered in more detail in Chapter 4.

3.1.1 HITRAP

HITRAP is a decelerator facility designed to facilitate experiments in heavy HCIs at the lowest energies. It extracts HCIs from the ESR and decelerates them from 4 MeV per nucleon to the sub-eV range. Figure 3.3 shows the relative energies of the low-energy facilities at GSI/FAIR. It is connected to a low-energy beamline with locations for multiple experiments to use HITRAP as a source [96]. It also has its own electron beam ion trap (EBIT) from DREBIT that can be used as an alternate ion source of light or medium HCIs between beamtimes from the ESR [97].

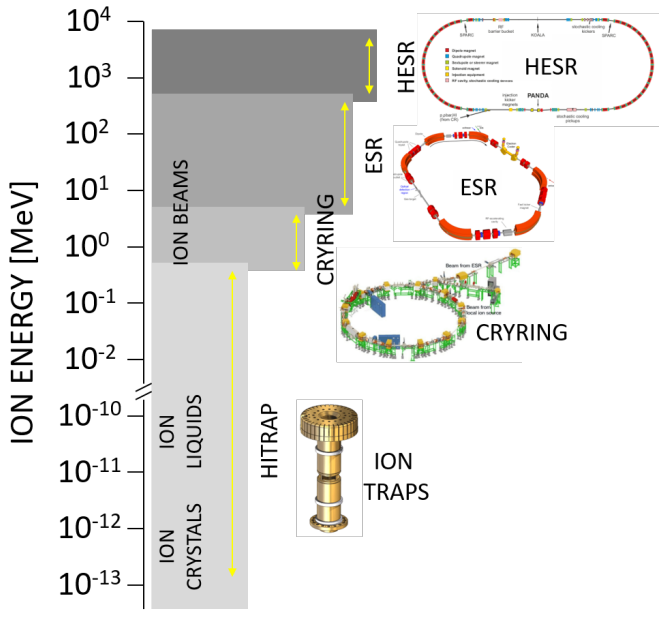

Figure 3.3: Accessible energy ranges for experiments with ions at low-energy at GSI/FAIR. HITRAP is designed for HCIs at the lowest currently possible energies.

The decelerator itself consists of three sections: a rebunching stage, two linear deceleration sections, and the cooler trap. Figure 3.4 shows the sections of the HITRAP decelerator and the respective ion energies at each. The double-drift buncher shapes the ion bunches ejected from the ESR to improve the acceptance into the decelerators. The first linear

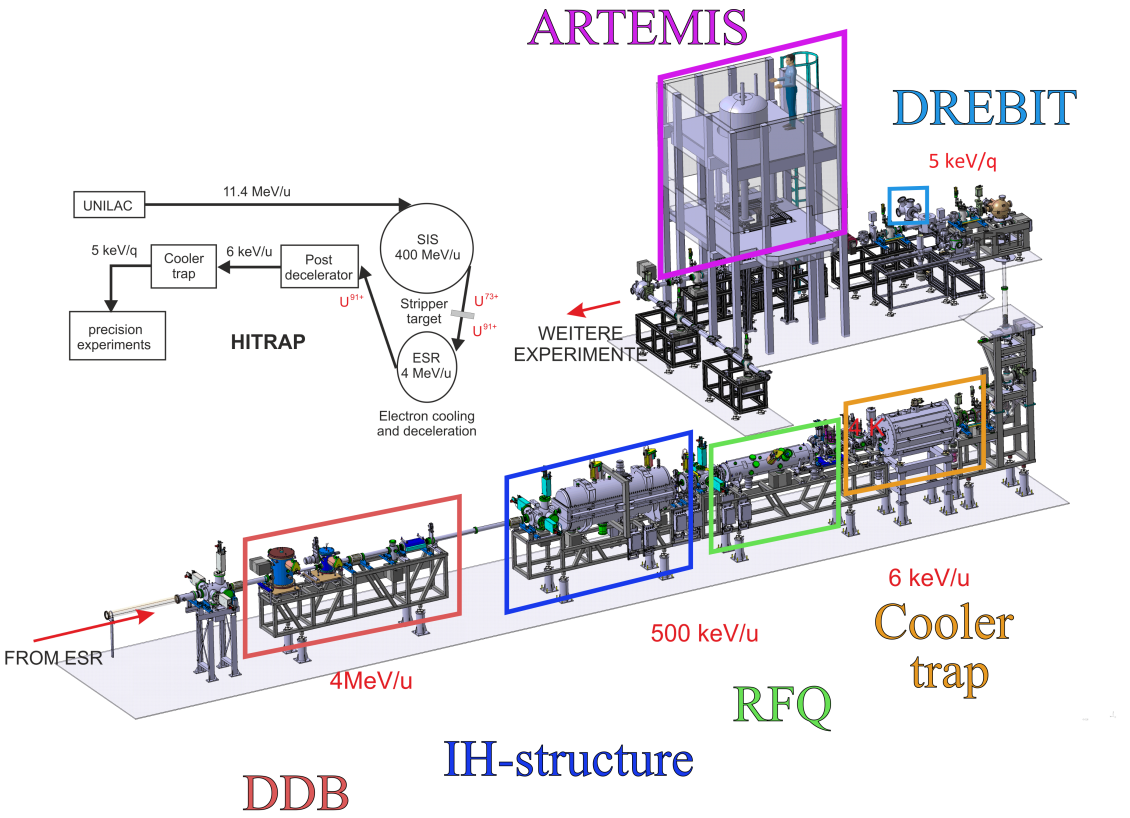

Figure 3.4: A schematic of the HITRAP decelerator. The individual sections are highlighted. The low-energy beamline and ARTEMIS on the upper platform are also shown. The inset outlines HITRAP in the context of the full GSI accelerator.

decelerator is an interdigital H-type structure that reaches 500 keV per nucleon, and the second is a radio frequency quadrupole that decelerates to 6 keV per nucleon. The HITRAP cooler trap is a Penning trap that captures the ions in flight and sympathetically cools them with simultaneously trapped electrons without recombination [98]. The ions are therefore essentially fully decelerated, but the cooler trap also reduces the extremely high emittance that is a consequence of the deceleration and space charge. Ions can be extracted from the cooler trap into the low-energy beamline which sends them up to the platform above where the experiments are located [99].

The low-energy beamline is designed for transport of HCI bunches at a few kV drift potential over several meters for delivery to experiments. The main challenges are interactions with the rest gas and increasing emittance due to space charge. The beamline is maintained at about 10^{-9} mbar by regularly spaced turbomolecular or ion getter pumps, and the ion beam is repeatedly refocused about every meter by einzel lenses or quadrupole doublets. A full description of the low-energy beamline is given in [96]. Figure 3.5 is a schematic of the low-energy beamline between the vertical channel from the cooler Pen-

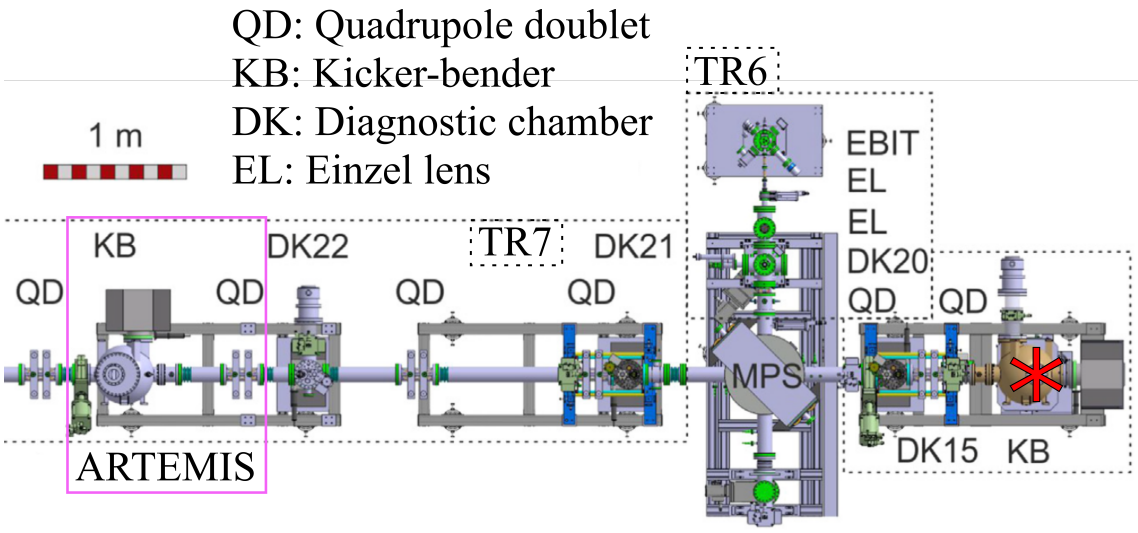

Figure 3.5: A schematic of low-energy beamline of HITRAP between the vertical line from the decelerator level (red asterisk) and the vertical beamline op the ARTEMIS tower. The beamline is divided into subsections for labeling components. TR6 and TR7 are two such sections shown here. The multi-pass spectrometer (MPS) has been recently replaced by a electrostatic quadrupole bender. The SPARC EBIT as well as ion optics components are labeled. Figure modified from [96].

ning trap and the vertical beamline of ARTEMIS.

3.2 Vacuum and Cryogenic Setup

The core of the ARTEMIS apparatus is the trapping region where the HCIs are stored for spectroscopy. As described in section 2.6 the conditions in this region are essential to the operation of the experiment. Therefore the design uses of layers of vacua and cryogenic shielding, and any connections to the external environment are carefully considered to reduce their impact on the trap environment. Figure 3.6 is a cut-away drawing of the entire apparatus without the beamline. The outermost layer is a magnet and its surrounding cryostat. The trap components are inserted into the bore of the magnet which is warm. They are therefore surrounded by an aluminum radiation shield, which is covered by multi-layer insulation (MLI) foil. This shield is kept at 40 K by a SUMITOMO RP-082 pulse-tube cryocooler at the top of the experiment. Inside the shield is another vacuum chamber, the trap chamber, which is connected to the 4 K stage of the cryocooler by thick copper rod and stacks of copper braiding such that the inner trap electrodes are positioned in the peak of the magnetic field. The apparatus is supported above the low-energy beamline of HITRAP as shown in figure 3.4 by an aluminum frame such that the ions can be injected from below.

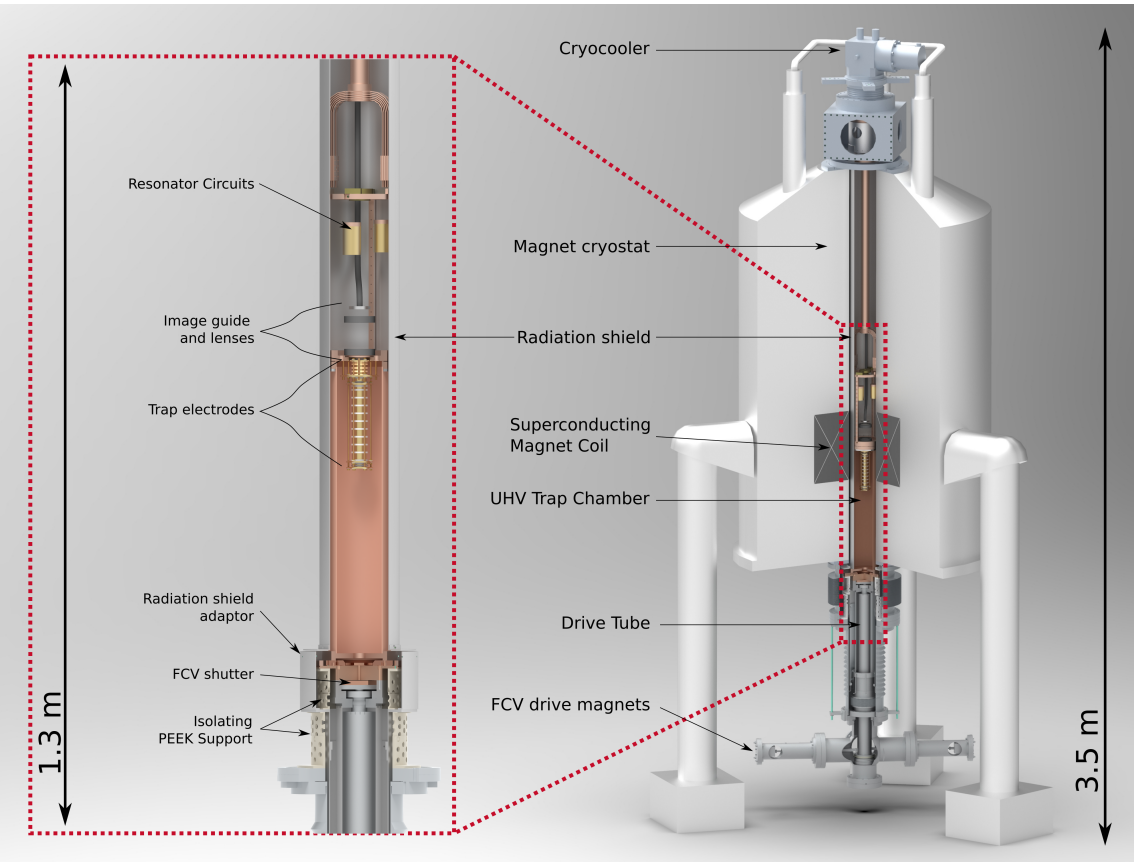

Figure 3.6: A complete drawing of the ARTEMIS apparatus. The inset gives a closer look at the interior components without the superconducting magnet and its cryostat. Some major components are labeled.

The coupling between the trap chamber and the beamline utilizes a specially designed valve (FCV) that is discussed completely in chapter 4. The entire setup is surrounded by a wooden tower to support the connected experimental electronics and data collection devices without interfering with the magnetic field.

The superconducting solenoid magnet produces the magnetic field of the trap at 7 T. It was produced by VARIAN, model number 7T160, and uses a NbTi wire to form the solenoid core as well as 8 superconducting active shim coils. These enable ultra low field gradients at the magnet center of less than 0.1 ppm/cm^3 and temporal stability less than 1 ppm/h. The superconductors are submerged in a 300 L liquid helium (LHe) reservoir which is surrounded by a 240 L liquid nitrogen (LN_2) reservoir. The walls of both reservoirs are vacuum insulated which reduces the heat load to the cryogenic liquids such that LN_2 needs to be refilled about every 14 days and LHe every 8 months. The magnet has been continuously energized at 210 A since 2009 with detailed measurement of the field strength determined from the ion motion given in [65].

The bore of the magnet is a cylinder, 173 cm long by 16 cm in diameter. On either end, vacuum flanges with Viton o-rings allow the bore to act as an isolation vacuum for the interior cryogenic components. A small extension of the vacuum chamber on top of the magnet allows feedthrough of connections to the interior electronics and spectroscopy components. It also houses the connection for the turbomolecular pump and cryocooler. Inside this section the radiation shield and copper rod are coupled to the cryocooler. Interior connections pass through small holes in the shield which are surrounded by MLI, and the interior is pumped down to about 10^{-7} mbar.

The magnet bore houses the electronics for ion detection and manipulation. Having these electronics as close as possible to the trap is essential for receiving signals with high signal to noise ratios. They are connected to the feedthroughs at the top with thin constantan wires which are thermally anchored to sapphire thermocouples on both the 4 K and 40 K temperature stages to minimize the thermal load to the electronics. There are three resonator circuits for particle detection which are custom built at ARTEMIS and two filter boards (custom made by STAHL ELECTRONICS) that remove high-frequency noise from any connections that are fed into the trap chamber and separate the DC trap biasing from the AC signals used for ion detection and manipulation. Figure 3.7 is a photo of the electronics mounted directly above the trap chamber. This section is referred to as the 4-leg section due to the shape of the structural OFHC components. The laser fiber and imaging system are also visible and will be covered in section 3.5.

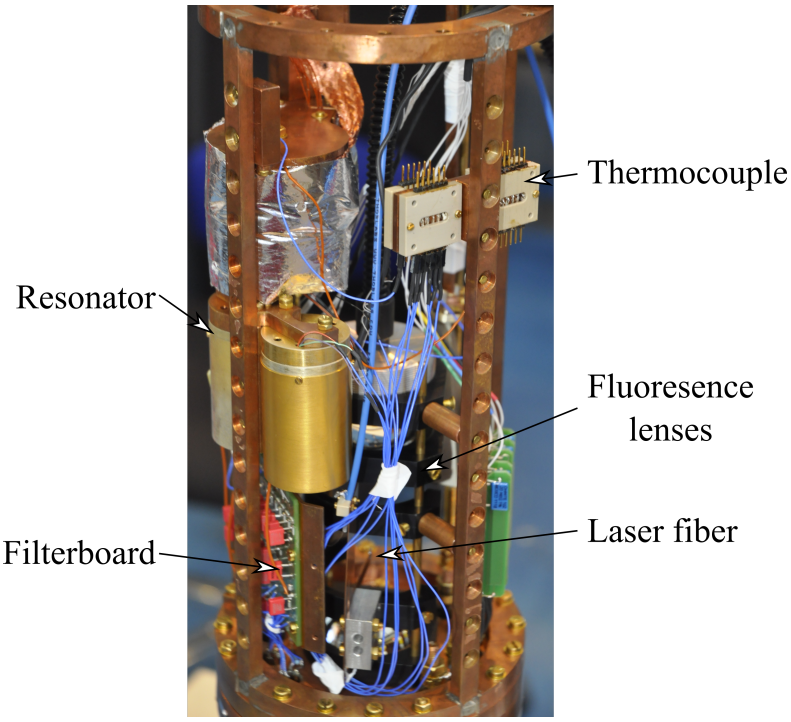

Figure 3.7: A photo pf the electronics mounted directly above the trap chamber in the cryogenic environment. Photo taken by [65].

3.3 The Trap Stack

Inside the trap chamber hangs the stack of electrodes that generate the confining electrostatic field. ARTEMIS can be divided into two distinct trapping regions: the precision spectroscopy trap (ST) and the larger high-voltage creation/capture trap (CT). The advantage of this design is that the ST can be compact with ultra low field gradients and electronic noise, and exceptional spectroscopic access. The CT has a wider range of applications such as in-trap ionization, a wider range of trap potentials and therefore of detectable ion species, fast switching of electrodes at high voltage for in flight capture, and selective rejection of ion species. Ions initially trapped in the CT can be transported to the ST near adiabatically. The added heat can only be measured after many successive transports between the two traps [65]. Figure 3.8 gives a drawing of the entire stack of electrodes and their labeling scheme as well as a photo of the electrode stack before installation in the trap chamber.

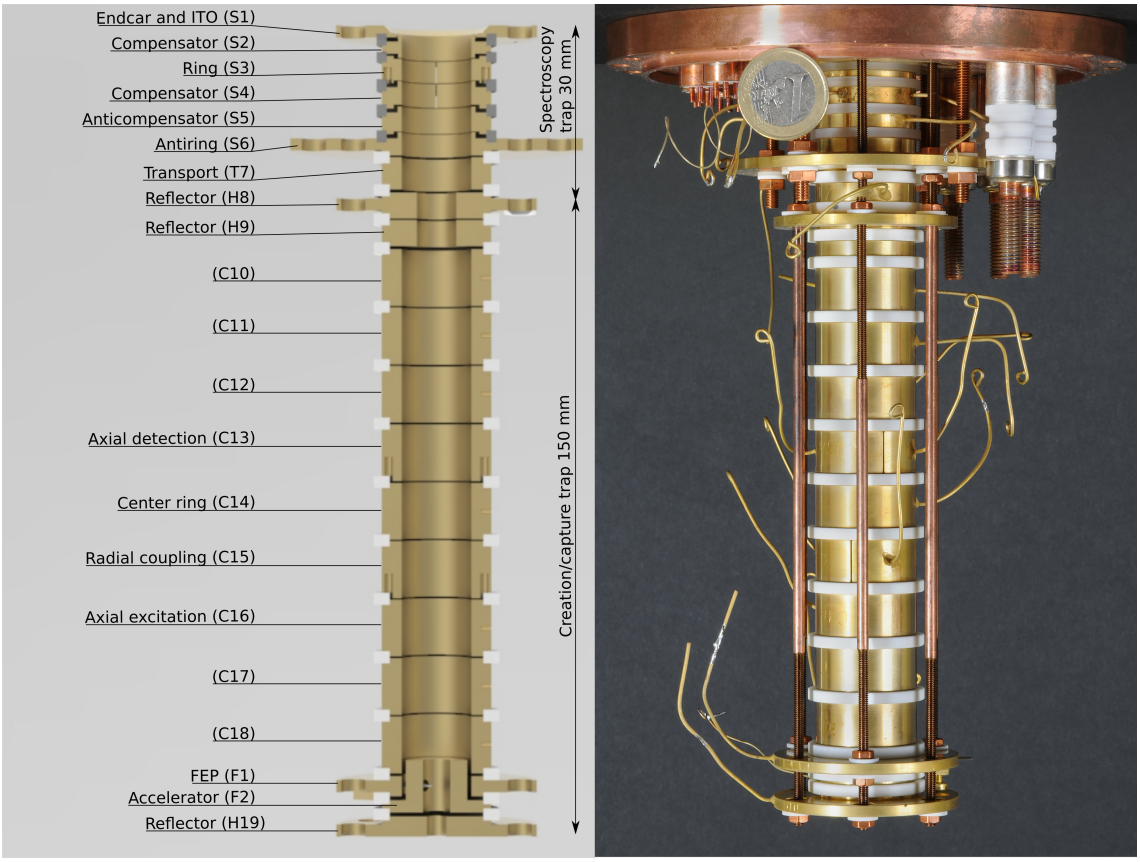

Figure 3.8: (a) a drawing of the stack of electrodes in ARTEMIS. It can be divided into two sections, the ST and CT, which are connected by a transport electrode. Also shown are the labeling scheme and some specific applications for electrodes. (b) a photo of the electrode stack before installation.

Table 3.1: Dimensions of ARTEMIS electrodes at 4 K

Electrode/Space	Height [mm]	Inner Radius [mm]
S2	5.87	8.70
S2 - S3	0.19	-
S3	5.36	8.70
S3 - S4	0.19	-
S4	5.87	8.70
S4 - S5	0.20	-
S5	6.20	8.70
S5 - S6	0.40	-
S6	5.71	8.70
S6 - T7	0.20	-
T7	7.97	8.70
T7 - H8	0.51	-
H8	6.48	4.96
H8 - H9	0.41	-
H9	6.48	4.96
H9 - C10	0.70	-
CT space	0.40	-
CT electrodes	14.1	8.70

The trap electrodes are made of OFHC copper that are gold plated with a 20 µm diffusion barrier of silver. The electrodes of the ST are precision machined with micrometer tolerance, but the thermal contraction is only given in this work to 3 digits of precision. In the ST they are separated by sapphire rings and in the CT by Macor rings. The two traps are assembled independently and then mounted to the top flange of the trap chamber with threaded copper rods to ensure that there is even contraction as the assembly cools. A detailed account of the trap geometry is given in [65] and the dimensions at 4 K including the gold and silver layers are given in table 3.1.

3.3.1 Half-open Penning trap

The ST is designed to allow the most precise measurements of the ion motions as well as spectroscopic transitions. Therefore it should have good access for laser spectroscopy and fluorescence detection, low field imperfections, and a compact size for maximum homogeneity of the magnetic field and good ion detection. This combination of functions is made possible by a half-open trap with two design adaptations: the antitrap and the conductive ITO window. The ST is electrically compensated and orthogonalized. Split electrodes (S3 and S4) allow application of magnetron centering and the rotating wall technique to increase the density of the plasma in the laser path for maximum luminescence.

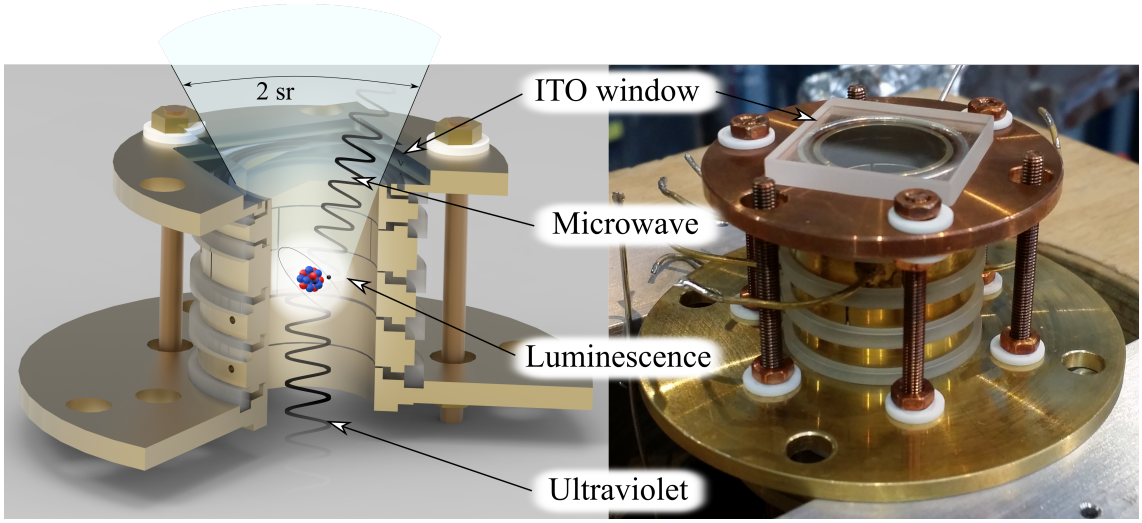

Figure 3.9: (left) a drawing of the ST with the cone of light emitted by ions trapped in the center (ion cloud size is not to scale). The solid angle from the trap center to the opening of the trap is about 2 sr. (right) a photo of the complete assembled ST with the ITO coated window on top.

The cyclotron resonator (CRES) is connected to one side of S4 and the axial resonator (ARES-ST) is connected to S2. These resonators will be covered in section 3.4. The electrodes are biased through the filter boards by a HV200-8 voltage supply from Stahl Electronics.

As described in 2.4, to have small imperfections of the electrostatic field, cylindrical Penning traps use long endcaps. Therefore, normal cylindrical Penning traps have about a 0.2 sr solid angle for light emitted by ions at the trap center to escape the endcap opening. The ST uses a half-open design, where ions can be injected from below, and a closed endcap on top allows it to be much closer to the trap center without inducing significant field imperfections. The endcap is optically transparent to allow spectroscopic access and is coated with a conductive layer to provide the trapping potential. This improves the solid angle for emitted light to about 2 sr, an increase of an order of magnitude. Figure 3.9 shows a drawing of the ST, highlighting the angle of the emitted light cone, as well as a photo of the ST with the transparent electrode on top.

The antitrap

To generate the harmonic potential in the half-open trap and decrease the transport length for ions from below, the concept of the antitrap is used. In this configuration the compensation and ring potentials are inverted and reflected to the opposite side by corresponding anticompensator and antiring. This is depicted in figure 3.10. The details of the fields and

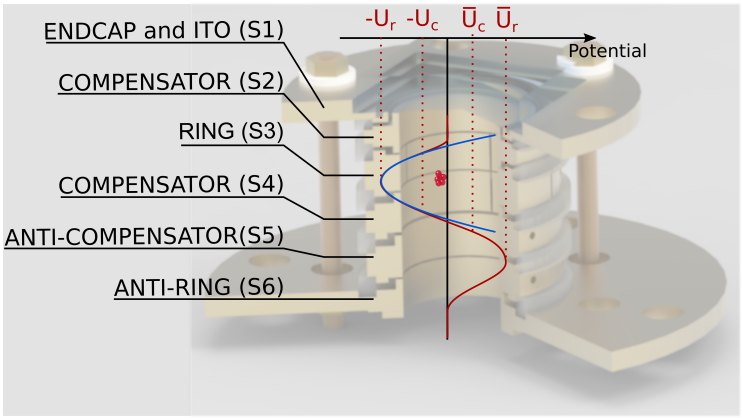

Figure 3.10: The concept of the antitrap. The red curve shows the shape of the center line potential in the ST and the blue curve is the ideal hyperbolic shape. The anticompensator and antiring electrodes have the opposite potential to their counterparts.

calculation of the geometries are given in [18]. The resulting coefficients of the electrostatic field expansion are $C_2 = 0.5229$ and $C_4 < 0.001$. The compact trap also enables slow transfer of ions from the CT. Long endcaps have almost no field gradient along their length, so even for relatively slow transfer the ramping potential has a much higher probability of accelerating the ions during transport.

Rotating wall technique

The ring of the ST (S3) is split into four equal segments precisely separated by sapphire spheres. These four electrodes enable application of the rotating wall technique [100], which allows radial compression of the trapped plasma by application of a rotating electric field in the direction of the cyclotron motion. The induced acceleration of the plasma rotation increases the magnetic Lorentz force and compresses the plasma radially. The ion density is given by

$$n = \frac{2\epsilon_0 m\omega(\omega_c - \omega)}{q^2}, \tag{3.1}$$

where ω is the plasma rotation frequency as driven by the rotating wall. Compression can be induced up to the Brillouin limit, which in the ST is 600 billion Bi^{82+} ions. In ARTEMIS this has the advantage of increasing the intensity of the fluorescence light emitted from ions in the center of the trap.

Magnetron centering

S4 is similarly split into two halves for application of radial dipole fields. These are useful for stimulating the radial motions or coupling them to each other or the axial mode. Application of a dipole field on half of S4 at $\omega = \omega_z + \omega_-$ or of a quadrupole field on all four segments of S3 at $\omega = \omega_+ + \omega_-$ results in exchange of energy between the respective

modes, referred to as resonant motional coupling. Such a coupling between the magnetron motion and either the cyclotron or axial motions while simultaneously resistively cooling the second motion, results in a net movement of ions up the ladder of magnetron states discussed in 2.4.2. As the energy of the magnetron motion is negative the resulting motion is an inward spiral of the ions toward the trap center. This procedure is therefore known as magnetron centering. In ARTEMIS, this is essential to ensure that the ion cloud overlaps the laser on the trap axis.

The conductive ITO window

The transparent electrode at the end of the ST, a WTSQ11050-A conductive window by THORLABS [101], consists of a N-BK7 substrate with an anti-reflective coating (350 - 700 nm) on one side and a indium tin oxide (ITO) coating on the other. ITO is an n-type semiconductor with a large band gap, allowing transmission of light deep into the optical regime. The exact properties of the window depend on the doping. Figure 3.11 shows the transmittance of the ITO window in ARTEMIS as a function of the wavelength of incident light. The measured surface resistivity of the ITO layer from corner to corner is 150 Ω at 4 K. For measurements in Ar, the ITO allows sufficient transmission of 441 nm light of 77%, but the transmission falls off for shorter wavelengths. Therefore, a new window is being developed for the measurements in bismuth. The new window will use a fused silica substrate with a graphene coating which is transparent to UV light [102, 103].

The ITO window also serves as the target for tuning the injection and capture parameters for ions from HITRAP. Therefore, its performance as a target material was tested before installation. It is important to ensure that the ion beam from the low-energy beamline does not destroy the ITO coating. The window was bombarded with ions from an

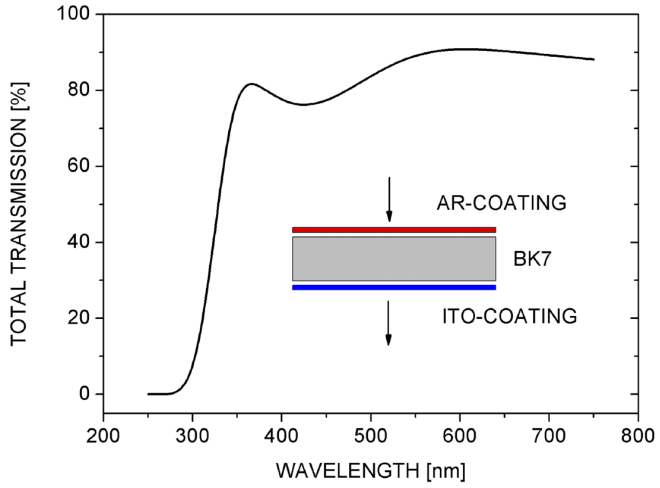

Figure 3.11: The transmission through the ITO window as a function of the wavelength of incident light in the near UV to near IR range. The inset graphic is a drawing of the WTSQ11050-A conductive window with the anti-reflective and ITO coatings. Data from [101].

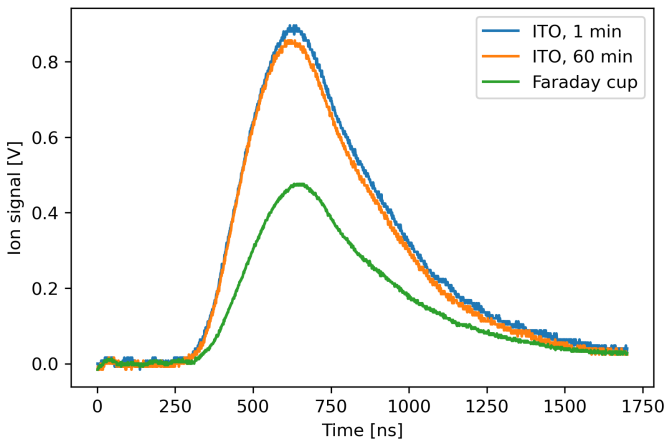

Figure 3.12: The response of the ITO to bombardment by an ion beam was measured initially and after 60 minutes of constant beam exposure. This is compared to a typical Faraday cup. The difference in signal height comes from the relative impedance of the ITO. After an hour of bombardment, there is only a small reduction of the signal height.

EBIT 450 times while measuring the induced signal with a fast transimpedance amplifier from FEMTO. This signal, both initially and after 60 minutes, is compared to the same ion beam impacting a typical Faraday cup in figure 3.12. The increased signal height is due to the higher surface resistivity compared to the copper Faraday cup. This signal shape is otherwise the same indicating that the ITO is sufficient for time sensitive detection but calibration would be required for true beam current measurements. After one hour, there was only minimal degradation of the signal indicating that the ITO will be a robust target for injection.

3.3.2 The creation/capture trap

The CT is designed to augment the set of functions available to the experiment without limiting the precision of measurements in the ST. To that end it enables in-trap creation of ions from residual gas atom, in-flight capture of ions from an external source, storage of a large cloud of exotic ions for extraction of small ion numbers to the ST, and a wider range of applicable trap potentials as well as fast switching of potentials.

The CT is made of 9 electrodes of the same dimensions (C10 - C18) surrounded by high voltage *reflector* electrodes with narrower inner diameters (H8, H9, H19) and an electron source on the end opposite the ST (F1 and F2). The inner electrodes apply the antitrap principle similar to the ST, where opposite potentials are applied to alternating electrodes to form three axial wells centered on C14. In this configuration of potentials, the trap has $C_2 = 0.5631$ and $C_4 = 0.001$. Note that this is possible due to the choice of electrode geometry, which taking into account the spacing, makes them mechanically compensated. Similar to the ST, electrodes C13 and C15 are split into two halves to allow radial dipole excitation or motional coupling, although currently the two halves of C13 are purposely connected to form a single electrode. The axial resonator (ARES-CT) is

connected to C13.

The filters on the CT electronics are somewhat wider, 1 ms characteristic time, allowing fast switching of electrode potentials including the reflectors. The exception being H8 and H9 which currently switch between two voltage sources depending on the application. This switching is controlled by a relay which is sensitive to high voltage. This is useful for ejection of contaminating ion species from the trap or for in-flight capture enabling of ion beams up to almost 2 kV beam potential, significantly easing the need for preliminary deceleration.

For ejecting contaminants, the center ring is pulsed briefly to same potential as neighboring electrodes, which breaks the confining condition of the electric field. Any ions with significant kinetic energy escape the trapping region during this pulse while other ions are too slow to avoid being *retrapped* as the potential drops back down. Contaminants are selectively excited according to their motional frequency by an axial dipole field. This procedure is often referred to as stored waveform inverse Fourier transform (SWIFT) as it creates a time domain signal from the measured ion frequency [104]. In ARTEMIS it is often simpler and equally effective to use a series of frequency bands around each contaminant's motional frequency. A detailed analysis of the application of SWIFT to the CT was done in [65]. It is implemented regularly at ARTEMIS to produce trapped ion clouds of only a single species. Figure 3.13 shows a charge to mass spectrum collected in the CT from a cloud of several Ar charge states before SWIFT compared to the same cloud of only Ar^{13+} after SWIFT.

The reflector electrodes can be biased up to ± 2 kV and have a narrower inner diameter to limit the field penetration from the low voltage regions. When negatively biased they serve to form an outer Penning-Malmberg trap for high energy electrons, into which the three wells of the CT are nested. This configuration is shown in figure 3.14 where electrons are confined within the entire length of CT and ions are confined in three inner wells.

The field emission point (FEP, F1) and associated accelerator (F2) comprise the electron source. The FEP is a tungsten needle, about $1\mu m$ in diameter at its point, mounted to the supporting electrode that sits in the stack. The tip protrudes through a hole in the accelerator electrode which closely surrounds the tip. Scanning electron microscopy of the tip reveals that it has micro-structure tips with curvatures as low as tens of nanometers. When paired with a voltage difference of a few kV between the FEP and the accelerator, this small curvature generates extreme electric fields at the tip surface. The induced Schottky effect creates a significant probability of electrons in the tip tunneling into the field. To this end tungsten was chosen for the tip for its low work function, the energy required to eject an electron at the Fermi level from the conductor.

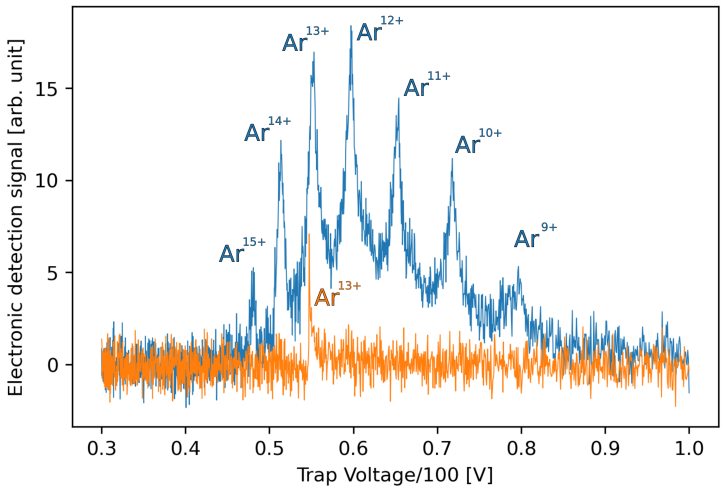

Figure 3.13: The q/m spectrum of several charge states of argon is compared to the spectrum of only Ar^{13+} left after SWIFT is used to remove all other charge states.

The FEP in ARTEMIS can be used to generate electron currents of hundreds of nA at up to 2 keV. The primary purpose of the FEP is for creating ions inside the trap volume from residual gas atoms by electron impact ionization. Combined with a source of argon gas, this allow ARTEMIS to be completely independent of external ion sources for g-factor measurements, although ions can be generated from any elements present in the trap. Electrons could also be used for excitation of laser-inaccessible states by electron impact excitation or sympathetic cooling of trapped ions. The latter being of particular interest for injected ion bunches which could have significant energies preventing efficient resistive cooling.

3.4 Detection circuits

ARTEMIS uses three tuned LC detection circuits as described in section 2.5:

- ARES-ST: Axial resonator for the spectroscopy trap $\nu_z \approx 600 - 800$kHz, connected to S2
- ARES-CT: Axial resonator for the creation trap, $\nu_z \approx 600$kHz, connected to C16
- CRES: Cyclotron resonator, connected to the spectroscopy trap, $\nu_+ \approx 35$MHz for argon and $\nu_+ \approx 42$MHz for bismuth, connected to half of S4.

There are several design considerations that must be made when building the resonator circuits. The implementation in ARTEMIS is covered in more detail in [66, 67, 105]. The major factors are its operation in cryogenic temperature, its natural resonance frequency,

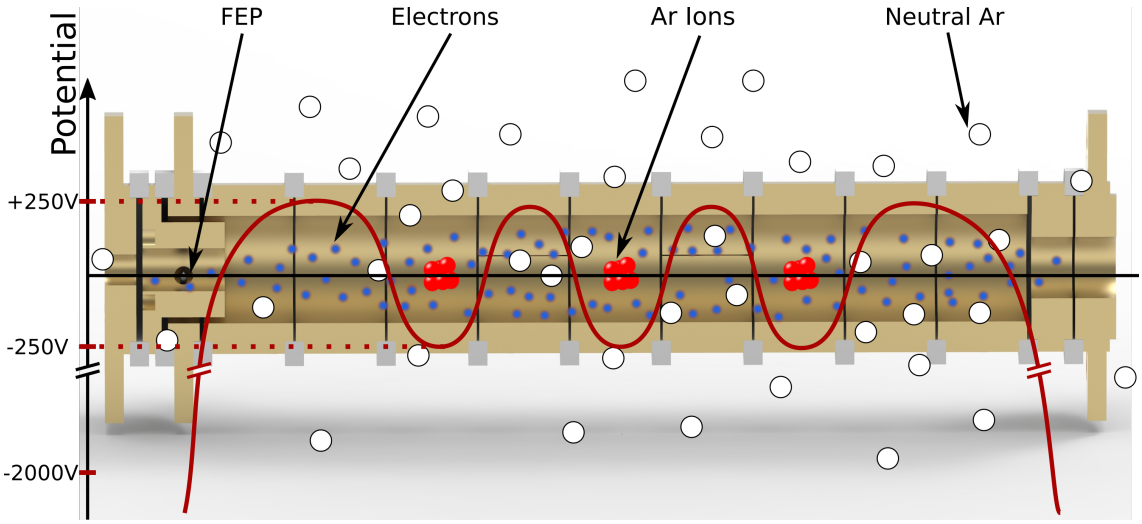

Figure 3.14: A schematic of the CT with its nested traps for ions and fast electrons. The approximate potential along the central axis of the trap is indicated by the red curve. Electrons emitted by the FEP (blue) are confined by the outer Penning-Malmberg trap and ionize neutral gas atoms (white) that are unaffected by the trapping fields. Some portion of the ionized gas atoms fall into the inner potential wells.

and its quality factor, Q. Building these resonators and pairing them to amplifiers is a somewhat precarious process and the resulting system is sensitive to a variety of environmental factors including temperature and humidity. Moreover, the resonance quality is limited by the lowest quality component in the signal chain as in equation 3.2, where the index i can be considered as each discrete component in the chain such as the trap, resonator, amplifiers, varactor, cables and connections.

$$Q_{det} = \left(\sum_i \frac{1}{Q_i} \right)^{-1} \tag{3.2}$$

Inside the cryogenic environment, they are usually stable for several months, but cycling the temperature during periods of maintenance often means the resonators will need to be replaced. Therefore several designs have been implemented in ARTEMIS over time. A typical resonator uses a copper solenoid coil wrapped around an air core supported by Teflon and encased in a copper housing. A typical implementation of this design for a cyclotron resonator is shown in figure 3.15.

Figure 3.16 shows the range of possible well depths that can be created in the CT and the corresponding axial frequency of some ions. Creating coils with resonant frequency below about 800 kHz required for the ST, generally calls for wire lengths of 50 to 100 meters, which means a significant amount of resistance for even copper wire at cryogenic temperatures. This ultimately limits copper coils to a quality of a few hundred when placed

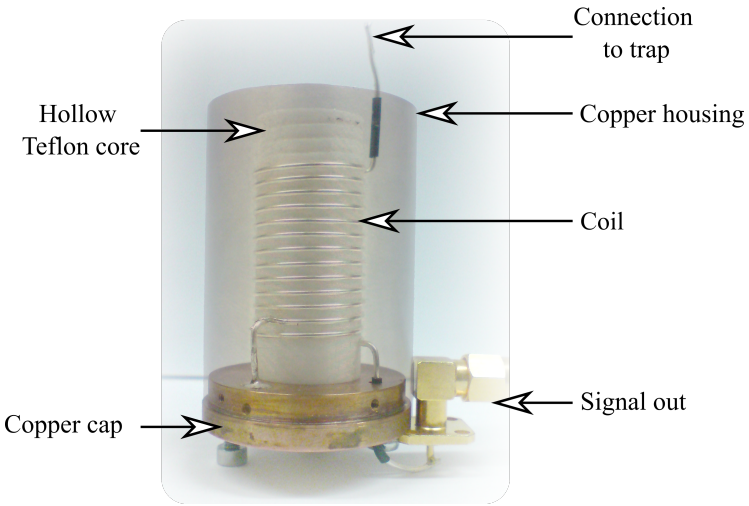

Figure 3.15: A typical cyclotron resonator used in ARTEMIS is shown. The copper housing has been made transparent for this image to show the inner details. A coil of wire is wound around a hollow Teflon core. The signal output is tapped about one third of the coil length before ground.

inside the magnetic field. Therefore it is desirable for precise detection and quick cooling of the ion, to use superconducting coils that enable qualities in the 10^5 range. Detecting the lowest q/m ions requires either large potential wells or resonators at very low frequencies which are impractical to produce at sufficient quality.

Unlike the axial frequency, the cyclotron frequency varies by only a small amount with the trap depth and creating a resonator exactly on the frequency of the ions is unreliable at best. Therefore, a small variable capacitance is wired in parallel to the cyclotron resonator. This allows the resonant frequency to be shifted by:

$$\frac{\Delta\omega_+}{\omega_+} = \frac{1-\sqrt{1-\frac{C_V}{C_R}}}{\sqrt{1+\frac{C_V}{C_R}}}, \tag{3.3}$$

where C_R and C_V are the capacitance of the resonator and variable capacitor respectively. This is implemented as a varactor tuning diode (MACOM MA46H202-1088) on a

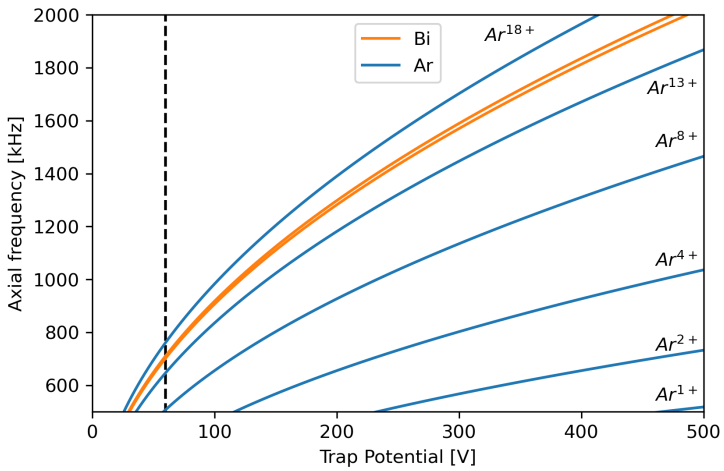

Figure 3.16: The range of applicable trap voltages in ARTEMIS and the expected axial frequency of some Ar charge states as well as Bi^{80+} and Bi^{82+}. The full range of the CT is shown on the x axis and the upper limit of the ST is indicated by the black line.

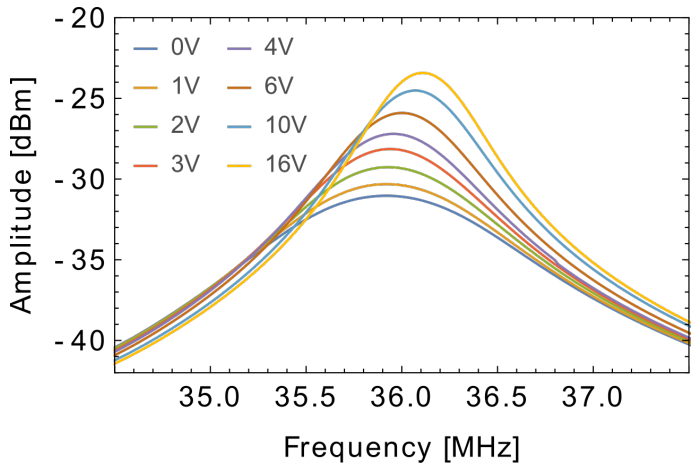

Figure 3.17: Variation of cyclotron resonator frequency and quality with varactor bias. Figure from [65].

custom filter/heater board by STAHL ELECTRONICS, which can be controlled by a low bias voltage so that it can used inside the cryogenic region. Figure 3.17 shows the variation of the cyclotron resonance as the varactor bias increased. Notably the quality increases significantly with higher voltages according to equation 3.4 as the capacitance is reduced. So precise prediction of the center frequency of the cyclotron resonator is still beneficial to put the ions on resonance with as high a varactor bias as possible. Here R is the resistance of the varactor and $C(U_{bias})$ is its capacitance as a function of the bias voltage.

$$Q_{var} = (\omega_+ RC(U_{bias}))^{-1} \tag{3.4}$$

With the resonator alone the signal from the ions would likely still be indistinguishable from the background noise of the electronics at room temperature. Two stages of amplification are used to prepare the signal for detection. The first stage is directly connected to the output of the resonator in the cryogenic region. This is critical because of the low Johnson noise in the cryogenic region. The cryoamplifiers are custom made at ARTEMIS and are individually paired with resonators to produce the best overall detection system possible. Figure 3.18 shows the circuit diagram used for producing the cryoamplifiers at ARTEMIS. A detailed description of the design principles and optimization can be found in [66, 105]. The general principle is a two stage design. The first stage has a high impedance and high voltage gain in the frequency range of interest, and the second stage has a gain just below one, but an output impedance of $50\ \Omega$ to limit reflections.

The choice of amplifier transistors for the cryoamplifier is crucial as many semiconductor substrates cannot operate in cryogenic conditions. The transistors are built on gallium arsenide semiconductors, which have some of the highest densities of free electrons at cryogenic temperatures and high electron mobility, which decreases their noise contribution. Often the most well behaved transistors at these temperatures are the result of

specific conditions of an individual batch which are not guaranteed in their manufacture. Therefore, these transistors should be considered vintage as obtaining replacements of equal quality is difficult.

From the cryogenic amplifiers the ion signal is routed out of the magnet bore and vacuum chamber by cryogenic coax cable. Room temperature amplification occurs on custom built boards from STAHL ELECTRONICS, the so-called room temperature filter boards. This signal is collected and analyzed in a Keysight N9000B spectrum analyzer.

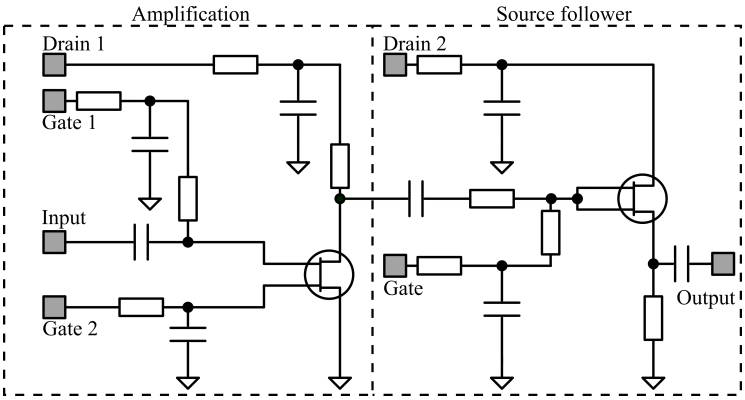

Figure 3.18: Circuit diagram of the cryogenic amplifiers used in ARTEMIS. The input pad is connected directly to the tap of the resonator coil. The drain and gate voltages are controlled by a low noise voltage supply from STAHL ELECTRONICS.

3.5 The Spectroscopy system

The spectroscopy system at ARTEMIS consists of the optical and microwave sources that are used for performing the double-resonance measurement (see section 2.3) as well as the connecting components for delivering radiation to the trapped ions. There are three main subsystems: the optical laser system, microwave system, and luminescence detection system. Figure 3.19 at the end of this section shows an abstract overview of the entire spectroscopy system as it currently exists for LMDR measurements in Ar^{13+} at 7 T.

3.5.1 Optical laser system

The current optical laser system at ARTEMIS as of the time of writing, is designed for the 2p fine-structure transition of Ar^{13+} at 441 nm. The system was first installed by A. Martin with subsequent development by P. Baus [106, 107]. It consists of four major components which are located in a environmentally stabilized room near the HITRAP tunnel:

- The spectroscopy laser is a DL 100 pro external cavity diode laser (ECDL) from TOPTICA. It can be tuned from 439.4 nm to 445.8 nm.

- The transfer cavity is an optical resonator cavity that stabilizes the frequency of the spectroscopy laser to the master laser. Fine tuning is achieved by precise control of the spacing of two concave mirrors.

- The master laser is a custom built ECDL by A. Martin and P. Baus. It has a precise frequency of 452.756 nm which is locked to a tellurium spectroscopy cell.

- The tellurium spectroscopy cell is a well known reference based on the so-called tellurium atlas. It provides a precise absolute frequency reference for the system.

The concept is that tellurium is vaporized by heating the cell to 504 K. Doppler-free spectroscopy is used to stabilize the master laser precisely based on feedback from the laser interaction inside the tellurium cell. This stable and precise laser is then used as a reference for tuning the transfer cavity. The spectroscopy laser is then shifted by an acousto-optic modulator and locked to the transfer cavity. Finally, the output from the frequency stabilized spectroscopy laser is referenced against the tellurium cell. This chain of reference frequencies generates a laser at the requisite 441 nm with high precision of the master laser.

The final output of the laser system is coupled into a long fiber that transfers the light from the laser lab to the ARTEMIS tower. A vacuum feedthrough is used to couple the fiber to another one inside the vacuum extension at the top of the magnet bore. The internal fiber extends to a mount directly above the window of the trap chamber by a narrow copper arm. At the end, the fiber is stripped of the protective jacket, and the emitted light is directed into the trap chamber through an aspheric lens, a quartz vacuum window and finally the ITO window.

The fluorescence light emitted by the ions is isotropic. The portion emitted in the direction of the window passes again through the ITO and quartz window and is collimated by the lens. It then passes around the fiber and mount and is focused by a second lens onto the image guide. The image guide is a bundle of thousands of optical fibers arranged in a 16 mm^2 lattice. At the end of the image guide the light is again collimated by a lens, passed through a vacuum window and a series of line filters centered at 441 nm, and finally focused on to the charge-coupled device (CCD) element of a camera. The camera is an ImagEM X2 from HAMAMATSU. This systems enables position sensitive imaging of the fluorescing ion cloud.

The design for the ultraviolet laser system that will be used for hyperfine spectroscopy in bismuth is currently underdevelopment. It should be noted that fibers in the UV range cannot be made with the low losses that are available in the optical range and must therefore be limited to short distances only. It is foreseen that the UV laser excitation will be

provided from the open end of the trap through the entire length of the vertical beamline. The fluorescence will be detected through the closed endcap and conversed into an electrical signal by a UV sensitive photocathode, rather than passed directly by an image guide.

3.5.2 Microwave system

The current microwave system installed in ARTEMIS is designed for the 65 GHz Zeeman transition in the lower fine structure state of Ar^{13+}. It was tested and installed by M. Wiesel and S. Ebrahimi [65, 66]. There are 6 major external components:

- The microwave source is a GT9000 synthesizer from GIGATRONICS. It is tunable from 2 to 20 GHz and uses a high quality YIG oscillator, which is important for precise measurement of the Zeeman transition.
- The clock for the microwave source is a 10 MHz rubidium frequency standard (SRS FS725) which ensures the long term stability of the synthesizer.
- The sensor is a model 578 locking microwave counter from EIP MICROWAVE, which monitors the output of the synthesizer and the clock to lock the synthesizer output.
- To match the requisite frequency range of the experiment a CFM1616X410-01 active frequency quadrupler is used, which can output frequencies from 64 to 66 GHz at up to 10 dBm.
- The amplifier is a model SP654-15-24-W from SPACEK. It has a gain of 19.8 dB and max output power of 23.2 dBm, but it not tunable.
- A model 520E attenuator from MIWAVE is used for tuning the power down from 0 to -25 dB relative to the input. This is necessary to minimize power broadening of the Zeeman transition, which would could limit the precision of the measured transition.

The microwave signal is then coupled to a coaxial cable to be sent into the vacuum chamber via a coaxial feedthrough. Inside the vacuum another coax cable, this time with low thermal conductivity, is used to route the signal into the radiation shield. This section has about 14 dB/m loss at 65 GHz, so its length is minimized. It is coupled to a 950 cm long OFHC copper waveguide directs the signal toward the trap. At the end is the microwave horn, which has a relatively high gain in the forward direction, effectively focusing the microwave radiation toward the trap center as pictured in figure 3.19.

This design results in the lowest possible losses along the entire length while still maintaining the low heat loads and vacuum conditions required for the experiment. The final expected power delivered to the trapped ions is up to 50 μW [65].

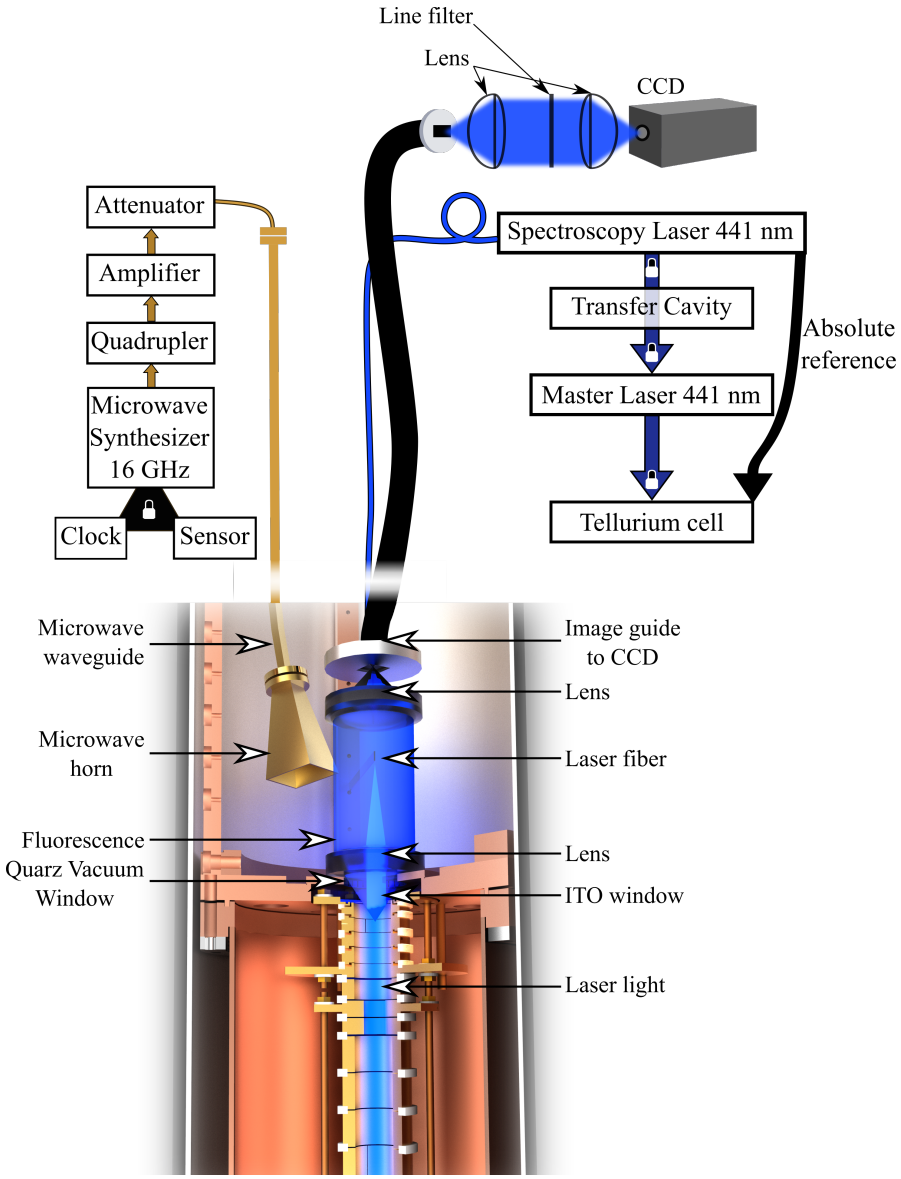

Figure 3.19: A brief overview of the spectroscopy system in ARTEMIS. The bottom half shows a schematic of the laser light overlapping the ions in the trap and the luminescence emitted by the ions collected by the image guide. The top half shows the components for generation and precise control of the laser and microwave irradiation as well as the light collection system. These are described further in the text.

Chapter 4

Design and Implementation of the ARTEMIS Vertical Beamline

Until recently ARTEMIS relied entirely on ions created by electron impact ionization directly within the CT. This chapter focuses on the vertical beamline which connects the experiment to the low-energy beamline of the HITRAP facility. Completion of the beamline represents the most recent major milestone of the experiment, which enables the injection of heavy HCIs from the accelerator facility of GSI.

The design of the vertical beamline was guided by the following requirements. It must...

- have an appropriate acceptance window for an incoming ion bunch from the low-energy beamline of HITRAP
- focus the ion bunch into the trapping region.
- provide some preliminary deceleration of the ions in flight.
- permit laser access for the UV spectroscopy laser.
- isolate the extreme vacuum and cryogenic temperatures of the trap chamber from the relatively poorer vacuum and higher temperature of the beamline.
- and of course it must not block the path of the ions in flight.

The final two points in particular provide the greatest challenge as any opening for the ions also allows residual gas to contaminate the vacuum. For this reason the concept of the fast-opening cryogenic valve was developed (see section 4.1). In addition the vertical beamline should...

- have a non-destructive beam monitoring device for tracking changes in the injected ion beam during the experiment
- have a means for compressing the ion bunch longitudinally.
- be able to be isolated from both the experiment and horizontal beamline without shutdown of either system

This chapter will provide a detailed description of the vertical beamline section and how it meets each of these challenges. Simulation data are also provided to justify the design elements of the various components. These simulations were performed primarily using finite-element numerical calculations for the electromagnetic field components and ion trajectories using COMSOL Multiphysics[1] and SIMION.

4.1 The Fast-opening Cryogenic Valve

The most critical component of the vertical beamline is the so-called fast-opening cryogenic valve (FCV). The FCV is responsible for isolating the ambient pressure and temperature conditions of the trap chamber from those of the rest of the beamline. Please be reminded of the considerations regarding background gas pressure and particle temperature which were discussed in sections 2.4.6 and 2.4.3 respectively. Previous particle traps have relied on the ability for fast, light particles to penetrate thin hermetically sealed windows or slow-opening valves for ion injection [108] that only need to be opened rarely. However, the HCIs of interest for ARTEMIS cannot penetrate even the thinnest seals at energies that permit capture. Other traps have used manually operable cryogenic valves, or electromagnetically actuated cryogenic valves with long opening/closing times on the order of minutes [109, 110]. In ARTEMIS however, the relatively short ion lifetimes and the necessity for frequent UV laser access (see sections 2.3.2 and 3.5) also preclude the possibility of manual opening during an experimental run and require opening times on the order of 100 milliseconds.

Below is a detailed description of the design and function of the FCV. The entire set-up is shown in figure 4.1. Relevant design parameters for the FCV are summarized in table 4.1.

The FCV design uses a copper shutter in the cryogenic environment to form a hermetic seal when covering the opening of the trap chamber. It is compressed flush against the face

[1] COMSOL is a finite element multiphysics simulation tool with an array integrated physics packages. The electrodynamics package was used primarily for this project for examining specific effects related to the design of ion optics components.

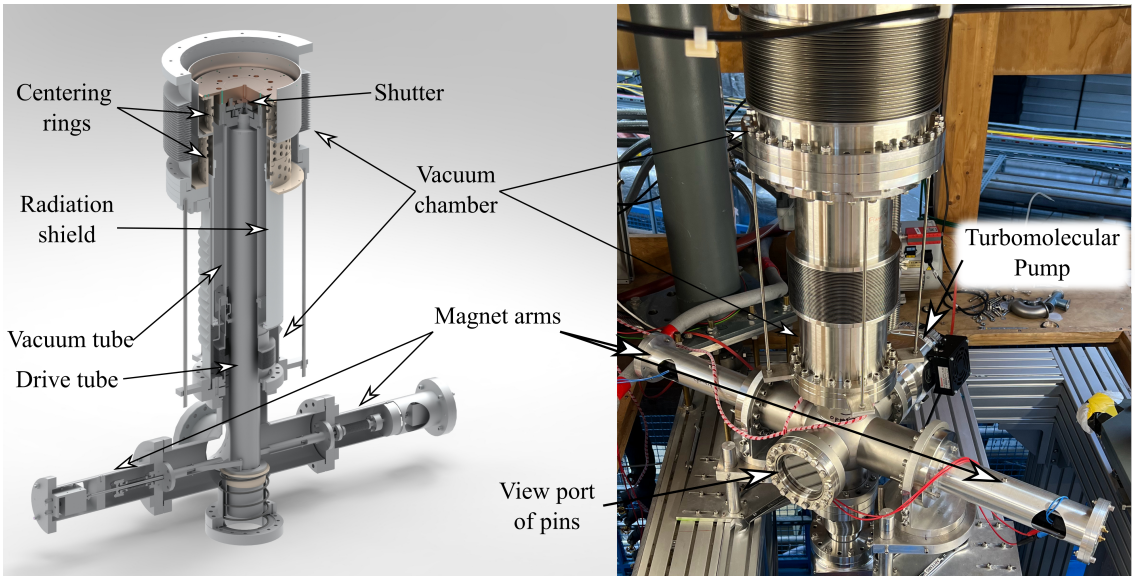

Figure 4.1: A cutaway rendering of the FCV and a photo as it is installed at ARTEMIS.

Table 4.1: Design parameters of the fast-opening cryogenic valve.

Parameter	Value
Temperatures	4 K (shutter) to 300K (vacuum chamber)
Pressures	$< 10^{-15}$ mbar (trap chamber) 10^{-10} mbar (beamline) 10^{-7} mbar (magnet bore)
Opening/closing time	<100 ms
Cycle time	90 s

of the trap chamber flange such that residual gas atoms have an overwhelming probability of sticking to the cryogenic copper surface, and all other connections are sealed with compressed indium wire. The shutter is then moved out of the beam path to allow injection. In order to achieve fast opening times on the order of milliseconds, mechanically actuated motion is used. The shutter is mounted to the *drive tube*, which is a thin stainless steel (1.4301) tube 710 mm in length with an inner diameter of 60.8 mm and thickness of 0.3 mm. It in turn is driven by arms connected to pins on the eccentric of the tube as shown in figure 4.2. These arms are a sufficient distance from the superconducting magnet that they can be driven with fast solenoids, (ITS-LS 4035 from Red Magnetics). The drive tube is mounted inside another thin stainless steel vacuum tube which separates the vacuum of the beamline from the vacuum of the magnet bore of ARTEMIS. This vacuum tube has an inner diameter of 85 mm, thickness 0.25 mm, and length 352 mm. These stainless steel tubes act as thermal isolators between the cryogenic region at the top and the room temperature region at the bottom. At the bottom of the vacuum tube, an edge-welded bellows

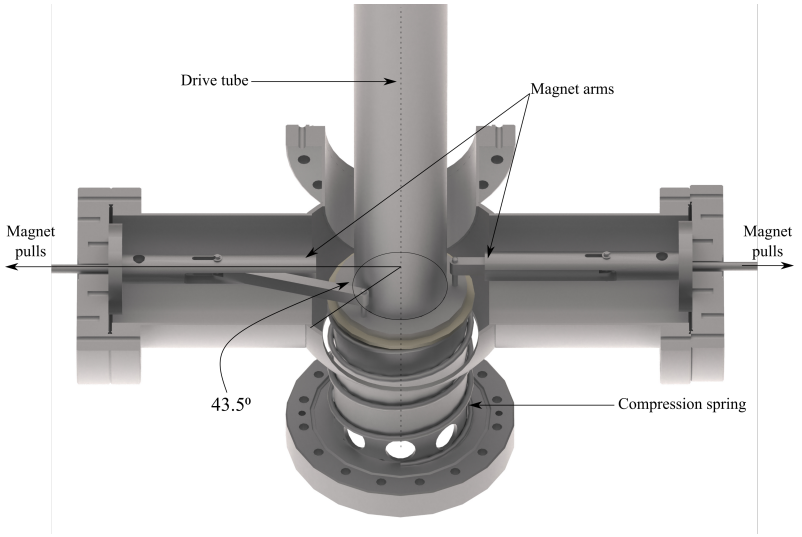

Figure 4.2: Diagram of the fast-opening cryogenic valve opening mechanism. Solenoid magnets pull on the magnet arms, which in turn apply a torque to rotate the drive tube. Note that in the final FCV assembly the pins that attach the arms to the drive tube are closer together than drawn here. The result is that they do not pull into a completely straight line with the arm mount. This lessens the loss of torque by the arm during rotation. The indicated 43.5° nominal drive rotation is maintained, in reality this arc sweeps a region somewhat displaced in the counter-clockwise direction.

allows some motion of these two tubes relative to the supporting cross below. As the shutter is mounted directly to the trap chamber, this allows the position of the trap chamber to be adjusted without moving the entire FCV. In addition, the walls of the bellows are extremely thin so it also insulates against the conduction of heat.

The shutter housing, and vacuum tube are all surrounded with a radiation shield which is coupled to the ARTEMIS radiation shield at the top by copper strands. Additional copper strands are connected between the bottom edge of the radiation shield and the bottom of vacuum tube as well as between the vacuum tube and the middle of the drive tube. MLI foil between each layer further reduces radiative heat transfer from the room temperature surfaces of the vacuum chamber and covers the small gap between the shields. The FCV also supports the trap chamber inside the magnet so as to decouple it from the vibrational motion of the cryocooler at the top. The weight is transferred to the vacuum chamber and mounting frame by two pairs of PEEK support rings. The rings are designed with conical and anti-conical groove pairs to ensure the concentric parts align when raised, which also centers the trap inside the magnet bore.

Finally all of these components are surrounded by a vacuum chamber in two sections. The top section is connected to the bore of the superconducting magnet and is primarily formed by two bellows. The top bellows mates to the bottom flange of the superconduct-

ing magnet and the bottom is a standard CF250 flange. A bellows is used in this section to allow access to the connection between the trap chamber and the FCV without deconstructing the entire assembly. Also for this purpose, an adapter plate of OFHC copper is installed between the bottom of the trap chamber and the top of the FCV. The bottom of this bellows sits on a zero-length CF250 to CF200 reducer flange. This flange forms the support plane for the PEEK rings that in turn support the trap chamber. Therefore, the precise position of the trap chamber can be adjusted by four threaded rods from below. The lower bellows section has a CF200 flange on top and CF160 on bottom. This bellows extends or contracts as the trap chamber is raised or lowered respectively.

The bottom vacuum section connects to the low-energy beamline and is formed by a 6-way cross. The top of this cross is connected to the bellows at the bottom of the vacuum tube. The arms are mounted to the sides of the cross and coupled to the drive tube inside. Two additional CF100 flanges are currently used for connecting a turbomolecular pump and a window to observe the motion of the drive tube as a diagnostic. Although neither of these are necessary in the long term.

An important consideration for the FCV design is the force and stroke length of the solenoids and magnet arms. They must provide enough torque to exceed the static friction at the shutter, which is the dominant component due to the sealing force of the compression spring. They must also quickly accelerate the rotation of the drive tube to meet the required opening time. The stroke length as well as the mounting angle of the arms must not limit the full rotation of the shutter. Instead a 5.5 mm slot is cut into the top of the FCV to guide the shutter motion and restrict it to a minimal path for uncovering the the aperture. Improper placement of the angle of the arms can inadvertently further restrict the motion in either direction. The nominal rotation angle is 43.5° to fully open the trap chamber aperture. The open and closed position of the shutter components are shown in figure 4.3. This demonstrates how the slot restricts the motion of the shutter.

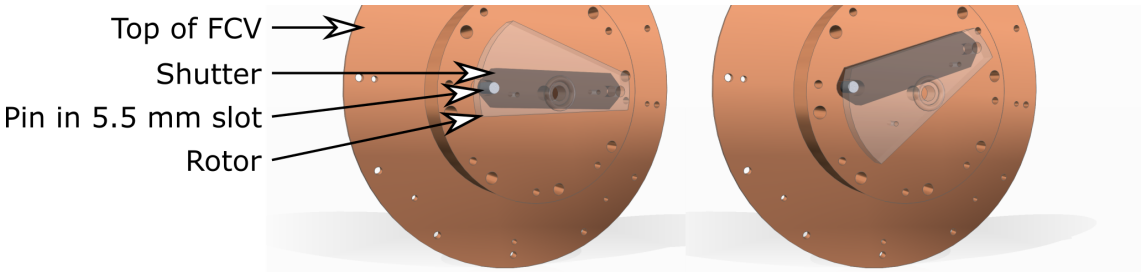

Figure 4.3: A CAD drawing of the shutter and the top piece of the FCV. The shutter and rotor have been made partially transparent to see the underlying motion. The rotor rotates with the drive tube which pulls on one side of the shutter. The other side cannot rotate about the beam axis. Instead it slides along a slot cut into the top of the FCV.

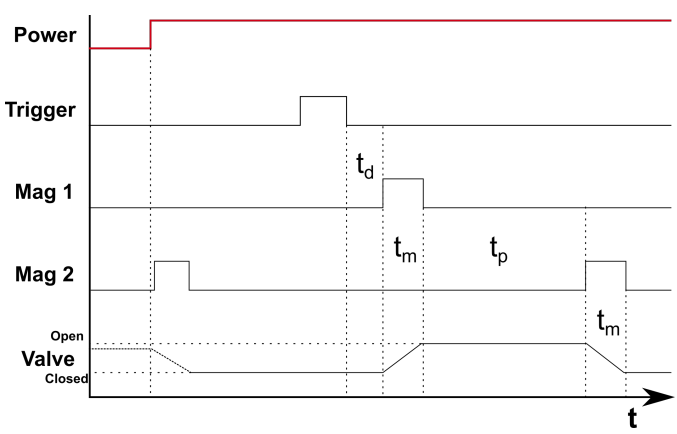

Figure 4.4: The timing signals for controlling the fast opening cryogenic valve. After the initial power on, magnet 2 triggers to ensure the valve is closed. Then on each incoming trigger the control box activates magnet 1 to open the valve followed by magnet 2 to close it. The timing between each magnet activation as well as the duration of the current pulses are programmable.

Transfer of the linear motion of the arms into the vacuum chamber requires linear motion vacuum feedthroughs. Typically such feedthroughs would use mechanical means to regulate the motion against compression by the pressure differential, but this would limit the intended operation of the arms. The FCV arms instead balance this compression against each other. As the vacuum is drawn the pressure pushes inward on both feedthroughs equally so that no net motion of the arms occurs. In this way the magnets are not counteracting the atmosphere pushing them inwards, which is much stronger than either magnet for the given size of the feedthroughs.

The opening and closing magnets are controlled by a custom designed control box. The control box contains two 1 mF capacitors for generating the large, low frequency current pulses for operating the valve. It controls the timing of the pulses relative to a TTL input signal. These are programmable with values from 1 millisecond to 1 second. Figure 4.4 shows the full control sequence of the FCV. After receiving power it generates a closing pulse to ensure the initial position of the shutter, then waits for a trigger signal. Once a trigger is received, there is a delay, t_d, before the current pulse to the opening magnet, t_m, a pause between magnet pulses, t_p, and a pulse to the closing magnet of the same duration as the opening pulse.

Although the opening time is programmable down to 1 ms, the actual opening time is limited. A camera with a frame resolution of 33 ms was used to monitor the shutter position while the FCV was installed directly below the ARETMIS magnet, but not mounted to the trap chamber. This allowed ambient light to be used for imaging the shutter position. Various t_m were applied with $t_p = 1$ s while the valve was cycled and monitored. For $t_m < 40$ ms no light could be detected through the shutter. While for $t_m > 50$ ms a completely open shutter was observed. Because there was no common trigger between the camera and the valve, precise determination of the actual opening time was not possible with this method. However a single frame with a partially open shutter could be recorded

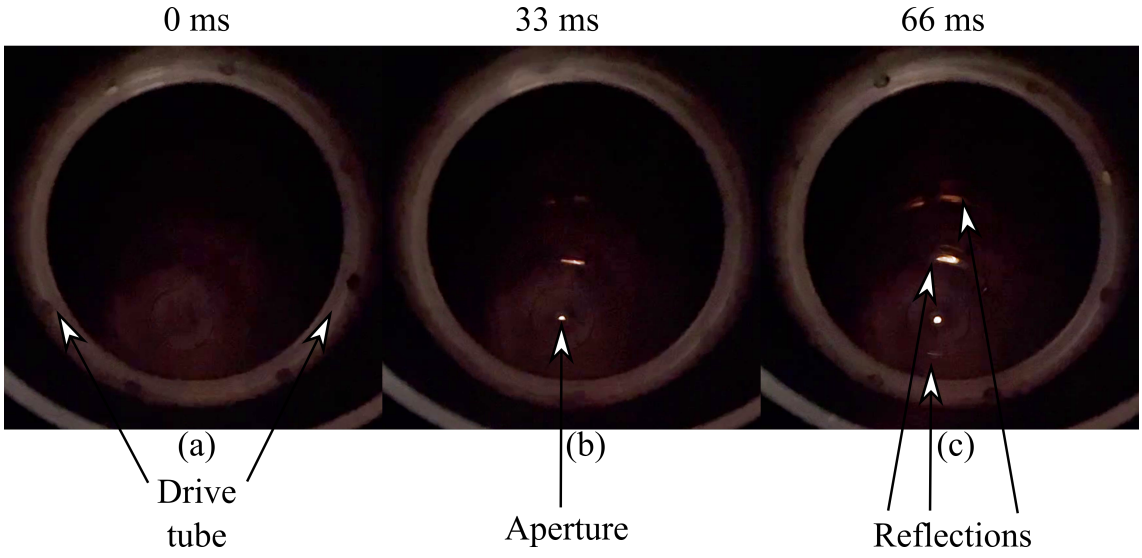

Figure 4.5: The view through the drive tube of the shutter of the FCV below the ARTEMIS magnet while decoupled to allow ambient light to enter. A sequence of three frames separated by 33 ms shows the (a) closed, (b) partially open, and (c) fully open positions of the shutter along with the timing of the frames. These images were taken with an applied $t_m = 50$ ms.

when $t_m > 50$ ms was applied as shown in figure 4.5. This puts an upper limit on the actual opening time of 66 ms assuming a reasonably low threshold of light detection is possible for an open shutter.

The observation that the shutter does not partially open for $t_m < 40$ ms is an indication that too little power is applied to drive the magnets in this case, resulting in no motion of the shutter during the magnet opening pulse. This is contrasted to the explanation that a sufficiently strong force is applied but for too short a duration to even partially open the shutter. Given that a partially open shutter was observed for $t_m = 50$ ms after a shorter elapsed time from the trigger of at most 33 ms, the duration of motion of the shutter is not a limiting factor for $t_m > 33$ ms. The observation that an applied $t_m = 40$ ms does not partially open the valve excludes the duration of motion as a limitation in this case, and only the lack of force remains. The limit is most likely caused by a high frequency shoulder on the output power spectrum of the control box. As faster pulses would transmit power in a higher frequency region of the spectrum, sufficiently fast pulses reduce the power delivered below the threshold to drive the device. However, this effect was not investigated further as even in the extreme case the valve is sufficiently fast for the design goal.

The Fast-opening Cryogenic Valve as a thermal bridge

There are two mechanisms by which the FCV increases the heat load of the experiment. The smaller effect comes from direct conduction of heat from the bottom of the magnet bore, which was previously well isolated with the old gas injection system. The second is the increased area and view factor for radiative heat transfer as the cold components now extend about 50% further down the length of the assembly than with the previous system. For a given geometry this can only be limited by the emissivity of the radiative surfaces, usually through MIL as described in 2.6

Careful consideration of the dimensions of the stainless steel isolation tubes has been used to control the conductive heat transfer. Figure 4.6 shows the expected temperature profiles along uniform lengths of stainless steel connected to a heat bath at each end of 4 K or 300 K accounting for the variable thermal conductivity with temperature. This is contrasted with profiles where the tubes have been connected to a 40 K heat bath halfway along their length. Profiles along the same path have the same heat load to the 4 K bath. This demonstrates the great reduction in length that can be achieved by intruding the copper strands between the tubes and the radiation shield. For example an uncoupled tube of 1.5 m delivers the same heat load to the 4 K bath as a coupled tube only 14 cm in length for the given cross sectional area. The trade off is that more heat is delivered to the 40 K stage of the cryocooler. Using the same example 4.8 Watts would be delivered to the 40 K stage by a 14 cm tube coupled to the 40 K stage at the midpoint. Figure 4.6 also shows the heat load delivered to each stage of the cryocooler for tubes of various lengths as well as different coupling locations as a fraction of the tube length measured from the 4 K side. The black lines are the conditions chosen for the drive tube of the FCV in ARTEMIS, which indicate a heat load to the 4 K stage of 45 mW and to the 40 K stage of 0.89 W. For comparison the heat delivered by the old stainless steel tube used for Ar gas injection is estimated to be about 8 mW.

The vacuum tube is half the length of the drive tube with a 17% larger cross sectional area, but it is connected directly to the 40 K stage at the bottom. It delivers an additional 53 mW to the 4 K stage. Estimating the heat flow through the bellows below the vacuum tube can be done similarly with some approximation of the geometry which limits the precision. However, the expected value is below 2 W depending on the exact thickness of the walls of the bellows. The PEEK support pieces have less than 4% of the thermal conductivity of the stainless steel, but as they are much shorter contribute similarly to the thermal loads of both stages. However, estimating their temperature profiles is more complex due to the geometry.

The conductive heat loads presented in this section were calculated for the cross sec-

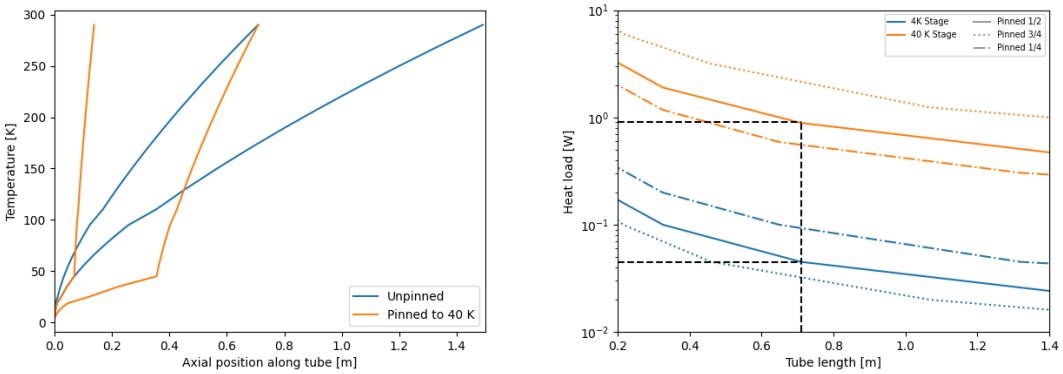

Figure 4.6: (Left) The temperature profile of a range of tube lengths is considered for connections at either end to thermal baths at 4 K and 300 K and contrasted to the scenario with an additional connection to 40 K at the midpoint. Overlapping paths indicate the same heat load to the 4 K bath. Pinning the tubes to 40 K at their midpoint significantly reduces the heat load or requisite length. (Right) The heat load delivered to each stage of the cryocooler through the isolating tubes of the FCV is considered for various lengths as well as pinning locations of the 40 K strands. The chosen length for the ARTEMIS FCV is indicated by the black lines.

tional areas of final design of the insulating tubes. While a thinner tube would reduce the heat load, these values permit a sufficient loading of pressure differentials to allow evacuation of each side of the valve. The chosen vacuum tube thickness can sustain a pressure differential up to about 0.3 bar before deforming. This vacuum pressure can be easily created with only mild pumping on one side. Therefore it is essential that both sides of the valve maintain a vacuum conductive connection at all times. In the molecular flow regime significant pressure differences have been observed between the magnet bore and the beamline (10^{-6} to 10^{-10} mbar at the extreme), but this gap closes rapidly as either side approaches a transitional flow regime and disappears completely in the continuous flow regime. Figure 4.7 shows the setup used for preventing catastrophic pressure differentials.

As of writing the valve has been used in two complete experimental runs and a third is pending. During the first run the motion of the shutter was prevented by over-compression of the spring below the drive tube, which caused too much friction when cooled. Given that the shutter could be moved before completely sealing the chamber, it is not clear if the shutter became stuck in a partially open state. The observed ion lifetimes indicate a poor vacuum pressure consistent with a continuous leak of residual gas into the trap chamber. Overcompensation for this effect in the second run left the trap chamber too low, and exposed a portion of the 4 K stage to radiation from the 300 K walls of the vacuum causing somewhat higher temperatures. Additional MLI was introduced after the second run to correct for this effect. Nonetheless, the principle motivation, to enable fast

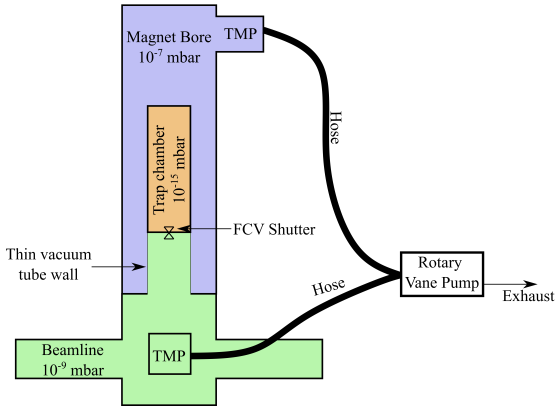

Figure 4.7: Vacuum pump scheme or the fast-opening cryogenic valve. If the pressure in either the magnet bore or the beamline increases significantly, the induced transition toward continuous flow will cause a corresponding increase in the other chamber. In the molecular flow regime the chambers are essentially completely independent.

Table 4.2: Performance of the FCV in each of the runs so far as measured by the lifetime of trapped ions of charge q, and the ultimate temperature of the trap chamber.

	Run 1	Run 2	Run 3
Trap temperature (K)	8.5 K	10.5 K	TBD
Ion lifetime (q=4+)	40 h	>500 h	TBD

repeated insertion of UV laser radiation, was achieved during the second run. The lifetime of the ion bunch was not limited by the chamber pressure even with repeated opening and closing of the valve, and the monolayer saturation time is estimated to be on the order of at least 10^5 cycles. The performance of the valve in each run is summarized in table 4.2. The third run is currently pending following the most recent changes, and results are expected in the near future.

4.2 Position-sensitive non-destructive single pass beam monitor

Due to the long drift length between the bottom of the FCV and the trap, steering the ion beam into the trap center will be challenging. The preliminary injection attempts are discussed in chapter 5. To facilitate injection a position-sensitive, non-destructive, single-pass beam monitor has been developed, but not yet implemented in the beamline. The beam monitor will allow the injection of ions to be monitored continuously without inter-

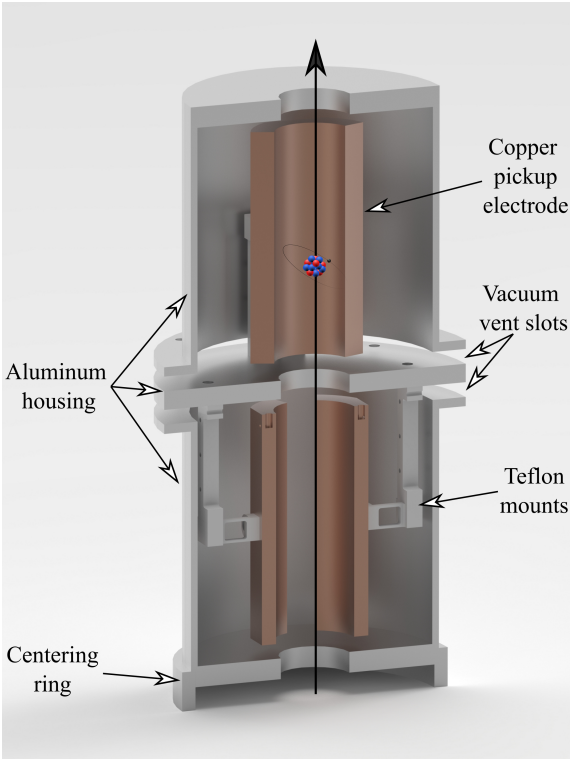

Figure 4.8: A drawing of the ARTEMIS position sensitive beam monitor, which is used to center the ions on the reference trajectory for injection into the trap chamber. The two pairs of electrodes are shown surrounded by the grounded housing and centering mount.

ruption of the experiment, and real time adjustments can be made to compensate for drift of the incoming ion beam over time. The detection principle is based on the same idea of induced image currents as is used for the detection of trapped ions, but in a single-pass pickup mode. As shown in equation 2.31, an ion near an electrode induces a current proportional to its velocity and the gradient of the electrodes geometry factor in the direction of the ion's motion. In order to determine the horizontal position of an ion beam relative to the reference trajectory, a pair of electrodes can be used to measure the induced current simultaneously in each electrode. The difference in signals between the two electrodes indicates the relative position of the center of charge between them. Two pairs positioned orthogonally can therefore be used to fully determine the transverse center of the ion beam. Such a configuration is shown in figure 4.8, which shows the design for the beam monitor in the ARTEMIS beamline.

From equation 2.31 it follows that the difference between the current induced in two electrodes by a moving charge is

$$\Delta I = q\nabla\Xi_1(\boldsymbol{r}) \cdot \frac{d\boldsymbol{r}}{dt} - q\nabla\Xi_2(\boldsymbol{r}) \cdot \frac{d\boldsymbol{r}}{dt} \tag{4.1}$$

$$= q\nabla(\Xi_1(\boldsymbol{r}) - \Xi_2(\boldsymbol{r})) \cdot \frac{d\boldsymbol{r}}{dt} \tag{4.2}$$

$$= q\nabla\Omega(\boldsymbol{r}) \cdot \frac{d\boldsymbol{r}}{dt}, \tag{4.3}$$

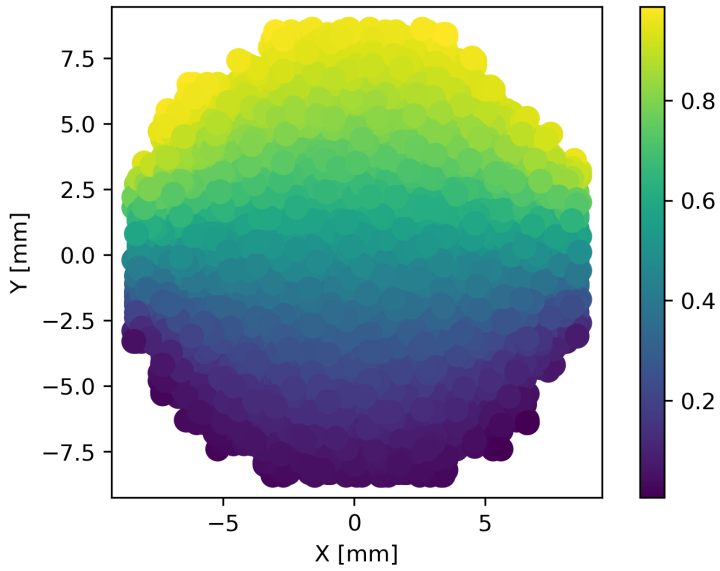

Figure 4.9: The geometry factor of a single electrode from the beam monitor simulated with SIMION. Here the data points sample the simulated function which causes the rough appearance of the function.

This motivates the definition of $\Omega \equiv \Xi_1 - \Xi_2$ which will be referred to as the position function. The precision of position detection is therefore limited by the derivative of the position function along the direction of measurement. Simulations of the geometry factor were used to optimize the dimensions of the pickup electrodes to maximize both the induced signal as well as the derivative at the center. The geometry factor of a single electrode is shown in figure 4.9. The four electrodes used in the detector all have the same geometry factor relative to their position.

The limit on the precision of the position measurement is the amount of noise charge within the detection electrodes. COMSOL was used to determine a capacitance of one electrode of about C=4.7 pF. At room temperature this induces a charge noise of

$$Q_n = \sqrt{k_B T C} = 867e, \tag{4.4}$$

where k_B is the Maxwell-Boltzmann constant and e is the fundamental charge. As it is not foreseen that the detectors will be used in a true differential detection mode, the effective noise in each is independent, and the noise in the difference signal is $\Delta Q_n = \sqrt{2} Q_n = 1.21\text{x}10^3\ e$. Taking the derivative of the position function at the center of the detection region in the direction of displacement, $\frac{d\Omega}{dx}(x=0) = 0.1\text{mm}^{-1}$ gives an estimated difference signal for a bunch of N ions at charge q, $\Delta Q = \text{qN}\Delta\Omega$ and a spacial resolution, R at a signal to noise ratio of one:

$$R(x=0) = \frac{\Delta Q_n}{\frac{d\Omega}{dx}(x=0)} \approx \frac{1.2\text{x}10^4\ \text{e} \cdot \text{mm}}{qN} \tag{4.5}$$

This indicates a spacial resolution well below the mm range for the center of charge of

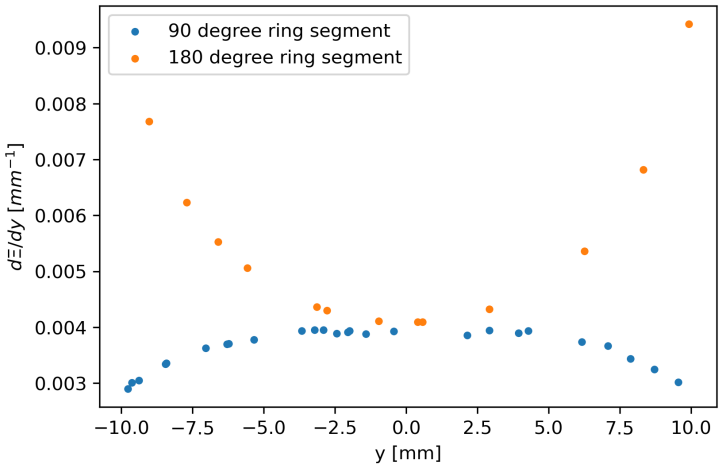

Figure 4.10: The derivative of the geometry factor for two electrode geometries is compared. The positive second derivative for the wider electrode indicates an improved spatial resolution for radially extended bunches.

10^4 Ar^{13+} ions as would be the case for bunches from the SPARC EBIT, and is well within the necessary resolution for injection. However, an important consideration is the radial distribution of charges. To first order the distribution doesn't limit the resolution, but nonlinearity of the derivative of the position function could reduce the spacial resolution for a significantly extended bunch size if the derivative falls off with distance. The spacial derivative is plotted for two geometries, a 90° ring segment and a near 180° ring segment in figure 4.10. For the larger segment the second derivative is positive which will improve the spacial resolution of radially extended bunches. The real beam monitor electrodes are constructed with 140° angles to try to maximize this effect without inducing significant mutual capacitance between electrodes.

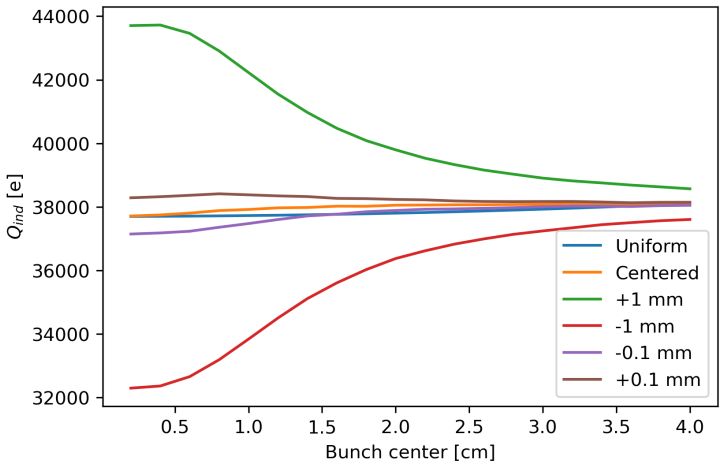

Figure 4.11: The results of simulations of 10^4 Ar^{13+} ions inducing charge in the electrodes as they pass through detector are shown. Here the total induced charge is shown as a function of the longitudinal position of the center of charge for a uniform bunch centered on the beam axis as well as for several Gaussian beams offset from the beam center both toward and away from the detector.

The induced charge of a bunch of 10^4 Ar^{13+} ions was simulated as it passed through the monitor. This was done for uniform and Gaussian beam profiles at 5 mm diameter and for varying position of the beam center. Figure 4.11 compares the results from these simulations. It can be seen that as expected the beam profile has only a small effect on the induced signal as the center of charge doesn't change. In fact this deviation is about the same scale as the elements size in the simulation so could be a stochastic artifact of the simulation. Near the detector center, the difference in the induced signal is only a few thousand charges for separations on the order of 0.1 mm which confirms the determination of the spacial resolution determined above. It should be noted that in these simulations a shorter electrode length of 1 cm was used so only about a quarter of the total charge was induced in the detector. This motivated the extension of the electrodes up to about 5 cm such that almost half of the total charge is induced on the reference trajectory, although not for the entire bunch length simultaneously.

Ion bunches from the SPARC EBIT are about $1\ \mu s$ long, which for Ar^{13+} at 4 keV/q beam energy is over 500 mm long, by the time they reach the vertical beamline. Simulation work of the dynamic time-domain signal for such long bunches is still ongoing, but this can still be used to determine the appropriate bandwidth for charge sensitive amplification of the signal so that it can be detected. The chosen amplifier is a CR-110-R2.1 from Cremat which has a low equivalent charge noise enabling the sub mm resolution discussed above and a gain of 1.4 V/pC which gives a signal of a few mV for bunches of about 10^4 ions. Although the saturation effects for large bunches about 10^6 ions could make position monitoring not possible in those cases.

4.3 Deceleration and Focusing Sections

The middle section of the beamline is designed to allow the horizontal beamline as well ARTEMIS to be mutually independent, such that either is still operable when the other is offline. To that end it has a vacuum bellows and gate valve at each end. These valves can sustain about nine decades of pressure difference between the vacuum chamber and atmosphere in one direction, and are oriented such that the ARTEMIS beamline can be vented without affecting either ARTEMIS itself or the low-energy beamline. They are controlled by a 24 V programmable power supply to allow interlocking with the pressure gauges in each section. In between is a diagnostic chamber, similar to those on the horizontal low-energy beamline, and the deceleration and focusing section for injection into ARTEMIS. Figure 4.12a shows a CAD drawing of the components in this section of the beamline. Figure 4.12b shows the graphical output of a SIMION simulation used for

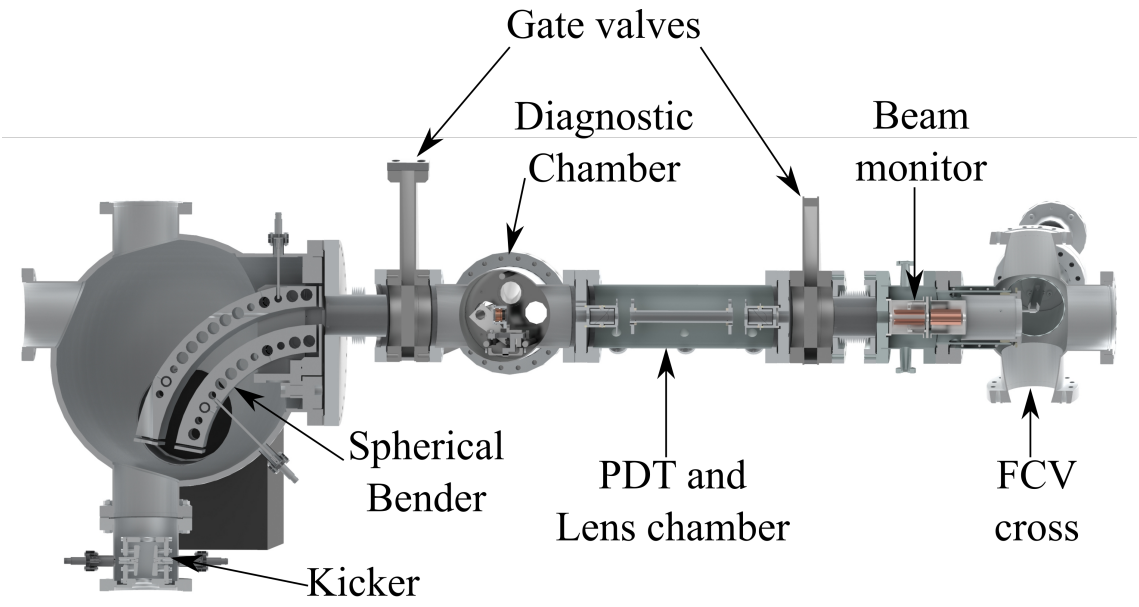

(a)

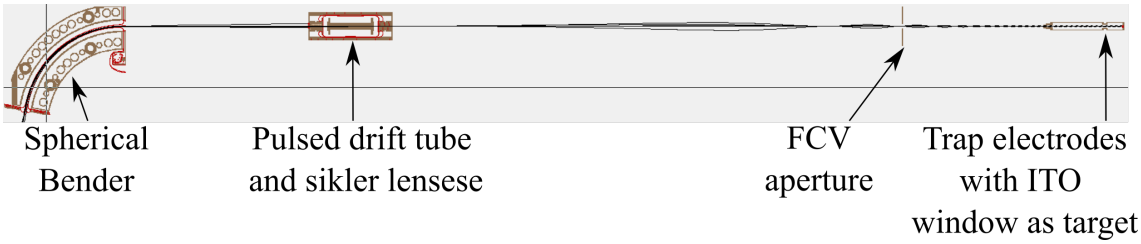

(b)

Figure 4.12: (a) A CAD drawing of the ARTEMIS vertical beamline between the Kicker-bender and the FCV. Note that the drawing is rotated such that ions enter upward through the kicker and fly toward the FCV at right as pictured. (b) SIMION simulation of injection of 4 keV/q ion bunch through the vertical beamline. The major electrostatic components or physical apertures are shown with the exception of the kicker and beam monitor. The ion trajectories are the curvy black lines.

tuning the injection potentials for delivering ions all the way to the ITO window inside the ARTEMIS trap chamber. The simulation and CAD program were used iteratively to refine the designs of the components and optimize them for the highest transmission of ions within the available parameters. More results from the simulations will be presented in the corresponding sections below. The deceleration and focusing chamber consists of a pulsed drift tube (PDT) flanked by Sikler lenses.

4.3.1 Pulsed Drift Tube

The PDT removes energy from the ions while the lenses focus the beam into and out of the section. Figure 4.13 shows the principle of operation of the PDT, where the ions

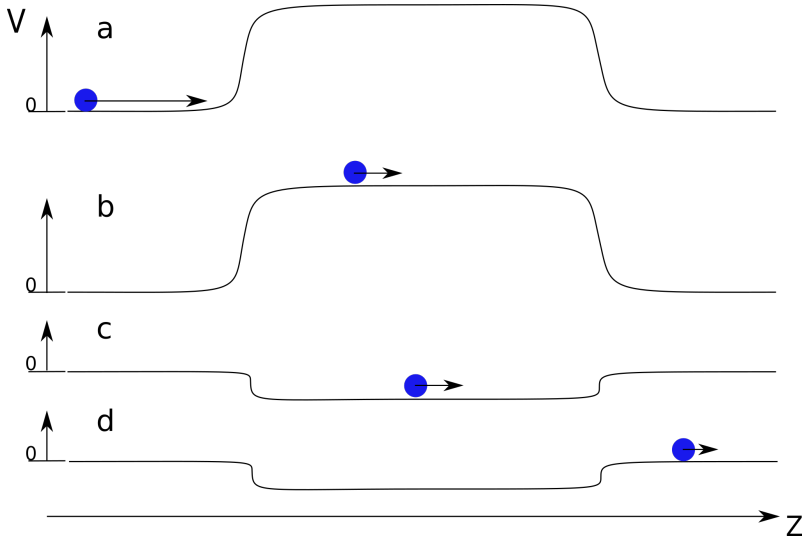

Figure 4.13: The operational principle of the pulsed drift tube is depicted in four stages from a to d. (a) Ions enter the region of the PDT with high kinetic energy. (b) The ions have expended some kinetic energy to climb the potential hill. (c) The tube is pulsed near to ground potential while the ions are inside and the potential energy of the system is dissipated by the electronics. (d) Finally the ions eject the tube with reduced total energy.

are decelerated by the electrostatic repulsion of the tube, and then ejected after the tube is pulsed near to ground. This results in a net transfer of energy from the ions into the capacitor banks of the switching electronics. The potential gradient at each end reduces the effective length of the PDT because the region of near uniform potential decreases.

In order to limit the number of connections needed inside the ARTEMIS trap chamber, especially those with potentially large currents which carry heat, it is desirable to place the PDT in the beamline instead. However, this increases the challenge of injection as the deceleration significantly increases the emittance of the ion beam. The radial confinement of the trap's magnetic field can be used to guide the slow ions into the trap over relatively large distances as long as they enter near parallel to the field lines (see section 2.7.5). SIMION was used to compare the ions transmission through the PDT with and without magnetic confinement. Figure 4.14 shows the graphical output of the simulation for a selected run highlighting the major physical processes that affect transmission.

Figure 4.15 shows the results of the results of the simulation for a converging ion bunch with relatively large initial emittance ($\epsilon = 5$ mm $\cdot$ mrad) and drift energy of 5 keV/q. Here it is apparent that the transmission depends on the relative deceleration as expected, and that the added confinement of the magnetic field improves transmission but not essential to the successful operation of the PDT. The deceleration section is currently located in a region of low magnetic field of only a few Gauss.

The ARTEMIS PDT has an effective length at 90% field strength of 167.8 mm. No-

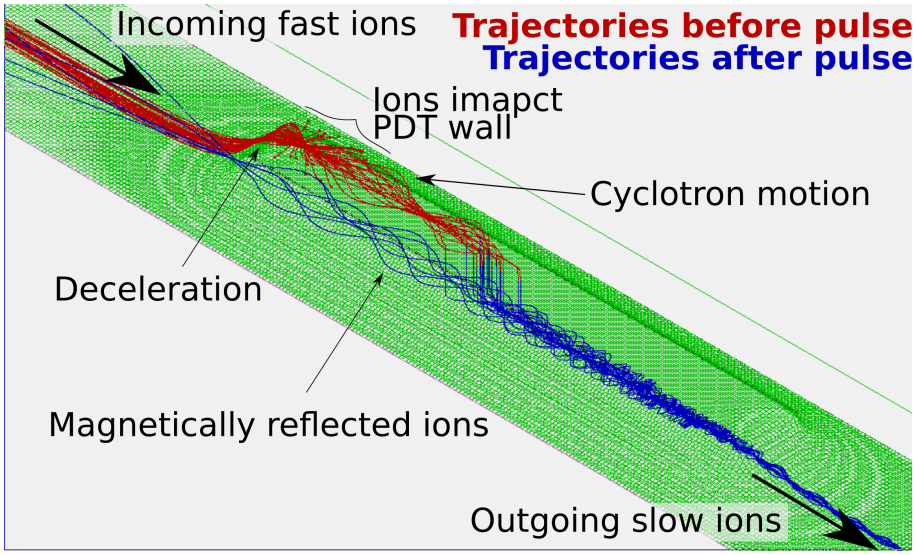

Figure 4.14: Graphical output of the SIMION simulation for the ARTEMIS pulsed drift tube. The incoming ions before the pulse are depicted by the red trajectories and the outgoing ions afterward are in blue. The height of the green surface depicts the electrostatic potential in a two dimensional slice of the simulation environment. The incoming ions from the upper left are lensed and slowed by the potential. Many are confined by the magnetic field before impacting the PDT walls. After pulsing they drop down to the lower potential surface which is near flat. Several are reflected off of the magnetic field gradient and pass backward through the PDT after pulsing. The transmitted ions exit the simulation to the lower right.

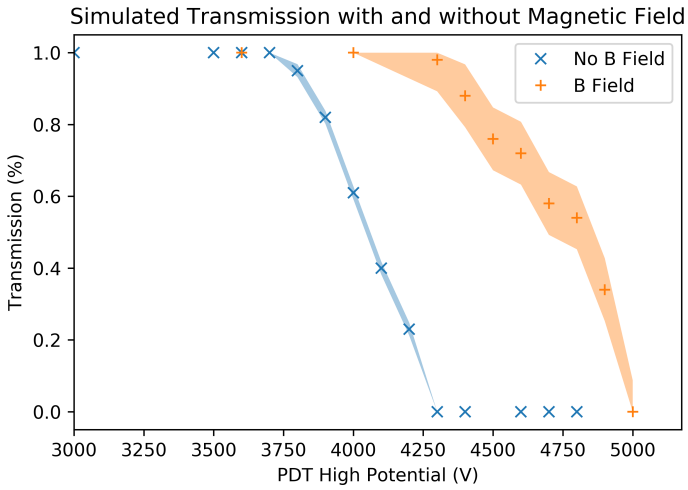

Figure 4.15: A comparison of select results from the SIMION simulation of the pulsed drift tube. Here the transmission is compared for a range of deceleration potentials with and without the magnetic field. The shaded regions indicate the statistical uncertainty of the transmission over 10 runs.

tably the bunch length from the EBIT at drift potential in this section is about 500 mm. However, this decreases with the square root of the deceleration potential such that the entire bunch fits inside the effective length at 89% deceleration for a 4keV/q beam of Ar^{13+} ions. While this is a plausible value, in practicality some of the bunch will likely be lost due to this length limitation. The finite space of the beamline made it impractical

to lengthen the PDT.

The capacitance of the PDT was also determined by simulations of the components inside the deceleration and focusing section. It is estimated to be 11.4 pF. The fast pulse of the PDT potential is driven by a GHTS 60A high voltage push-pull switch from BEHLKE. For a low capacitance load such as the PDT, the switch can perform a voltage switch (10 to 90 %) of up to 6 kV in 12 ns drawing an expected average current in this use case of 3.3 A, well below the design rating of the switch at 15 A. The HV wires for the PDT inside the vacuum chamber are thicker to support the associated heat load, although the current pulse is so short only minimal heating is expected even with relatively short breeding times in the DREBIT, which correspondingly increase the cycle frequency of the PDT. In addition, the switch can switch between positive and negative polarities relative to ground. This allows the deceleration to occur while climbing both an incoming and outgoing potential hill as is shown in steps c and d of figure 4.13. The main benefit of this effect is it limits the probability of breakdown of the dielectric that isolates the PDT from its mounting hardware, by allowing a two step deceleration. It can also be used for small adjustments to the focusing which may useful if the decelerating potential in unipolar mode is too high for the incoming beam such that transmission through the PDT would be unacceptably low. This competes with the longitudinal compression for increasing transmission and the final values should be tuned to the specific incoming beam.

After deceleration the expected spacial longitudinal distribution will be reduced as discussed above, but this has no effect on the longitudinal straggling which will cause the beam to spread out again after deceleration. To correct for this effect and further improve transmission into the trap, the PDT design will be separated into two pieces with elongated interlocking crown shaped serrations as shown in the left of figure 4.16. This geometry creates a linear potential hill along the length of the PDT as shown in the right. Higher energy ions enter ahead of the bunch center and climb further up the hill whereas the opposite is true for slower ions. When both ends of the PDT are pulsed down to near ground simultaneously, an energy dependent deceleration occurs.

This new design has a lower effective length of only 118 mm and the combined capacitance of both pieces increases to 12.6 pF. This is consistent with expectations as the overall size of the PDT doesn't change but the positions of the nearby grounds for mounting do slightly. The effective cross sectional area decreases due to breaking the azimuthal symmetry. Figure 4.17 shows the cross section of the electrostatic potential in the midplane of the tube perpendicular to the ion trajectory. Here the azimuthal dependence of the potential smooths out further from the walls of the tube as expected. The effect is quantified as shown in the right side of the figure. The variation of the field shape along

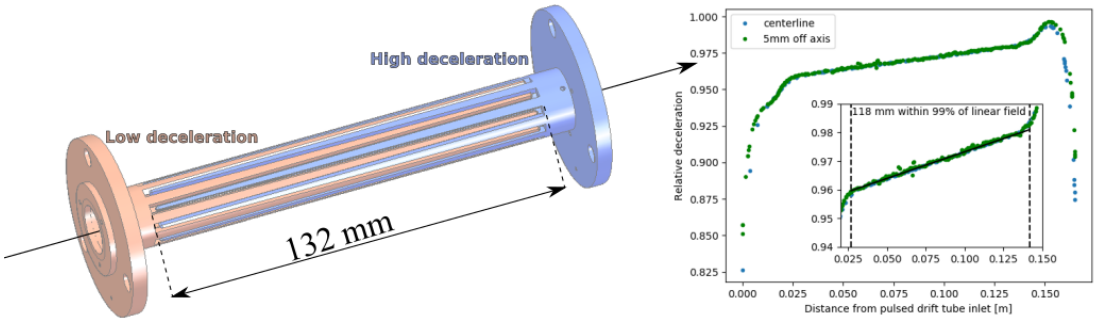

Figure 4.16: (Left) A CAD drawing of the serrated pulsed drift tube design. The ion reference trajectory is shown by the black arrow. The two halves of the PDT are biased above and below the average deceleration potential for high and low deceleration respectively. (Right) The centerline potential and a parallel potential are simulated for the serrated PDT. The inset shows the nominal usable length of the PDT where the field is linear. Ions within a 10 mm diameter spot size experience the same deceleration, but the deviations on either end contribute a small spherical aberration.

circles of increasing radii is shown. For $r > 0.6R$ the variation is about 1% of the average field, where R is the inner tube radius. The expected field distribution is a square wave near the tube walls and a sine function off center, deviations here are artifacts due to the limited memory available for simulation. An attempt is made to smooth the artifacts in analysis with the smoothing accounting for much less than 0.05R in the final value.

As the capacitance is so low, one possible improvement would be to increase the tube radius and decrease the number of tines. This would improve the ease of initial steering through the PDT and could also increase the effective area. However, as explained in chapter 5 the isolated PDT makes a good target for picking up the ion signal as they fly though. Increasing the tube radius could reduce this effect. Due to manufacturing difficulties the serrated version of the PDT could not be implemented during this work. It is expected to be installed in the ARTEMIS beamline soon.

4.3.2 Sikler lenses

The two Sikler lenses are modified forms of the lens presented in [111]. The Sikler lens is similar to a traditional einzel lens as described in section 2.7, with the center electrode cut by two planes angled 45° to the beam axis and 90° from each other, which creates 4 independent electrodes. Each section of the lens, when biased alone, steers the ion beam in a direction defined by the sum of the normal vectors of the two cutting planes for that electrode projected onto the xy plane. An example of this steering is shown in figure 4.18. This particular configuration of cutting planes significantly reduces aberration of the focal point caused by breaking the azimuthal symmetry and allows for small corrections

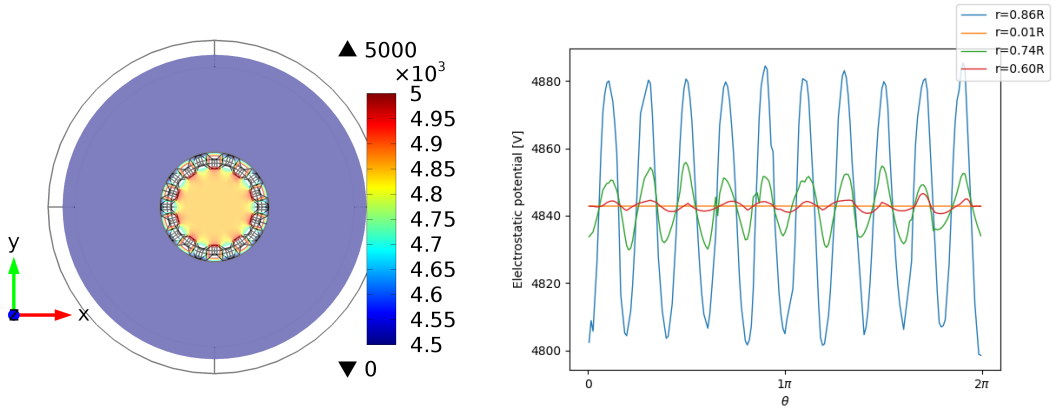

Figure 4.17: (Left) A slice of field distribution inside the serrated pulsed drift tube at the center plane perpendicular to the ion trajectory. The effective diameter where the field has azimuthal symmetry is only about 5 mm. (Right) The method for quantifying this area considers the azimuthal variation of the field potential along circles of increasing radii, r, as a fraction of the inner tube radius, R.

to the steering of the ion beam. This is especially important for focusing into the trap where the drift region is over 1 m long and the cyclotron motion significantly amplifies the effect of any misalignment. In addition, the lens can correct for astigmatism of the ion beam by purposefully adding a small quadrupole component to the focusing field, but this is limited to beams elongated along one of the steering axes of the lens, therefore the two lenses are oriented with a relative 45° rotation about the beam axis. Thus the 8 electrodes that comprise the two lenses are uniquely identified and labeled by the direction of deflection for similar polarity charges and bias potential. The final applied biases are determined as shown in equation 4.6. Here the voltages on the left are applied to the named electrode, and the voltages on the right are tuned for the desired effect: f for focusing, x or y for steering in the respective direction, and a for astigmatism correction, with numbers indicating at which lens the effect is applied. Note that astigmatism correction in the X and Y directions are only possible with V_{a1} and corrections in the planes 45° from X and Y with V_{a2}. As defined here positive values for V_{a1} compress the X dimension and stretch the Y, and positive values for V_{a2} compress the +X+Y dimension and stretch the +X-Y.

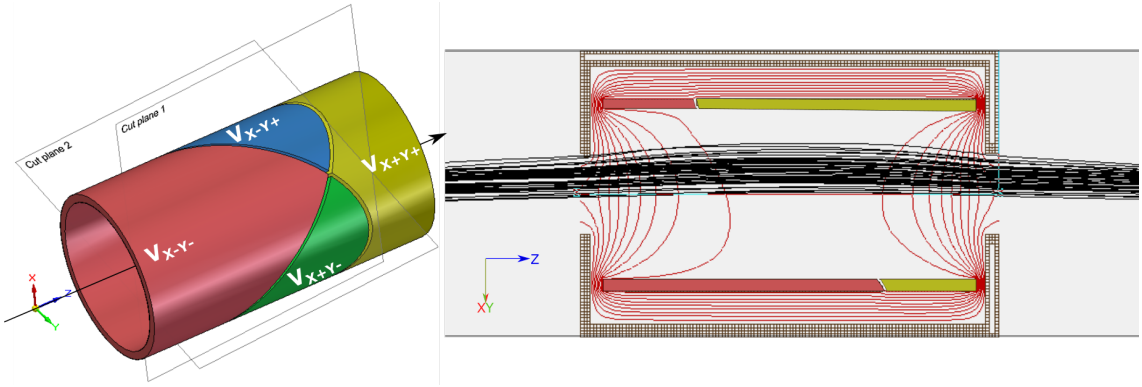

Figure 4.18: (Left) CAD drawing of the concept of the Sikler lens. The sections are colored to highlight their shape and labeled by the direction into which they steer ions with matched charge to their own polarity. Also indicated are the planes of the diagonal cuts. (Right) The graphical output of a SIMION simulation of the Sikler lens steering and focusing an ion bunch. Here the steering plane is angled to both the X and Y planes. The electrodes have matching color to the left. Only two electrodes are visible in this slice. Grounds are represented by the brown hash pattern. The red lines are equipotential lines and the black are ion trajectories. The incoming bunch parameters and steering are exaggerated relative to the device size for demonstrative purposes.

$$\begin{pmatrix} V_{X+} \\ V_{Y+} \\ V_{X-} \\ V_{Y-} \\ V_{X+Y+} \\ V_{X+Y-} \\ V_{X-Y+} \\ V_{X-Y-} \end{pmatrix} = \begin{pmatrix} 1 & 1 & 0 & 1 & 0 & 0 & 0 & 0 \\ 1 & 0 & 1 & -1 & 0 & 0 & 0 & 0 \\ 1 & -1 & 0 & 1 & 0 & 0 & 0 & 0 \\ 1 & 0 & -1 & -1 & 0 & 0 & 0 & 0 \\ 0 & 0 & 0 & 0 & 1 & 1 & 1 & 1 \\ 0 & 0 & 0 & 0 & 1 & 1 & -1 & -1 \\ 0 & 0 & 0 & 0 & 1 & -1 & 1 & 1 \\ 0 & 0 & 0 & 0 & 1 & -1 & -1 & -1 \end{pmatrix} \begin{pmatrix} V_{f1} \\ V_{x1} \\ V_{y1} \\ V_{a1} \\ V_{f2} \\ V_{x2} \\ V_{y2} \\ V_{a2} \end{pmatrix} \tag{4.6}$$

In ARTEMIS these lenses focus the beam from the kicker-bender into the PDT and the output of the PDT into the trap chamber. As the middle section of the beamline has bellows on either side, small deviations between the center axis of its beampipes and the reference trajectory of the ions is anticipated. This steering and focusing is achieved in a compact device that can be accommodated in the limited space of the vertical beamline. When compared to the quadrupole doublet steering in the horizontal beamline, the Sikler lenses are only about 15% as long, saving valuable length along on the beam axis, which ultimately made the addition of the gate valves and beam monitor possible.

The performance of the lenses for steering into the trap was evaluated by simulating several scenarios of incoming ions into the lenses. The results of two scenarios are shown

Table 4.3: The parameters for determining the angular acceptance for injection into ARTEMIS. The most stringent limit currently comes from the aperture of the CT.

Magnetic mirror	CT aperture
Distance, lens to peak field: 1743 mm	Distance, lens to CT: 1560
Field at lens: 8.3 G	Aperture diameter: 5 mm
Angular acceptance: 34.4 mrad	Angular acceptance: 1.6 mrad

in figure 4.19 as the 2D emittance before and after the lens. The gray shaded regions indicate the angular acceptances of both the magnetic mirror (dark gray) and the most stringent aperture by angle (light gray) which entrance to the CT. The parameters for for these values are given in table 4.3

In the first scenario the beam is off axis and steered into the lens by another prior optical element. The beam coming into the lens in this case is well controlled and only a minor correction rights the outgoing beam. In terms of the emittance, this is indicated by shifting the center of the ion distribution to the origin. In the second scenario a wide beam with a fan-like profile is focused into a converging beam as well as steered into alignment with the reference trajectory. The beam profile causes several ions to fly near the lens electrodes. These are essentially scattered by the strong field in this region and appear in the emittance as filaments in the upper right and lower left quadrants. The second scenario represents a more realistic beam as was observed during the first injection tests. Although improvement of the beam conditions coming into the lens is likely still possible, this demonstrates that in principle the lenses could account for even a relatively uncontrolled incoming beam. In both cases 500 ions were simulated. They were focused with about 70% of the beam potential, and steered with up to 2%.

As previously stated the drift region from the second Sikler to the trap chamber is over 1 m in length and the magnetic field requires the ions enter as near parallel to the field axis as possible, so proper operation of the focusing and steering is crucial to the injection of ions into ARTEMIS. Introduction of the beam monitor and proper selection of aperture sizes will help to ensure the beam is both centered and true. However, great care must be taken to ensure all apertures are themselves parallel to the field axis and aligned. Therefore it is foreseen that a laser will be directed through the complete beamline to mark the reference axis to aid alignment of middle section of the beamline with target masks. This should allow millimeter precision for the alignment of all apertures.

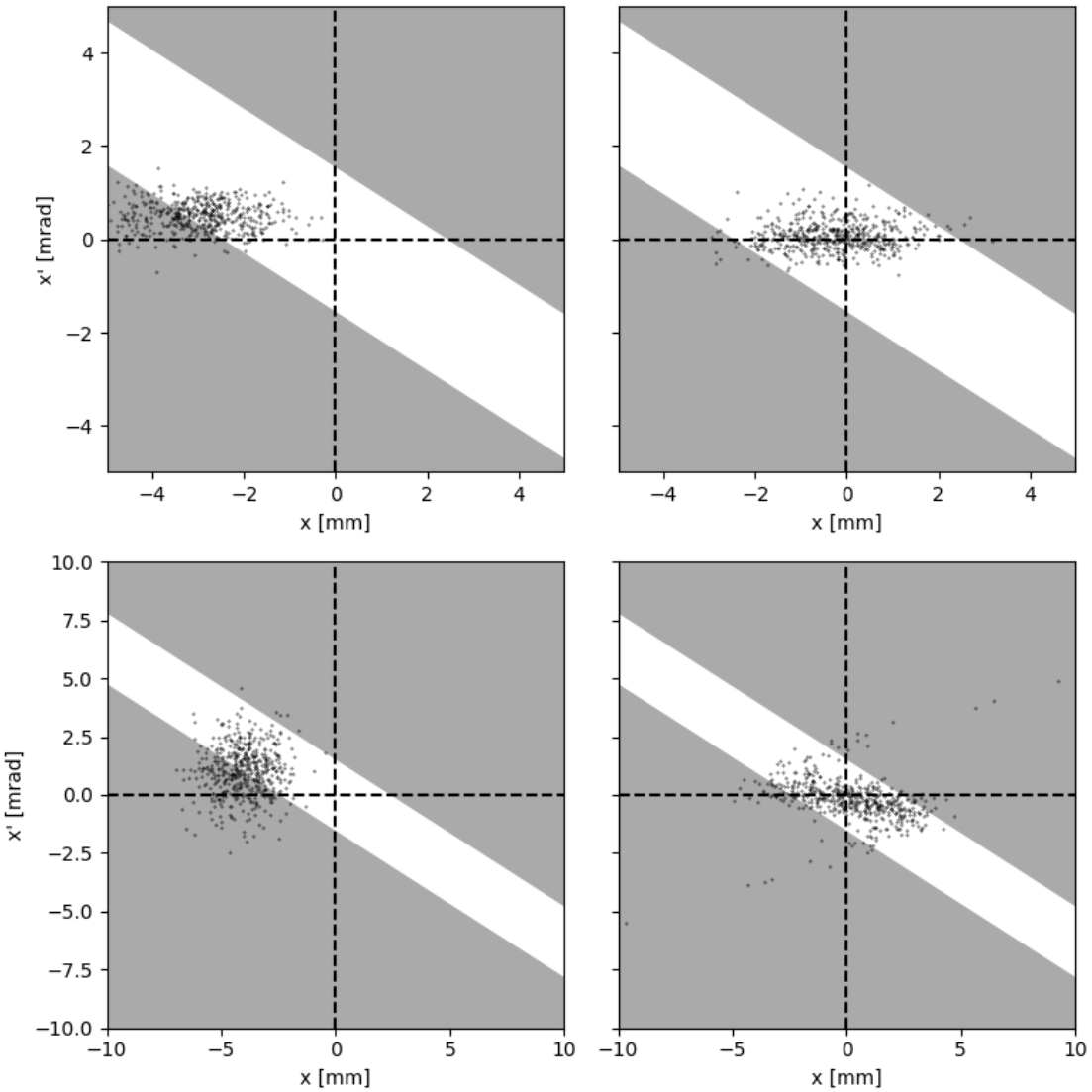

Figure 4.19: The 2D emittance for an ion beam in shown for two scenarios before and after correction with the Sikler lens. The shaded regions indicate the angular acceptance of the magnetic mirror (dark) and the aperture of the CT (light) (Top left) a parallel beam is entering the lens off center and at an angle. (Top right) the beam exits in parallel with the reference trajectory and on axis. (Bottom left) a widely diverging and broad beam is incoming off axis and with an average angle not parallel to the reference. (Bottom right) the beam exits slightly converging onto the reference axis and centered. Some filamentation of the emittance occurs as result of ions scattered by the lens.

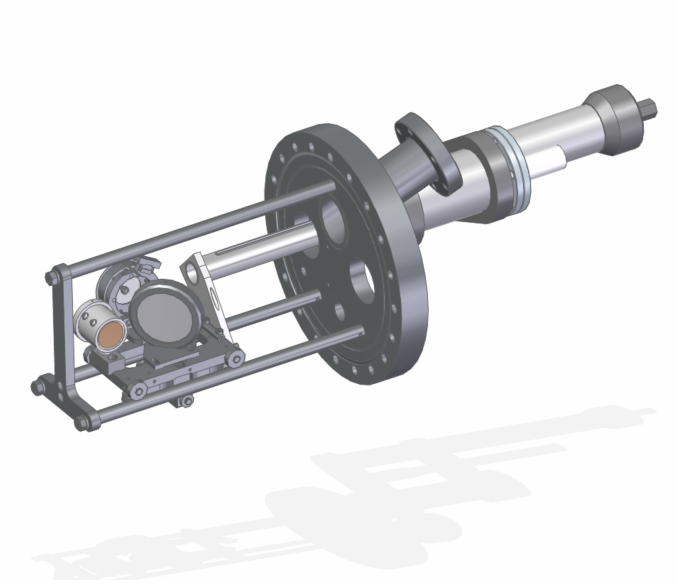

Figure 4.20: A CAD drawing of the inner components of the diagnostic chamber. This shows a detailed view of the sled that moves the detectors inside the chamber. The Faraday cup is on the left and the MCP with the mirror are the right. The sled is pushed or pulled along the rails by a rod that extends into the linear motion vacuum feedthrough.

4.4 Diagnostic Chamber

The diagnostic chamber (often abbreviated DK *Ger: Diagnostische Kammer*) of the vertical beamline is the same design as the others on the horizontal beamline with some details given already in [96]. They monitor the conditions of the beam and vacuum at regular intervals as well as provide convenient access for pumping the beamline vacuum with turbomolecular pumps. Each one also has a permanent ion getter pump (AGILNET Vaclon Plus 300) as well as a wide range pressure gauge (various). The getter pump maintains the vacuum after the turbomolecular pump is removed and the pressure gauge can measure vacuum to 10^{-9} mbar using a combination Pirani and inverted magnetron gauge.

The main feature of the diagnostic chamber is the sled for mounting beam monitoring components. There are generally two kinds of beam diagnostics that are used in the beamline: compensated Faraday cups [112] and microchannel plates (MCP) [113] with phosphor screens. The Faraday cups provide direct measurements of the beam current with high temporal resolution, and are a reliable target for tuning. The MCPs offer more detailed information about the beam size, shape, and position when viewed by a sensitive CCD camera. A mirror mounted behind the phosphor screen reflects the image through a window in the feedthrough flange and to the camera. Figure 4.20 shows the sled that mounts inside the diagnostic chamber. The sled can be moved into or out of the path of the beam by a linear motion vacuum feedthrough. The feedthrough is graduated so that the detectors can be placed precisely on the beam path. The diagnostic chamber of ARTEMIS currently has only a Faraday cup mounted, but space is available for additional diagnostics if needed in the future.

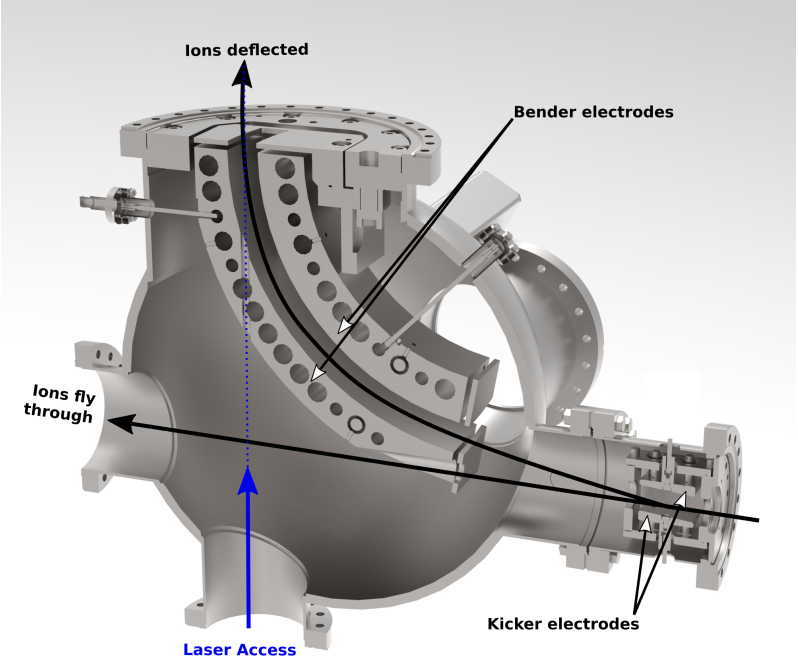

Figure 4.21: A CAD drawing of the kicker-bender below the ARTEMIS beamline. The ions can be deflected into the vertical beamline or fly directly through undisturbed. Laser access is provided by a small aperture in one electrode of the bender and continues all the way to the ARTEMIS trap chamber, through the vertical beamline and FCV.

4.5 Kicker-Bender

The Kicker-Bender is responsible for deflecting the reference path of the ion bunch into the vertical direction on axis with the ARTEMIS magnet. This is accomplished by a 10° 'kick' where the ions are deflected over a short range, followed by a smooth bend over the remaining 80° in a circular arc. The advantage of this configuration is that the 80° bender does not block the beam path when the potentials are grounded. In this way the kicker-bender can selectively bend the ion beam or allow it to fly through unimpeded. Both the kicker and bender have two electrodes with apertures at the entrance and exit. Figure 4.21 is a CAD drawing of the kicker bender indicating the possible paths for ions.

The spherical bending elements have curvatures of 235 and 265 mm for the inner and outer surfaces respectively, giving a bending radius of 250 mm and effective length of about 349 mm. Simulations of ion injection with SIMION showed the expected beam waist only about 30 cm from the exit of the bender, which sets the required location of the focusing section within 60 cm from the bender exit. As explained in 2.7 the bender can

cause significant longitudinal separation of the beam for ions entering at an angle to the reference trajectory or with significant energy differences. Therefore, more accurate steering into the bender could help to reduce the measured bunch lengths in future injections. The first order transfer matrix for the bender is

$$R_{ij} = \begin{pmatrix} 0.174 & 0.246\ \frac{\text{mm}}{\text{mrad}} & 0 & 0 & 0 & 0 \\ 3.94\ \frac{\text{mrad}}{\text{mm}} & 0.174 & 0 & 0 & 0 & 0 \\ 0 & 0 & 0.174 & 0.246\ \frac{\text{mm}}{\text{mrad}} & 0 & 826\ \text{mm} \\ 0 & 0 & 3.94\ \frac{\text{mrad}}{\text{mm}} & 0.174 & 0 & 3.94\ \text{rad} \\ 0 & 0 & 0.985 & 0.206\ \frac{\text{mm}}{\text{mrad}} & 1 & 636\ \text{mm} \\ 0 & 0 & 0 & 0 & 0 & 1 \end{pmatrix}. \tag{4.7}$$

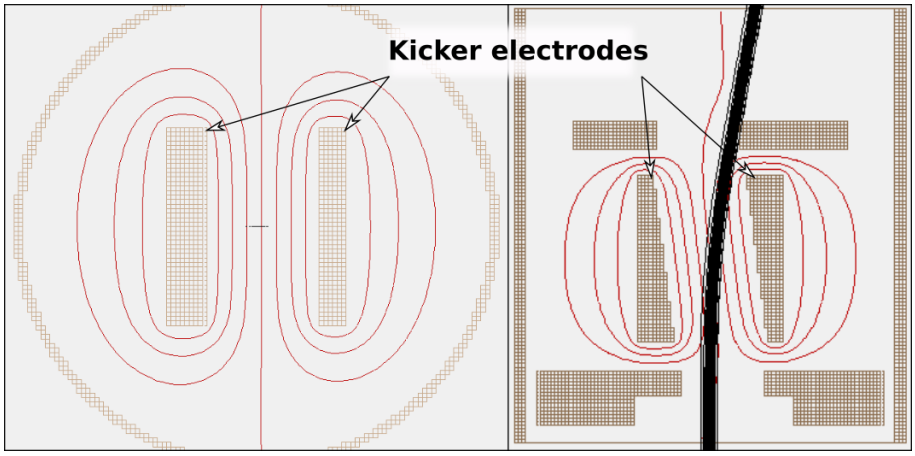

Figure 4.22: The graphical output of the SIMION simulation of the 10° kicker. Ion trajectories are distributed only in the bending plane in this image and appear as black lines. Red lines are contours of the potential generated by the labeled electrodes. All other brown hashes are grounded. (Left) is a slice of the transverse plane showing almost no field gradient in the unbent direction. (Right) is a slice in the bending plane.

The effects of the kicker are not well understood in terms of transfer matrices. As the equipotential lines are near parallel in the plane perpendicular to the ion deflection, it was found to act as a drift region in this dimension. The simulation of these equipotential lines are shown in figure 4.22. Over the short path into the bender the kicker showed no significant impact on the profile of the beam.

Chapter 5

Investigation with Highly Charged Ions in ARTEMIS

The new connection to the HITRAP low-energy beamline will enable injection of heavy, HCIs for future measurements in ARTEMIS. It is a significant step toward the complete commissioning of the experiment and its design goals. For g-factor measurements, an ensemble of some 10^5 ions will need to be stored in the trap for a few hours. They will also need to be cooled into a dense ion cloud for the best results with the spectroscopy system.

Following completion of the beamline, the conditions of the experiment are verified again using ions created in the CT. In addition, the first injection of ions from the SPARC EBIT on the HITRAP low-energy beamline is being prepared. This chapter reports on the current conditions of the experiment following the connection to HITRAP. This includes a residual gas pressure better than $2.37\text{x}10^{-14}$ mbar, with cooling into a liquid-like state possible for dense ions clouds created from cryosorbed gas atoms. The next steps for the experiment following this work will be to finalize the parameters of injection based on the models used for its design and fully implement capture and active cooling of injected ions. Some specific suggestions for future work are given throughout.

5.1 Ion creation

Ion creation in ARTEMIS without the old cryovalve for argon injection, is still possible using residual air or cryosorbed particles. Even in the excellent vacuum pressures made possible by the fast-opening cryogenic valve the residual molecular density of the gas phase is still above 1000 ions per cubic centimeter. This could allow for simpler creation of small ion clouds compared to previous use of the cryovalve where the pressure spike

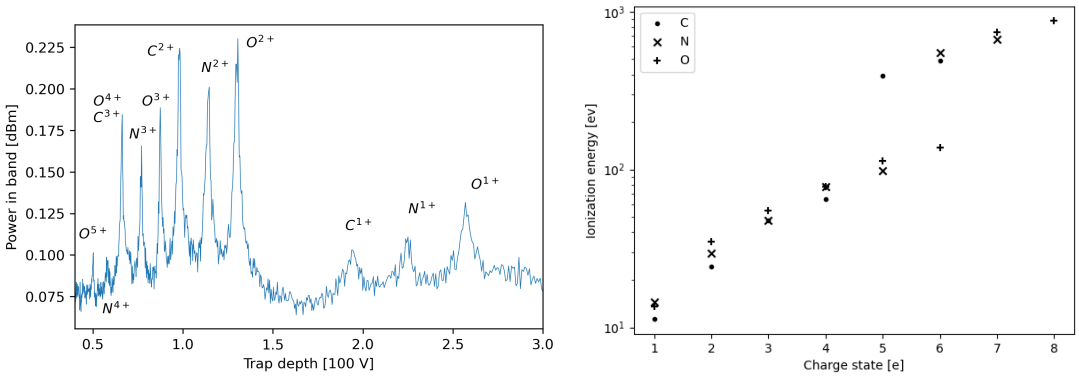

(a) (b)

Figure 5.1: [Ion creation with the fast-opening cryogenic valve.](a) The charge to mass spectrum measured from a trapped cloud of ionized residual air. (b) The ionization energies for the components of air that can be seen in the spectra of ARTEMIS.

from gas injection meant that even cold creations tended to have a large number of ions. It comes at the cost of significantly reduced probability of creating argon ions from the residual gas since Ar is such a small component of air. Although evidence of argon ions was seen with residual air creation, its relative population is too small compared to oxygen, nitrogen and carbon to make measurements practical.

The method of ion creation is covered in section 3.3.2, and a detailed study of the creation parameters is done in [65]. Ion creation from air requires no gas pulse from the old cryovalve, and the required accelerator voltage to achieve a given current from the FEP has increased. Otherwise the process is largely unchanged. The main factor that is adjusted is the breeding time, which determines the duration of the electron beam. Longer breeding times produce a larger proportion of higher charge states, but also more ions overall and at higher initial energies. For investigating specific effects of the ions' motions often smaller number of ions are more useful because the distribution of the induced signal is usually narrower and cooling takes less time.

The pressure estimation with the FCV presented in this work was only able to set an upper limit, which opens the possibility that ion creation from gas phase residual air is not feasible in large numbers if the pressure is significantly below this limit. Another possible explanation is that electron currents from the field emission point sputter cryosorbed atoms from the inner trap surfaces. Given that FEP currents are on the order of nA, the Brillouin limit of the outer Penning-Malmberg trap in the CT would be reached nearly instantly with electrons. Therefore those electrons could be scattered onto the cold surfaces with sufficient energy to break the weak intermolecular bonds responsible for cryosorption.

No evidence was found as of yet to determine which of these proposed mechanisms is the dominant mode of ion creation in the current setup, but the significant presence of ionized components of air should not be considered a measure of the residual air pressure as both creation mechanisms are possible.

The charge to mass spectra collected clearly indicate the constituent components of air when looking at chains of charge states as shown in figure 5.1a. The trap voltage at which these species come into resonance matches the value predicted by equation 2.20 to within a few volts, much smaller than the relative spacing of those species. This is further reinforced by the observation that reducing the FEP voltage causes higher charge states to vanish from the measured spectrum in the same order as decreasing ionization energies of those systems. Figure 5.1b shows the ionization energy of each charge state for the main atomic components of air except for bare hydrogen.

5.2 Ion Injection

The first attempts at injection of ions into ARTEMIS are still ongoing. Preliminary results indicate the critical role of steering into the magnetic field and aperture of the FCV. Although ions have been successfully detected in the steering section they have not yet been detected in the trap chamber. A grounding issue within the downstream Sikler lens prevented the necessary steering to find the ITO window target during the second run of the FCV.

Ions were created in the SPARC EBIT using argon gas with a breeding time between 1 and 80 ms and an electron current of about 20 mA. This generates ion bunches of 10^4 to 10^5 ions with charge states from 16+ down to about 8+ depending on the breeding time. A preliminary set of bunches was recorded in the ARTEMIS Faraday cup using a DHPCA-100 variable gain high speed current amplifier from FEMTO with a gain of 10^6 and a TDS2002B oscilloscope from TEKTRONIX

Both long and short breeding times in the EBIT were used to produce the signals in figure 5.2a. The Faraday cup used no compensation voltage in these measurements so the ion counts are around 30% higher than measured. With only rudimentary tuning of the components of the beamline, around $2\text{x}10^4$ total ions across all charge states are represented. The lines are not true fits to the data but roughly outline the individual charge states. The expected distributions are normal in energy which leads to the rightward skewing in time. As the breeding time is reduced the average charge state shifts down, above 80 ms the resulting bunch is entirely Ar^{16+}.

The beamline elements were then tuned to optimize the current on the Faraday cup.

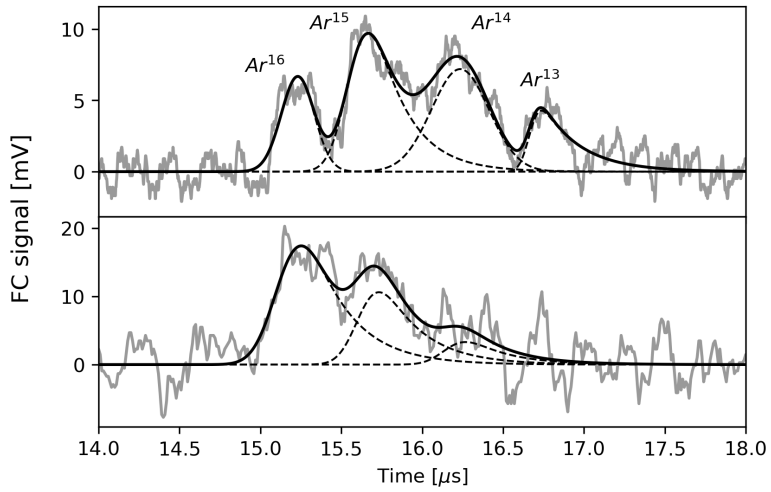

(a)

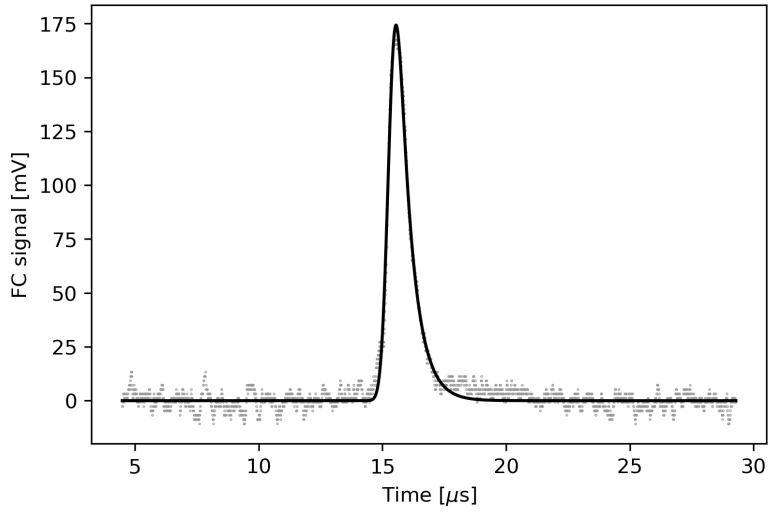

(b)

Figure 5.2: Ion bunch signals in the ARTEMIS Faraday cup. The top of (a) shows the soft spectrum with a short breeding time and multiple charge states. Whereas the bottom has a long breeding time and only 16+ and 15+ are readily visible. Both have a total ion count across all charge states of about $2\text{x}10^4$. (b) is the signal after tuning with about 10^5 Ar^{16+} ions.

The optimal parameters are given in Appendix A . Figure 5.2b shows the resulting time of flight signal of almost pure Ar^{16+}. The beam energy used for first injection tests was 4 keV, and although it wasn't directly measured, the horizontal and vertical emittance are estimated to be between 5 and 10π mm·mrad based on prior experience with the beamline.

As of writing, the furthest along the beamline that an ion signal could be detected was by using some of the electrodes of the downstream Sikler lens as a charge counter, but the quality of the signal measured this way is low. Instead, figure 5.3 shows the induced ion signal that can be detected as the ion bunches fly through the PDT without deceleration. The measured signal approximately matches the expected signal for an ion bunch of 1 µs width passing through the PDT which is shown by the black line. The measurement is broadened by the limited bandwidth of the amplifier, while the simulated signal experi-

ences no broadening. Steering into this section is reliable, as the same parameters could be reapplied in multiple subsequent days and the ion signal would reappear with nearly the same intensity without adjustment. Sweeping the steering with either the upstream Sikler lens or even the spherical bender results in the following sequence of detection on the PDT: ions completely blocked by the lens aperture (no signal), ions strike the PDT (unipolar pulse), ions pass through the PDT (bipolar pulse, figure 5.3), ions strike the other side of the PDT (unipolar signal), ions blocked by the aperture (no signal). Therefore it is reasonable to expect that steering with the downstream Sikler could have been used to direct the beam into the trap aperture had it been available.

From the measured signals on the Faraday cup and PDT, a significant loss of ions was found with transmission around only 10%. This is consistent with the SIMION simulation which showed steering into aperture of the Sikler lenses to be difficult for some beam conditions in the low-energy beamline. These apertures are the same 5 mm diameter as in the CT. In this way the combined apertures act as beam collimator that ensures ions exiting both Sikler lenses are parallel with the beam axis to a very high degree. For higher transmission a more detailed study of the beam profile before the lenses would be needed, especially after the bender, where currently no MCP is installed for this purpose.

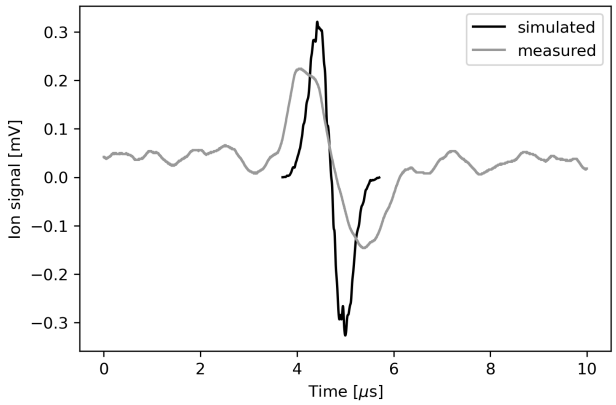

Figure 5.3: The ions passing through the pulsed drift tube induce a bipolar signal as they push and then pull current through the connected line. Here the measured signal is compared to a simulated signal for a bunch of 10^4 Ar^{16+} ions. The bandwidth of the amplifier (220 kHz) has broadened the measured signal. The simulated signal band is distributed around 1 MHz.

Due to the long path from the last Sikler lens to the trap, precise control of the alignment is necessary. To ensure that the vertical beamline and magnet axes are parallel, a laser source for the window below the kicker-bender is being prepared. As discussed in section 3.5, this will be utilized for the UV laser for hyperfine spectroscopy in bismuth. In the short term, an optical laser visible to the CCD can be mounted to obtain better alignment of the beamline to the magnetic field as well as improve the timing measurements of the FCV's shutter speed.

Finally, as mentioned in 4.1 the alignment of the trap to the magnetic field can be controlled by tuning the position of the FCV. Internally created ions should be used to analyze frequency shifts due to any misalignment to the magnetic field according to 2.25.

5.3 Thermalization of Ion Bunches

5.3.1 Injection energies and precooling

Ions injected from HiTrap are anticipated to have energies in the 100 - 500 eV/q range, even after deceleration in the pulsed drift tube. This is significantly higher than the average energy of ions after electron impact creation in the CT for all but the most intense electron beam settings. Therefore, the cooling techniques used in the CT will likely need to be adapted as resistive cooling is not as effective at higher energies and evaporative cooling is not effective for injected ions at a near uniform energy. HCIs from the HiTrap cooler trap are expected to be relatively cold thanks to sympathetic electron cooling. In this sense they have a relatively narrow distribution of their kinetic energy about the average value, unlike hot creations in the CT which follow a Maxwell-Boltzmann distribution. This allows the possibility for active feedback cooling in the CT as shown in figure 5.4. Active feedback cooling relies on the coherent motion of the center of the ion plasma. The axial trap potential is modulated by the inverse of the signal picked up from the motion, and the cloud's energy is dissipated by the voltage sources of the trap.

At higher energies the stored plasma is gas-like. This means that when cooling a single motional mode of the cloud, energy will transfer slowly from the other modes into the cooled mode. For the axial motion the model of this cooling is exponential on short

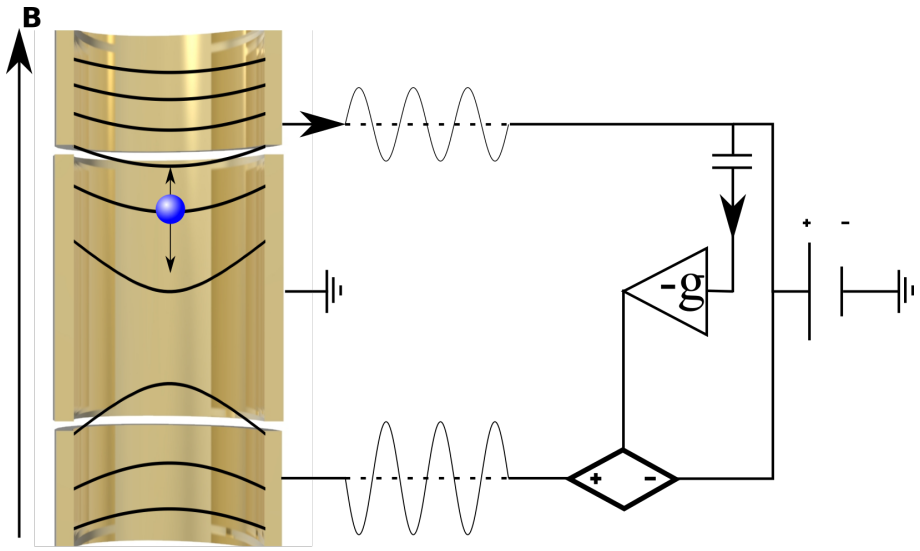

Figure 5.4: A schematic representation of the kind of feedback that could be used for cooling injected ions in the CT. The ion signal detected on the upper endcap is inverted and fed back to the lower endcap with some gain g. The resulting asymmetry of the confining electric field is shown by the contours and results in a net force of the particle toward the trap center.

time scales with time constant given by equation 5.1 when the interactions between ions are weak or all modes are at approximately the same temperature. However, the measured time constant changes on longer time scales as the cloud condenses over time. As the geometry factor is position dependent, as is its curvature, the cooling constant is also dependent on the position of the ion cloud in its orbit. This can vary by orders of magnitude depending on the trap geometry The theoretical cooling constants for a range of positions in the CT is given in [65].

$$\tau = \frac{m}{R_p Q^2}\left(\frac{\partial \Xi}{\partial z}\right)^{-2} \tag{5.1}$$

Here m and Q are the mass and charge of the ion species respectively, R_p is the parallel resistance to the resonator, and Ξ is the geometry factor as defined in section 2.5. To determine the resistive cooling behavior of ions at higher energy than is typically stored in the CT a cloud of ions of mixed charge state was monitored continuously during the first run with the FCV. Following initial creation and evaporative cooling to 60 eV/q the O^{2+} species, being the most abundant for this creation was kept on resonance continuously except for short periods to monitor drifts of the resonator or baseline noise density. Figure 5.5a shows the raw power-in-band measurement from one hour of cooling in this condition. The cooling time constants were determined for each of 4 segments of observation as shown in figure 5.5b.

From the measured time constants the characteristics of the orbit can be determined. The measurements are consistent with an ion cloud in a very large orbit both radially and axially of several mm. Given that the resonant voltage for O^{2+} in the CT is 129 V, the ions have initial axial energies very near the depth of the trap, and the model of harmonic motion breaks down. As the cloud cools and the sizes of the orbits shrink, the rate of cooling approaches more typical conditions, although still much cooling would be needed to reach the usual range of cloud temperatures. The frequency distribution of the ions is quite broad at this energy (wider than the resonator) so sweeping the trap voltage could improve the cooling time. This relies less on the interactions of the ions to cool species which are off-resonance. In addition, the resonator quality was limited for this run to $Q \approx 400$ so significant improvement could also be made in the cooling time by restoring the detection system to its previous quality, which increases the induced current across the parallel resistor. Nonetheless given the injection energies, this demonstrates that active precooling will likely be needed to match the resistive cooling times that were previously recorded in the CT [61]. While the models for particle cooling work well for traps with small numbers of charges or individual species, these extreme conditions are less well understood. More information about cooling large ion clouds is available in [114] and for electron clouds in [73].

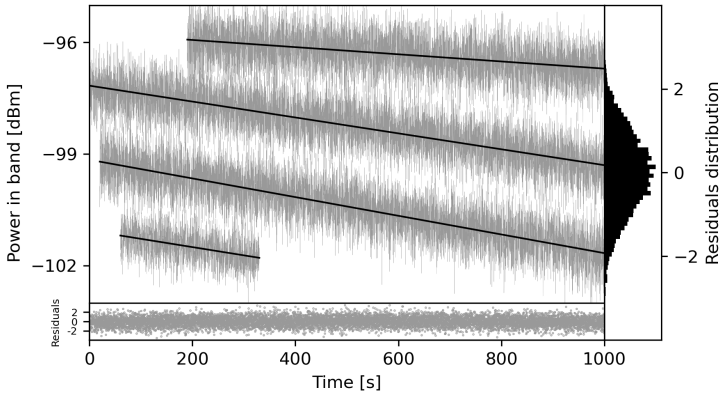

(a)

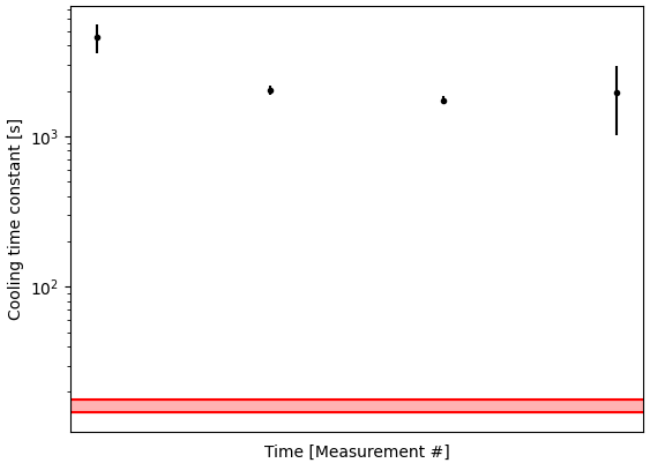

(b)

Figure 5.5: (a) the raw data from a hot ensemble of O^{2+} ions as it is resistively cooled. Four measurements were recorded over about one hour with references before each. Linear fits to the data are also shown along with the residuals for run 2. (b) extracted cooling time constants for each of the four runs. The red bar indicates the expected cooling constant for very low curvature of the geometry factor.

5.3.2 Cooling of dense ion clouds

Additional analysis of the cooling behavior of ions used for subsequent pressure measurements is presented here as indication of the environmental conditions of the stored ions in the setup with the FCV. In the first run with the FCV, measurements were performed in a mixed ensemble of primarily oxygen and nitrogen ions with a background of argon of several charge states and likely also carbon. These background charge states are not resolved in the q/m spectra for this run. This relatively large ion cloud prevented effective estimation of the pressure due to the strong internal interactions and long cooling time. The ions cooled continuously throughout the measurement time for pressure determination, which combined with the observed storage time of only some 20 or so hours made precise measurements impossible. However, this allowed some additional investigation into the behavior of dense ion clouds. Due to the high density, reheating of the axial mode by coupling to the radial modes was observed during pauses in precooling.

Figure 5.6 shows a portion of one of the collected spectra of oxygen and nitrogen during the first run with the FCV. The dominant peaks are O^{6+} and N^{5+} which were the highest produced charge state of each element based on the electron beam energy, utilizing the large gap between electron shells. In addition the Lorentzian distributions of each peak were extracted independently as shown by the dotted curves. The relative abundance of nitrogen in air compared to oxygen leads to the broadening of the nitrogen peak, even though both species are in thermal equilibrium. This is confirmed by investigation of the ion signals over time which indicate a contemporaneous transition of both species into a liquid-like state. Figure 5.7 shows this effect as a discontinuity of the ions' signal widths at the phase transition. This behavior for ion clouds of significant density was explored in detail in [61].

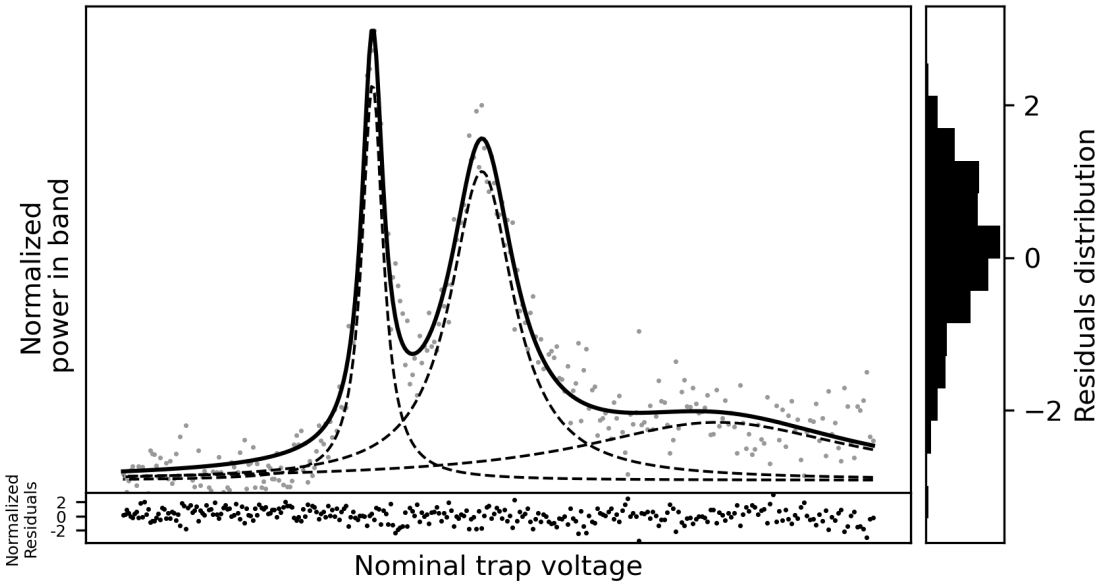

Figure 5.6: Example of the mass spectrum fit used for ion lifetime analysis. The O^{6+} (left) and N^{5+} (middle) peaks can be seen on top of a wide background of multiple unresolved Ar charge states which peaks around Ar^{14+}. The global fit is shown by the solid black line and the individual contributions by dashed lines.

5.3.3 Cooling of sparse ion clouds

In the second run a pure N^{4+} ion cloud was prepared with a low ion density. This was done with very short pulses of the FEP (2 ms) for each creation. The cloud was then cleaned of all other ion species by SWIFT. Figure 5.8 shows the portion of the spectrum around N^{4+} with the fit for the ion peak. The extracted peak widths and positions from each mass spectrum are shown in figure 5.9. At each step of the trapping potential, the power in

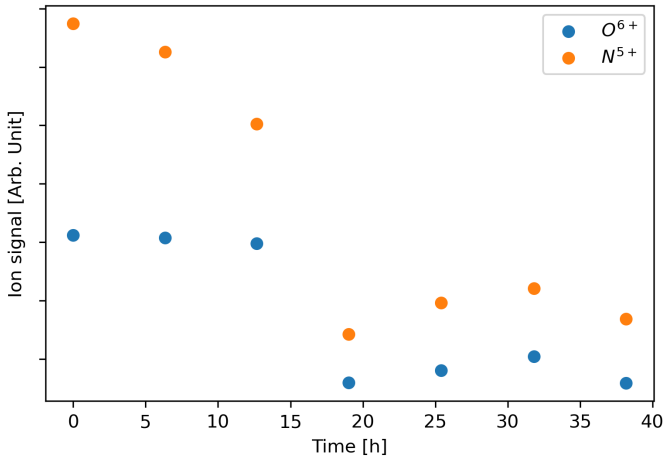

Figure 5.7: The extracted individual ion signals for O^{6+} and N^{5+} are shown over time. The discontinuity around 18 hours is likely due to a phase transition of the ion plasma to a more highly correlated state.

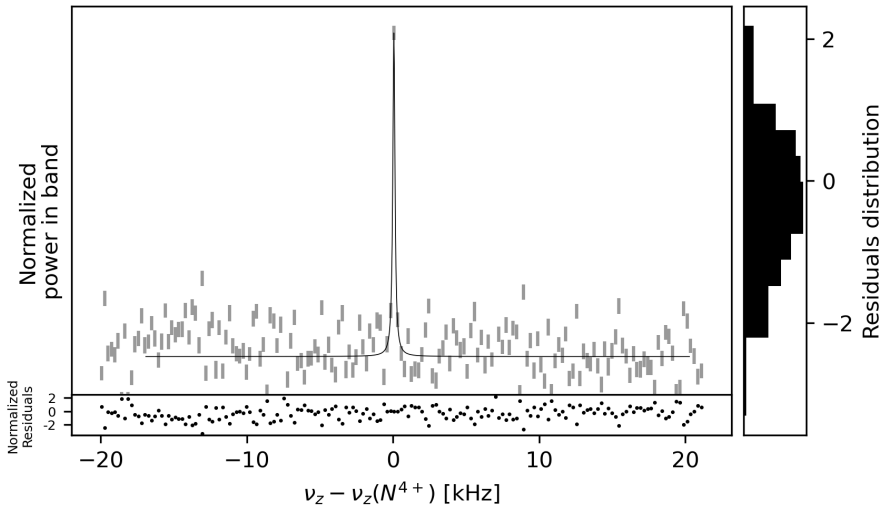

Figure 5.8: Example of Lorentzian fit to a pure, sparse N^{4+} spectrum. The gray bars are the $1-\sigma$ distribution of power-in-band measured at each trap potential and the black line is a fit to the data.

the measurement band (300 Hz) is measured for 400 ms. The nitrogen ions appear as an increase of the measured power in just a single voltage step after cooling.

The cooling of the ion cloud is indicated by the narrowing of the peak width, while the increase of the peak position in terms of the trap depth indicates an increasingly dense ion cloud and therefore increasing plasma frequency. As cooling progresses the peak narrows to the same width as the measurement steps, and the fit gains a large covariance of χ^2 to the center and width of the fitting function. In this case the uncertainty of the extracted parameters is taken as the measurement step size. The fact that cooling was observed to approach equilibrium in just a few cycles gives a good indication of effective cooling time on the order of minutes based on the cycle time and the resonator quality for this run. This is higher than the ideal value even for the reduced quality of the resonator. The

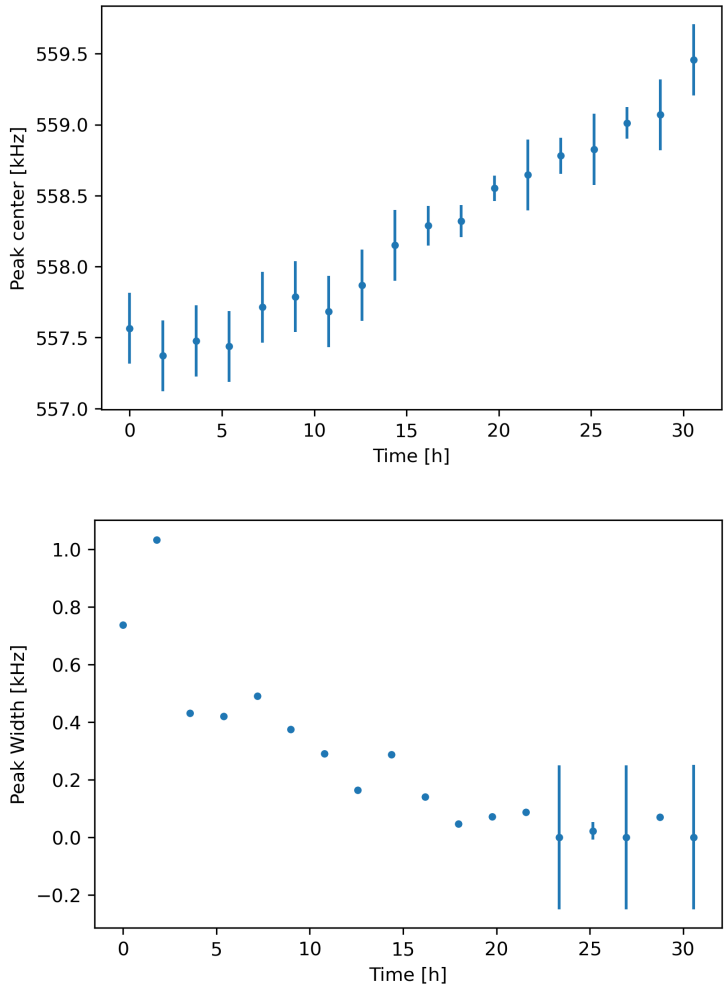

Figure 5.9: (a) the extracted center position of the ion signal peak and (b) its width. The narrowing width indicates cooling to equilibrium which is corroborated by the increasing position of the resonance in terms of trap depth which indicates a stronger shift of the plasma frequency and increasing ion density. Note that the uncertainty is dominated by the variance of the fit, which diverges for measurements of a single value above the noise floor. In this case the step size is taken as the uncertainty instead.

slower cooling is caused by heat transfer to the axial motion from the radial modes due to internal interactions of the cloud, which is also responsible for the stochastic fluctuations of width measurements at these low ion numbers. No phase transition is detected, which is consistent with a small number of trapped ions such that the critical density was not reached. A density of over 1 million N^{4+} ions per cubic centimeter is needed to approach a phase transition at 4 K. Moreover, the lower charge state reduces the strength of internal interactions compared to the study of mixed states.

5.4 Ion Lifetime Measurements

In most cases, the lifetime of ions inside ARTEMIS is limited by the interactions with the background gas. When using the old gas injection system, the residual pressure varied significantly over time as buildup of Ar gas from repeated injections formed layers of cryosorbed atoms, but pressures around 10^{-15} mbar were routine. With the FCV it is

expected that the residual gas pressure will now be even better than before. This is because the initial evacuation through the FCV aperture is improved over the old cryovalve, and leakage through the FCV should also be lower. Determining the background pressure with the new setup is critical as it will be the ultimate limit on the time that heavy HCIs from GSI will be available for measurement within the experiment. The residual gas pressure is estimated by storing a cooled ion ensemble for an extended time and observing the loss of the ion signal as they interact with the background gas atoms. In some cases, this includes a corresponding increase in the next-lower charge state. Measurements are presented for both the old injection system with the cryovalve before installing the FCV and in the current setup.

5.4.1 Pressure measurements with argon injection

The measurements with the old system are useful for comparison with results using the FCV. Presented here is a measurement made near the end of the experimental run immediately before installing the FCV. With the old cryovalve, gas would cryosorb to the walls with each injection of Argon, which would result in reduced vacuum over time. Because the data was collected at the end of an experimental run, it demonstrates the charge exchange effect most readily with an estimated pressure of $3.40(34)\text{x}10^{-14}$ mbar. In this case a pure Ar^{11+} cloud was prepared by electron impact ionization inside the trap, purified by SWIFT and resistively cooled in 21 cycles over 4 hours. After preparation of the ion cloud, q/m spectra were collected approximately every 6 hours. The resulting spectra are shown in figure 5.10a, vertically offset according to the time of measurement. The initial Ar^{11+} peak can be clearly seen around 60 V. Over time this evolves into a spectrum of multiple charge states with the Ar^{10+} peak matching the 11+ peak after 20 hours.

The amplitudes were extracted by fitting the global spectrum as a collection of Lorentzian distributions for each charge state. The amplitudes of the 10+ and 11+ peaks are plotted against time in figure 5.10b with fits to the expected time dependent behavior of the charge-exchange decay, equations 5.2. Here N_{i11+} is the initial population of Ar^{11+}.

$$\begin{aligned} N_{11+} &= N_{i11+} e^{\frac{-t}{\tau_{11+}}} \\ N_{10+} &= N_{i11+} \frac{\tau_{10+}}{\tau_{11+} - \tau_{10+}} \left(e^{\frac{-t}{\tau_{11+}}} - e^{\frac{-t}{\tau_{10+}}} \right) + N_{i10+} e^{\frac{-t}{\tau_{10+}}} \end{aligned} \tag{5.2}$$

The two fits give similar lifetimes: $\tau_{11+} = 20(2)$ hr from the decay of Ar^{11+}, $\tau_{11+} = 20.3$ hr from the growth of Ar^{10+}, and $\tau_{10+} = 17.4$ hr from the decay of Ar^{11+}. However, only the fits to the decay of Ar^{11+} are controlled. The variance of the fitting parameters

in the population of Ar^{10+} show signs of underfitting, as there are only six data points and four free parameters. Using the cross section for single charge exchange with molecular hydrogen from [70] for Ar^{11+} : $10.55(40)\text{x}10^{-15}$ cm^2 the pressure is $P = 3.40(34)\text{x}10^{-14}$ mbar.

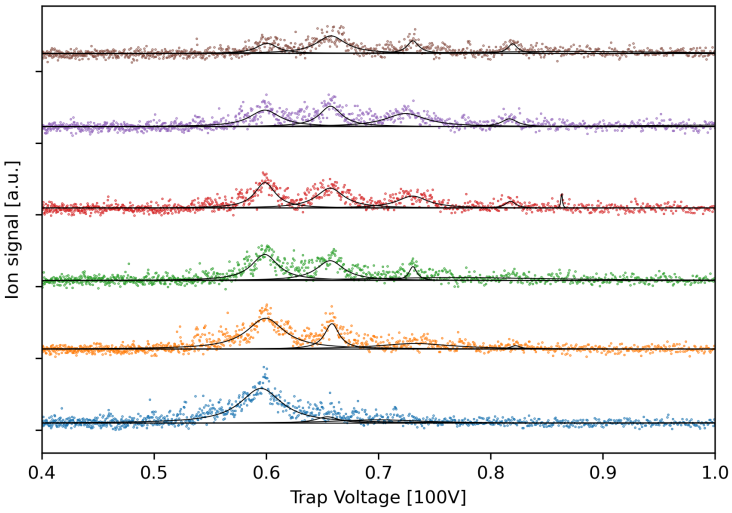

(a)

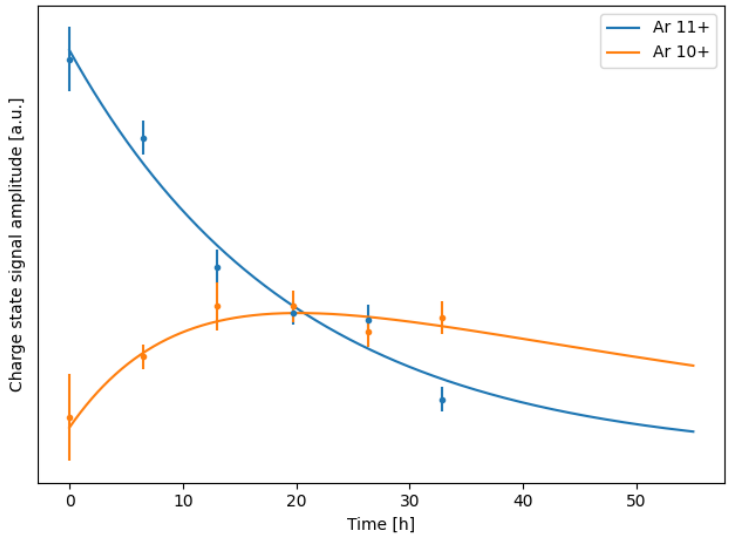

(b)

Figure 5.10: Mass spectra collected for pressure estimation with the old injection system. (a) shows the individual spectra with fits to each peak. They are stacked vertically with the initial scan at the bottom. (b) shows the extracted amplitudes of the Ar^{11+} and Ar^{10+} and fits according to equation 5.2.

5.4.2 Pressure measurements with the FCV

Pressure measurements with the FCV were limited by the detection system which appears to have reduced quality from multiple thermal cycles as well as spurious peaks in the frequency spectrum caused by temperature dependent feedback in the amplifier. The presented measurement was performed in the second run with a pure N^{4+} ion cloud. It was prepared with a very short pulse of the electron beam in an attempt to limit the size of the cloud which had prevented pressure measurements in the first run as explained above. After creation the charge state was isolated by SWIFT and resistively cooled for 5 hours. 19 spectra were collected over 34 hours. Although the signal of the N^{4+} charge state decays exponentially over the run, no N^{3+} appears above the noise floor. This can be explained as further cooling of ion cloud which had not demonstrated any phase transition, which is in turn an indication of a relatively low ion density.

Given that the minimum energy of the ions is in equilibrium with the environment, collisions cannot up-scatter the ions, and daughter charge states from charge exchange interactions are at most the same temperature as the N^{4+} cloud. Therefore the expected signal from the 3+ charge state is 3/4 that of the parent state. This places an upper limit on the creation of the N^{3+} charge state for a given noise floor. At the 99% confidence level the ratio of N^{3+} to N^{4+}:

$$\frac{N_{N3+}}{N_{N4+}} < \frac{3\sigma}{\frac{3}{4}\Sigma_{N4+}}, \tag{5.3}$$

where σ is the standard deviation of the noise floor in the region about the expected N^{3+} peak and Σ_{N4+} is the N^{4+} peak height. That is to say that a population of N^{3+} ions above this threshold would be distinguishable from the noise floor. For the collected spectra the value is between 0.0019 and 0.0031. This is primarily limited by the distribution of noise which is not normally distributed due to temperature related feedback in the amplifier. Figure 5.11 compares the distribution of power-in-band in the region about each charge state for spectra with well distributed noise and with amplifier fluctuations. The 4+ peak is visible as an outlier in all distributions but no peaks are visible in the 3+ region. Thus confidence in the absence of the 3+ peak is high, but the upper limit on the ratio of N^{3+} to N^{4+} ions could be improved with less noise. Amplifier stability also limited the observation time to about 30 hours as the noise peak eventually overlapped with the ion cloud and confinement was lost. Therefore, this limit could also be improved with longer observation time.

Taking the upper value as a conservative limit on the relative population of N^{3+} ions, the pressure can be determined by considering the probability of a single N^{4+} undergoing

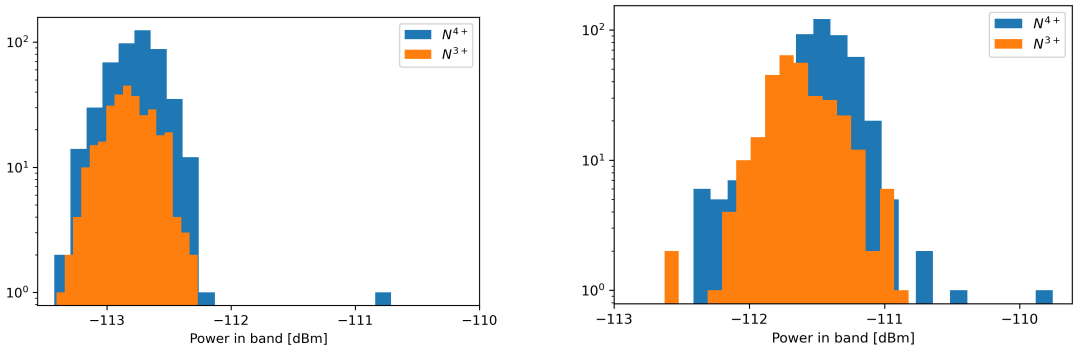

Figure 5.11: Histograms of the measured power-in-band about the region of the N^{3+} and N^{4+} peaks. The color indicates the frequency region. The large peak is the noise distribution and ions appear as outliers to the right of the peak. (left) shows a spectrum with well distributed noise with a stable amplifier. (right) shows the same in the presence of amplifier instabilities. In all spectra the 4+ peak is clearly visible as an outlier but none showed any indication of a significant population of N^{3+} ions.

charge exchange in time Δt:

$$\mathcal{P} = \frac{\langle v \rangle \Delta t}{\ell} = \frac{N_{N3+}}{N_{N4+}}$$
$$\ell = \frac{1}{n\sigma} \tag{5.4}$$

which is then equal to the proportion of N^{3+} ions created. Here $\langle v \rangle$ is the expected ion velocity and ℓ is the mean free path in terms of the residual gas molecular density, n, and charge-exchange cross section, σ. The cross section is estimated by the Müller-Salzborn formula (section 2.4.6) with a molecular hydrogen background as, $5.59\text{x}10^{-15} cm^2$. Although as discussed in section 2.4.6 this may significantly overestimate the cross section. Therefore a more stringent limit could be placed with better data for the interaction cross section for low interaction energies. The mean velocity can be conservatively determined from the equilibrium temperature of the environment.

The maximum proportion of N^{3+} ions created by charge exchange in Δt can then be used to extract the pressure by treating the background gas as ideal.

$$P < \frac{RT}{\langle v \rangle \Delta t \sigma} \frac{N_{N3+}}{N_{N4+}} = 2.37\text{x}10^{-16} \text{ mbar} \tag{5.5}$$

5.4.3 Amplifier instability

In order to determine the source of the amplifier instability, measurements of the frequency spectrum without ions were collected for several days. The most prominent feature was an additional set of peaks just above the resonator frequency. These *intruder* peaks

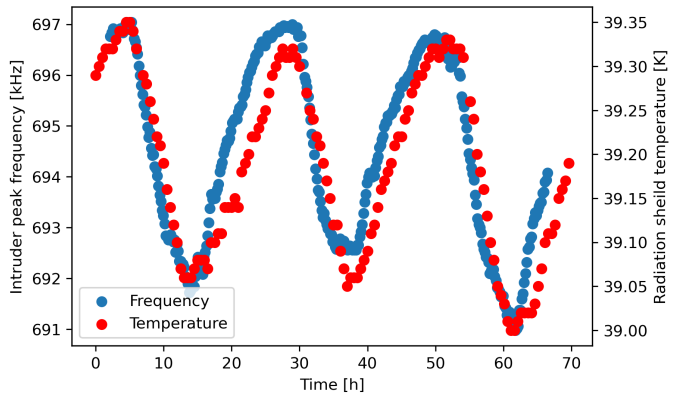

Figure 5.12: Comparison of the amplifier feedback resonance with temperature.

were observed without biasing the first gate of the amplifier as well as without any room-temperature amplification, leaving only the buffer stage of the amplifier and connected components as possible sources. It was also observed that the peaks could be removed temporarily by briefly grounding all of the pins on the electrical vacuum feedthrough for the amplifier. This indicates a possible feedback resonance within the amplifier's buffer stage.

Moreover the center frequency of this intruder resonance was found to correlate well with temperature, showing day night cycles similar to the experimental temperature measurements. Figure 5.12 shows the temperature of the radiation shield and the intruder peak center frequency during these measurements. Given the higher temperatures of the experiment during the second run of the FCV one might expect such fluctuations of the amplifier performance; however a closer investigation of the signal shows significantly higher covariance of the intruder frequency with the temperature of the radiation shield than of the experimental electronics:

$$\begin{aligned} Cov(T_{Shield}, \nu_{intruder}) &= 153 \\ Cov(T_{Elec.}, \nu_{intruder}) &= 48.8 \end{aligned} \tag{5.6}$$

This indicates a thermal link was caused somewhere between the shield stage of the cold head and the amplifier. Specific effort is made to ensure good grounding of the amplifier to the resonator housing and the amplifiers have shielding covers which are also thermally grounded. Therefore the most likely thermal short is between the cable shielding of the output signal and the radiation shield. In the future, the effect of passing the shields of the signal-out line of the amplifiers through the thermocouples of the 4 K stage should be investigated. As this instability was the limit on the lifetime measurement, elimination of the source would allow the determination of a more stringent limit on the pressure in the trap chamber.

Chapter 6

Conclusion and Outlook

This work represents the most recent major upgrades of the ARTEMIS experiment and its current progress toward commissioning of the full operation for measuring magnetic moments in heavy highly charged ions. It presents two main contributions: a detailed description of the changes to the apparatus is given with remarks on the continuing work and next steps, and the trapping conditions after the upgrade are validated by measurements with trapped ions. Until now the experiment has relied entirely on creation of ions by electron impact ionization of gas directly inside the trap chamber. The capabilities of the experiment have grown significantly with access to injection from the SPARC EBIT as well as the HITRAP decelerator facility. Future studies in ARTEMIS will be able to utilize the widened range of highly charged atomic species from external injection or utilize the preexisting internal creation mechanism for simple access to trapped HCIs. Finally, the upcoming beamtime at GSI, E130, will send Bi^{82+} ions to ARTEMIS, which would not be possible without these upgrades.

In chapter 4 a full description of the design of the new beamline at ARTEMIS is presented as well as discussions about its current limitations and possible further upgrades in the future. The final design that is presented was the result of several iterations of simulations of the various components, but realization of the design presents new possibilities for improvement. Nonetheless the initial design requirements have been realized according to the simulations and results with injected and trapped ions are expected in the near future.

The most critical component introduced was the fast-opening cryogenic valve (FCV), which enables the possibility of laser-microwave double-resonance (LMDR) measurements in the ultraviolet range required for measurements in Bi^{82+}. It is the only known valve that can be opened on millisecond time scales and maintain a pressure inside the trap chamber better than $2.4\text{x}10^{-16}$ mbar at less than 10 K. The implementation of the FCV

has increased the monolayer saturation time of cryosorbed gases in the trap chamber of ARTEMIS by more that four orders of magnitude with typical usage. In addition, the concept for a position sensitive non-destructive detector for monitoring ion bunch injection conditions was demonstrated with simulations, which verify that it meets the requirements to properly tune the injection parameters. The design for the active ion optics elements, a decelerating pulsed drift tube and two Sikler lenses, were also verified to meet the requisite injection conditions. The entire design was ensured to allow independent operation of ARTEMIS as well as the low-energy beamline of HiTrap, and fail-safes were implemented to protect the sensitive components.

Chapter 5 presents the first results for ion storage inside the upgraded apparatus and the first results from attempted injection into the trap from the SPARC EBIT. Consistency between the expected conditions inside the trap and the observed impacts on stored ion ensembles indicates a reliable low-noise, cryogenic, ultra-high vacuum environment. This was verified with tests in high ion density conditions as expected for LMDR spectroscopy as well as sparse ion clouds that give the most precise results for non-destructive image current detection. Measurements in dense clouds showed cooling to a critical density to induce a phase transition, where the interaction strength between the trapped ions increases suddenly. This is demonstrated by a sudden shift of the distribution of oscillation frequencies of the trapped ions. Both measurements were limited by the current detection system. Parallel upgrades to the detection system by Kanika [67] should allow more rigorous determination of the conditions in the near future.

The next steps for the ARTEMIS project should aim for successful injection of ions from the SPARC EBIT into the trap chamber. Some specific recommendations related to this work are:

- The third experimental run with the FCV should determine if any further adjustments are needed to bring the ultimate temperatures into the 6 K range. This would primarily come from introduction of more MLI foil on any still uncovered surfaces, particularly those which are non-cylindrical around the adapter for the FCV shutter.
- The beam monitor should be implemented co-axially with the FCV and trap chamber. This will give another diagnostic for injection tuning and ensure that the beam is parallel when entering the long drift region.
- After repair of the downstream Sikler lens, the optimized parameters for injection should be determined with help from the simulation and beam monitor.
- The apertures of the beamline should be aligned with an optical laser and target masks on the vacuum chambers. Although not strictly necessary as steering into

the apertures is not precluded by the magnetic field, this would ease injection significantly.

- The profile of the beam in the horizontal portion of the low-energy beamline should be determined. The apertures of the Sikler lenses are relatively small compared to the components in the horizontal beamline. Therefore significant improvement of the transmission into the middle section of the vertical beamline could be made by ensuring the beam is well controlled before the bender. This will also reduce the elongation of the beam in the bender, further improving transmission. Introduction of an MCP in the ARTEMIS diagnostic chamber could also be useful for more careful tuning of the components of the horizontal beamline.

- Finally, the position of the trap relative to the magnetic field should be verified using trapped ions. Precise determination of the misalignment and position of the peak field strength can be made from the corresponding frequency shifts. The FCV can then be adjusted accordingly.

At the conclusion of this work, the other essential upgrades for LMDR measurements in Bi^{82+} are already underway. Also, the final necessary components for completing the measurement in Ar^{13+} are being implemented. It is foreseen that a precise measurement of high-order Zeeman splitting in Ar as well as the first measurements of electron magnetic moments in a heavy ions will be achieved in the near future.

Appendix A

Optimized beamline parameters

During the second attempt at injection of ions from the SPARC EBIT into ARTEMIS, the ion beam current was maximized on the ARTEMIS Faraday cup. The various voltages applied to components of the low-energy beamline were recorded for the optimal settings at that time in table A.1. Here the channel name begins with either EBIT or TRX which indicates the beamline section as described in 3.5. Then follows an alphanumeric code to indicate the specific component with letters defining the type of element, and subunits are number in increasing order of the path of the ions: L for (segmented) einzel lens, QD for quadrupole doublet, EU for benders (quadrupole or spherical), mpl for another design of einzel lens, or MK for kicker. A final letter or number indicates either a steering direction or specific electrode for segmented components. For example EBITL2r is the second lens after extraction from the EBIT and steers the beam toward the right, TR6EU2C2C4 designates the correction elements for electrodes 2 and 4 in the the quadrupole bender in TR6, and TR722u indicates the bottom (*Ger: unten*) electrode of the second element of the second quadrupole doublet in TR7.

Table A.1: The optimized electrostatic potentials for steering Ar^{16+} ions from the EBIT into the vertical beamline. After the EBIT, TRX indicates the beamline section as in section 3.1.1. A description of each channel is also given for reference.

Channel Name	Channel description	Channel voltage
EBITL1new	EBIT extraction lens 1	1800
EBITL2u	EBIT extraction lens 2 with steering	1320
EBITL2d		1200
EBITL2r		1280
EBITL2l		1160
TR6QD51	Quadrupole doublet 6-5 focusing	100
TR6QD52		160
TR6QD53		120
TR6QD54		130
TR6QD5hSt	Quadrupole doublet 6-5 steering	100
TR6QD5vSt		50
TR6EU2E2E4	Quadrupole bender with correction	4000
TR6EU2C2C4		3750
TR7mpl31	Einzel lens	2200
TR7QD17q11	Quadrupole doublet 7-1 focusing	90
TR7QD17q12		90
TR7QD17q13		75
TR7QD17q14		75
TR7QD21h	Quadrupole doublet 7-2 1st stage	40
TR7QD21v		0
TR7QD22l	Quadrupole doublet 7-2 2nd stage	60
TR7QD22r		60
TR7QD22o		60
TR7QD22u		60
TR7QD31h	Quadrupole doublet 7-2 1st stage	0
TR7QD31v		0
TR7QD32l	Quadrupole doublet 7-2 2nd stage	50
TR7QD32r		50
TR7QD32o		50
TR7QD32u		50
TR7MK11	Kicker	375
TR7MK12		375
TR7EU11	Spherical bender	465
TR7EU12		449

List of Figures

List of Tables

Bibliography

[1] R. Feynman. *QED: The Strange Theory of Light and Matter*. Princeton University Press, 1985. ISBN: 9780691083889.

[2] X. Fan, T. Myers, B. Sukra, and G. Gabrielse. Measurement of the Electron Magnetic Moment. *Physical Review Letters*, 130(7):071801, feb 2023. doi:10.1103/physrevlett.130.071801.

[3] ATLAS Collaboration. Evidence for light-by-light scattering in heavy-ion collisions with the ATLAS detector at the LHC. *Nature Physics*, 13(9):852–858, Aug. 2017. doi:10.1038/nphys4208.

[4] A. H. Compton. The magnetic electron. *Journal of the Franklin Institute*, 192(2):145–155, 1921. ISSN 0016-0032. doi:https://doi.org/10.1016/S0016-0032(21)90917-7.

[5] G. E. Uhlenbeck and S. Goudsmit. Spinning Electrons and the Structure of Spectra. *Nature*, 117(2938):264–265, Feb. 1926. doi:10.1038/117264a0.

[6] A. Landé. Über den anomalen Zeemaneffekt (Teil I). *Zeitschrift für Physik*, 5(4): 231–241, Jul. 1921. doi:10.1007/bf01335014.

[7] W. Pauli. Exclusion Principle and Quantum Mechanics. *Nobel Lecture*, 1946.

[8] P. A. M. Dirac. The Quantum Theory of the Electron. *Proc. R. Soc. Lond*, A: 610–624, 1928.

[9] H. A. Bethe. The Electromagnetic Shift of Energy Levels. *Phys. Rev.*, 72:339–341, Aug. 1947. doi:10.1103/PhysRev.72.339.

[10] F. Sauter. Über das Verhalten eines Elektrons im homogenen elektrischen Feld nach der relativistischen Theorie Diracs. *Zeitschrift für Physik*, 69(11-12):742–764, November 1931. doi:10.1007/bf01339461.

[11] W. Heisenberg and H. Euler. Consequences of Dirac Theory of the Positron. *Zeitschrift Physik*, 2006. doi:10.48550/ARXIV.PHYSICS/0605038.

[12] J. Schwinger. On Gauge Invariance and Vacuum Polarization. *Phys. Rev.*, 82:664–679, Jun. 1951. doi:10.1103/PhysRev.82.664.

[13] V. Hannen, J. Vollbrecht, Z. Andelkovic, C. Brandau, A. Dax, W. Geithner, C. Geppert, C. Gorges, M. Hammen, S. Kaufmann, K. König, Y. A. Litvinov, M. Lochmann, B. Maaß, J. Meisner, T. Murböck, R. Sánchez, M. Schmidt, S. Schmidt, M. Steck, T. Stöhlker, R. C. Thompson, C. Trageser, J. Ullmann, C. Weinheimer, and W. Nörtershäuser. Lifetimes and g-factors of the HFS states in H-like and Li-like bismuth. *Journal of Physics B: Atomic, Molecular and Optical Physics*, 52(8): 085003, Apr. 2019. doi:10.1088/1361-6455/ab0ef0.

[14] T. Aoyama, T. Kinoshita, and M. Nio. Revised and improved value of the QED tenth-order electron anomalous magnetic moment. *Physical Review D*, 97(3): 036001, feb 2018. doi:10.1103/physrevd.97.036001.

[15] D. L. Moskovkin, N. S. Oreshkina, V. M. Shabaev, T. Beier, G. Plunien, W. Quint, and G. Soff. g-factor of hydrogenlike ions with nonzero nuclear spin. *Phys. Rev. A*, 70:032105, Sept. 2004. doi:10.1103/PhysRevA.70.032105.

[16] H. Dehmelt. New continuous Stern-Gerlach effect and a hint of "the" elementary particle. *Zeitschrift für Physik D Atoms, Molecules and Clusters*, 10(2-3):127–134, Jun. 1988. doi:10.1007/bf01384846.

[17] W. Quint, D. L. Moskovkhin, V. M. Shabaev, and M. Vogel. Laser-microwave double-resonance technique for g-factor measurements in highly charged ions. *Phys. Rev. A*, 78:032517, Sep. 2008. doi:10.1103/PhysRevA.78.032517.

[18] D. von Lindenfels, M. Vogel, W. Quint, G. Birkl, and M. Wiesel. Half-open Penning trap with efficient light collection for precision laser spectroscopy of highly charged ions. *Hyperfine Interactions*, Nov. 2013. doi:10.1007/s10751-013-0961-z.

[19] T. Aoyama, M. Hayakawa, T. Kinoshita, and M. Nio. Tenth-Order QED Contribution to the Electron $g-2$ and an Improved Value of the Fine Structure Constant. *Phys. Rev. Lett.*, 109:111807, Sep. 2012. doi:10.1103/PhysRevLett.109.111807.

[20] X. Fan, G. Gabrielse, P. W. Graham, R. Harnik, T. G. Myers, H. Ramani, B. A. Sukra, S. S. Wong, and Y. Xiao. One-Electron Quantum Cyclotron as a Milli-

eV Dark-Photon Detector. *Physical Review Letters*, 129(26):261801, dec 2022. doi:10.1103/physrevlett.129.261801.

[21] W. Quint and M. Vogel, Editors. *Fundamental Physics in Particle Traps*. Tracts in Modern Physics. Springer, 2014. doi:10.1007/978-3-642-45201-7. ISSN 0081-3869.

[22] T. Beier. The g_j factor of a bound electron and the hyperfine structure splitting in hydrogenlike ions. *Physics Reports*, 339(2):79–213, 2000. ISSN 0370-1573. doi:https://doi.org/10.1016/S0370-1573(00)00071-5.

[23] J. Schwinger. On Quantum-Electrodynamics and the Magnetic Moment of the Electron. *Phys. Rev.*, 73:416–417, Feb. 1948. doi:10.1103/PhysRev.73.416.

[24] NIST. The NIST Reference on Constants, Units, and Uncertainty., 2018. URL `https://physics.nist.gov/cgi-bin/cuu/Value?alph|search_for=fine+structure+constant`. *CODATA value: Fine-structure constant.* Retrieved: 2022-Sept-16.

[25] G. Soff, I. Bednyakov, T. Beier, F. Erler, I. Goidenko, U. Jentschura, L. Labzowsky, A. Nefiodov, G. Plunien, R. Schützhold, and S. Zschocke. Effects of QED and Beyond from the Atomic Binding Energy. *Hyperfine Interactions*, 132:75–103, Jan. 2001. doi:10.1023/A:1011977217302.

[26] V. M. Shabaev, D. A. Glazov, G. Plunien, and A. V. Volotka. Theory of Bound-Electron g-Factor in Highly Charged Ions. *Journal of Physical and Chemical Reference Data*, 44(3):031205, September 2015. doi:10.1063/1.4921299.

[27] V. M. Shabaev, D. A. Glazov, M. B. Shabaeva, V. A. Yerokhin, G. Plunien, and G. Soff. g-factor of high-Z lithiumlike ions. *Phys. Rev. A*, 65:062104, Jun. 2002. doi:10.1103/PhysRevA.65.062104.

[28] V. M. Shabaev and V. A. Yerokhin. Recoil Correction to the Bound-Electron g-Factor in H-Like Atoms to All Orders in αZ. *Phys. Rev. Lett.*, 88:091801, Feb. 2002. doi:10.1103/PhysRevLett.88.091801.

[29] U. D. Jentschura, A. Czarnecki, K. Pachucki, and V. A. Yerokhin. Mass Measurements and the Bound–Electron g-Factor. *Int.J.Mass Spectrometry*, 2005. doi:10.48550/arxiv.physics/0510049.

[30] A. V. Volotka and G. Plunien. Nuclear Polarization Study: New Frontiers for Tests of QED in Heavy Highly Charged Ions. *Phys. Rev. Lett.*, 113:023002, Jul. 2014. doi:10.1103/PhysRevLett.113.023002.

[31] A. V. Nefiodov, G. Plunien, and G. Soff. Nuclear-Polarization Correction to the Bound-Electron g-Factor in Heavy Hydrogenlike Ions. *Phys. Rev. Lett.*, 89:081802, Aug. 2002. doi:10.1103/PhysRevLett.89.081802.

[32] N. Michel, J. Zatorski, N. S. Oreshkina, and C. H. Keitel. Nonperturbative analysis of nuclear shape effects on the bound electron g-factor. *Phys. Rev. A*, 99:012505, Jan. 2019. doi:10.1103/PhysRevA.99.012505.

[33] A. S. Varentsova, V. A. Agababaev, D. A. Glazov, A. M. Volchkova, A. V. Volotka, V. M. Shabaev, and G. Plunien. Interelectronic-interaction contribution to the nonlinear Zeeman effect in boronlike ions. *Phys. Rev. A*, 97:043402, Apr. 2018. doi:10.1103/PhysRevA.97.043402.

[34] D. A. Glazov. Zeeman and Hyperfine Splittings in Highly Charged Ions. Seminar, May 2012.

[35] J. C. Berengut, V. A. Dzuba, V. V. Flambaum, and A. Ong. Highly charged ions with $E1, M1, and E2$ transitions within laser range. *Phys. Rev. A*, 86:022517, Aug. 2012. doi:10.1103/PhysRevA.86.022517.

[36] P. G. Thirolf, B. Seiferle, and L. von der Wense. The 229-thorium isomer: doorway to the road from the atomic clock to the nuclear clock. *Journal of Physics B: Atomic, Molecular and Optical Physics*, 52(20):203001, Sept. 2019. doi:10.1088/1361-6455/ab29b8.

[37] T. Beier, H. Häffner, N. Hermanspahn, S. G. Karshenboim, H.-J. Kluge, W. Quint, S. Stahl, J. Verdú, and G. Werth. New Determination of the Electron's Mass. *Phys. Rev. Lett.*, 88:011603, Dec. 2001. doi:10.1103/PhysRevLett.88.011603.

[38] F. A. Jenkins and E. Segrè. The Quadratic Zeeman Effect. *Phys. Rev.*, 55:52–58, Jan. 1939. doi:10.1103/PhysRev.55.52.

[39] W. R. S. Garton and F. S. Tomkins. Diamagnetic Zeeman Effect and Magnetic Configuration Mixing in Long Spectral Series of BA I. *Astrophysical Journal*, 158:839, Nov. 1969. doi:10.1086/150243.

[40] L. I. Schiff and H. Snyder. Theory of the Quadratic Zeeman Effect. *Phys. Rev.*, 55: 59–63, Jan. 1939. doi:10.1103/PhysRev.55.59.

[41] M. Vogel. *Particle Confinement in Penning Traps, An Introduction*. Springer Series on Atomic, Optical, and Plasma Physics. Springer International Publishing, Gewerbestrasse 11, 6330 Cham, Switzerland, 2018. ISBN 331976263X.

[42] I. Arapoglou, A. Egl, M. Höcker, T. Sailer, B. Tu, A. Weigel, R. Wolf, H. Cakir, V. A. Yerokhin, N. S. Oreshkina, V. A. Agababaev, A. V. Volotka, D. V. Zinenko, D. A. Glazov, Z. Harman, C. H. Keitel, S. Sturm, and K. Blaum. g-Factor of Boronlike Argon $^{40}Ar^{13+}$. *Phys. Rev. Lett.*, 122:253001, Jun. 2019. doi:10.1103/PhysRevLett.122.253001.

[43] T. Sailer, V. Debierre, Z. Harman, F. Heiße, C. König, J. Morgner, B. Tu, A. V. Volotka, C. H. Keitel, K. Blaum, and S. Sturm. Measurement of the bound-electron g-factor difference in coupled ions. *Nature*, 606(7914):479–483, Jun. 2022. doi:10.1038/s41586-022-04807-w.

[44] N. Hermanspahn, H. Häffner, H.-J. Kluge, W. Quint, S. Stahl, J. Verdú, and G. Werth. Observation of the Continuous Stern-Gerlach Effect on an Electron Bound in an Atomic Ion. *Phys. Rev. Lett.*, 84:427–430, Jan. 2000. doi:10.1103/PhysRevLett.84.427.

[45] F. G. Major and G. Werth. High-Resolution Magnetic Hyperfine Resonance in Harmonically Bound Ground-State ^{199}Hg Ions. *Phys. Rev. Lett.*, 30:1155–1158, Jun. 1973. doi:10.1103/PhysRevLett.30.1155.

[46] H. F. Beyer and V. P. Shevelko. *Introduction to the Physics of Highly Charged Ions*. Series in Atomic and Molecular Physics. Institute of Physics Publishing, 2003. ISBN 0750304812.

[47] A. Lapierre, U. D. Jentschura, J. R. Crespo López-Urrutia, J. Braun, G. Brenner, H. Bruhns, D. Fischer, A. J. González Martínez, Z. Harman, W. R. Johnson, C. H. Keitel, V. Mironov, C. J. Osborne, G. Sikler, R. Soria Orts, V. Shabaev, H. Tawara, I. I. Tupitsyn, J. Ullrich, and A. Volotka. Relativistic Electron Correlation, Quantum Electrodynamics, and the Lifetime of the $1s^22s^22p^2p^o_{3/2}$ Level in Boronlike Argon. *Phys. Rev. Lett.*, 95:183001, Oct. 2005. doi:10.1103/PhysRevLett.95.183001.

[48] V. Mäckel, R. Klawitter, G. Brenner, J. R. C. López-Urrutia, and J. Ullrich. Laser spectroscopy of highly charged argon at the Heidelberg electron beam ion trap. *Physica Scripta*, T156:014004, Sept. 2013. doi:10.1088/0031-8949/2013/t156/014004.

[49] F. Major, V. Gheorghe, and G. Werth. *Charged Particle Traps*, volume 37 of *atomic, optical, and plasma physics*. Springer, 2005. ISBN 1615-5653.

[50] D. L. Moskovkin, V. M. Shabaev, and W. Quint. g-factor of Li-like ions with a nonzero nuclear spin. *Optics and Spectroscopy*, 104(5):637–649, May 2008. doi:10.1134/s0030400x08050019.

[51] R. S. Van Dyck, P. B. Schwinberg, and H. G. Dehmelt. New high-precision comparison of electron and positron g factors. *Phys. Rev. Lett.*, 59:26–29, Jul. 1987. doi:10.1103/PhysRevLett.59.26.

[52] H.G. Dehmelt. Radiofrequency Spectroscopy of Stored Ions I: Storage*. *Advances in Atomic and Molecular Physics*, 3:53–72, 1968. ISSN 0065-2199. doi:https://doi.org/10.1016/S0065-2199(08)60170-0.

[53] W. Paul and H. Steinwedel. Notizen: Ein neues Massenspektrometer ohne Magnetfeld. *Zeitschrift für Naturforschung A*, 8(7):448–450, Jul. 1953. doi:10.1515/zna-1953-0710.

[54] Nobel Prize Outreach. The Nobel Prize in Physics 1989. *Press Release*, 1989. URL https://www.nobelprize.org/prizes/physics/1989/press-release/.

[55] G. Gabrielse, L. Haarsma, and S. Rolston. Open-endcap Penning traps for high precision experiments. *International Journal of Mass Spectrometry and Ion Processes*, 88(2-3):319–332, Apr. 1989. doi:10.1016/0168-1176(89)85027-x.

[56] M. Kretzschmar. Particle motion in a Penning trap. *European Journal of Physics*, 12(5):240–246, Sept. 1991. doi:10.1088/0143-0807/12/5/010.

[57] G. Gabrielse. The true cyclotron frequency for particles and ions in a Penning trap. *International Journal of Mass Spectrometry*, 279(2):107–112, 2009. ISSN 1387-3806. doi:https://doi.org/10.1016/j.ijms.2008.10.015.

[58] M. Lara and J. P. Salas. Octupolar perturbation of a single ion in a Penning trap. *Phys. Rev. E*, 67:027401, Feb. 2003. doi:10.1103/PhysRevE.67.027401. URL https://link.aps.org/doi/10.1103/PhysRevE.67.027401.

[59] L. Brillouin. A Theorem of Larmor and Its Importance for Electrons in Magnetic Fields. *Phys. Rev.*, 67:260–266, Apr. 1945. doi:10.1103/PhysRev.67.260.

[60] K. Dholakia, G. Z. K. Horvath, D. M. Segal, R. C. Thompson, D. M. Warrington, and D. C. Wilson. Photon-correlation detection of ion-oscillation

frequencies in quadrupole ion traps. *Phys. Rev. A*, 47:441–448, Jan. 1993. doi:10.1103/PhysRevA.47.441.

[61] M. S. Ebrahimi, Z. Guo, M. Vogel, M. Wiesel, G. Birkl, and W. Quint. Resistive cooling of highly charged ions in a Penning trap to a fluidlike state. *Phys. Rev. A*, 98:023423, Aug 2018. doi:10.1103/PhysRevA.98.023423.

[62] L. Schmöger, O. O. Versolato, M. Schwarz, M. Kohnen, A. Windberger, B. Piest, S. Feuchtenbeiner, J. Pedregosa-Gutierrez, T. Leopold, P. Micke, A. K. Hansen, T. M. Baumann, M. Drewsen, J. Ullrich, P. O. Schmidt, and J. R. C. López-Urrutia. Coulomb crystallization of highly charged ions. *Science*, 347(6227):1233–1236, Mar. 2015. doi:10.1126/science.aaa2960.

[63] S. Schmidt, T. Murböck, Z. Andelkovic, G. Birkl, K. König, W. Nörtershäuser, R. C. Thompson, and M. Vogel. Sympathetic cooling in two-species ion crystals in a Penning trap. *Journal of Modern Optics*, 65(5-6):538–548, Jul. 2017. doi:10.1080/09500340.2017.1342877.

[64] D.-F. F. von Lindenfels. *Experimental Studies of Highly Charged Ions in a Penning Trap for the Measurement of Electron Magnetic Moments by Double-Resonance Spectroscopy*. phdthesis, Ruprecht-Karls-Universität Heidelberg, 2015. URL http://www.ub.uni-heidelberg.de/archiv/19835.

[65] M. Wiesel. *Preparation and Investigation of Highly Charged Ions in a Penning Trap for the Determination of Atomic Magnetic Moments*. PhD thesis, Technische Universität Darmstadt, 2017. URL https://tuprints.ulb.tu-darmstadt.de/6280/.

[66] M. S. Ebrahimi. *Non-Destructive Detection and Resistive Cooling of Highly-Charged-Ion Ensembles for Precision Spectroscopy in the ARTEMIS Penning Trap*. phdthesis, Ruprecht-Karls-Universität Heidelberg, 2018.

[67] Kanika. *Studies and Cooling of Highly Charged Ion Ensembles in the ARTEMIS Trap and High-Precision Mass Measurements of* ^{221}Fr, ^{219}Rn, ^{213}Bi, ^{211}Pb, ^{209}Pb, ^{207}Tl *and* ^{207}Pb *at SHIPTRAP*. PhD thesis, Ruprecht-Karls-Universität Heidelberg, 2023.

[68] A. Müller and E. Salzborn. Scaling of cross sections for multiple electron transfer to highly charged ions colliding with atoms and molecules. *Physics Letters A*, 62 (6):391–394, Sept. 1977. doi:10.1016/0375-9601(77)90672-7.

[69] G. Weinberg, B. R. Beck, J. Steiger, D. A. Church, J. McDonald, and D. Schneider. Electron capture from H_2 to highly charged Th and Xe ions trapped at center-of-mass energies near 6 eV. *Physical Review A*, 57(6):4452–4461, 1998. doi:10.1103/physreva.57.4452.

[70] R. Mann. Total one-electron capture cross sections for Ar^{q+} and I^{q+} ions in slow collisions on H_2 and He. *Zeitschrift für Physik D. Atoms, molecules and clusters.*, 3(1):85–90, 1986.

[71] R. E. Olson and A. Salop. Charge-transfer and impact-ionization cross sections for fully and partially stripped positive ions colliding with atomic hydrogen. *Physical Review A*, 16(2):531–541, aug 1977. doi:10.1103/physreva.16.531.

[72] J. D. Jackson. *Classical Electrodynamics 3e*. John Wiley & Sons Inc, Dec. 1998. ISBN 047130932X. URL https://www.ebook.de/de/product/3240907/jd_jackson_classical_electrodynamics_3e.html.

[73] D. J. Wineland and H. G. Dehmelt. Principles of the stored ion calorimeter. *Journal of Applied Physics*, 46(2):919–930, 1975. doi:10.1063/1.321602.

[74] S. Ulmer. *First Observation of Spin Flips with a single Proton stored in a cryogenic Penning trap*. phdthesis, Ruprecht-Karls-Universität Heidelberg, 2011.

[75] Pfeiffer Vacuum GmbH. *The Vacuum Technology Book*. LOTS OF DOTS Media-Group, 2013.

[76] P. J. Gareis and G. F. Hagenbach. Cryosorption. *Industrial & Engineering Chemistry*, 57(5):27–32, 1965. doi:10.1021/ie50665a006.

[77] P. A. Redhead. Extreme high vacuum, 1999.

[78] B. Baudouy. Heat transfer and cooling techniques at low temperature, 2014.

[79] NIST. Therman Expansion of Technical Solids at Low Temperatures. *NBS Monograph 29*, 1961.

[80] D. Rule and L. Sparks. Low-temperature thermal conductivity of composites:Alumina Fiber/Epoxy and Alumina Fiber/PEEK. *NISTIR 89-3914*, 1989.

[81] NIST. Cryogenic technology resources. Website, 2022. URL https://trc.nist.gov/cryogenics/index.html.

[82] P. Bradely and R. Radebaugh. Properties of Selected Materials at Cryogenic Temperatuers. *CRC Press*, 2013. URL https://tsapps.nist.gov/publication/get_pdf.cfm?pub_id=913059.

[83] X. Chu, Z. Wu, R. Huang, Y. Zhou, and L. Li. Mechanical and thermal expansion properties of glass fibers reinforced PEEK composites at cryogenic temperatures. *Cryogenics*, 50(2):84–88, Feb. 2010. doi:10.1016/j.cryogenics.2009.12.003.

[84] W. Lawless. Dielectric and thermal properties of a machinable glass—ceramic at low temperatures. *Cryogenics*, 15(5):273–277, May 1975. doi:10.1016/0011-2275(75)90117-4.

[85] G. Nunes. Thermal contraction of ultrahigh vacuum materials for scanning probe microscopy from 300 to 4 K. *Journal of Vacuum Science & Technology B*, 13(3): 1063, May 1995. doi:10.1116/1.587905.

[86] Erice. Materials properties at low temperature. CERN Accelerator School, 2013.

[87] R. Gans. *Zeitschrift für Technische Physik*, 18:41, 1937.

[88] M. M. Elkind. Ion Optics in Long, High Voltage Accelerator Tubes. *Review of Scientific Instruments*, 24(2):129–137, Feb. 1953. doi:10.1063/1.1770640.

[89] U. Timm. Zur Bereschnung elektrostatischer Linsen. *Zeitschrift für Naturforschung*, 10a:593, 1955. URL https://zfn.mpdl.mpg.de/data/Reihe_A/10/ZNA-1955-10a-0593.pdf.

[90] P. Grivet. Chapter 4 - The Optical Properties of Electrostatic Lenses. In *Electron Optics (Second Edition)*, pages 85–122. Pergamon, second edition edition, 1972. ISBN 978-0-08-016226-3. doi:https://doi.org/10.1016/B978-0-08-016226-3.50008-X.

[91] M. J. S. D. A. Edwards. *An Introduction to the Physics of High Energy Accelerators*. WILEY, Jan. 1993. ISBN 0471551635.

[92] R. Baartman. Low Energy Beam Transport Design. *CERN Yellow Reports: School Proceedings*, Vol 5:Extraction and Transfer, 2018. doi:10.23730/CYRSP-2018-005.491.

[93] F. Hinterberger. Ion optics with electrostatic lenses, 2006.

[94] GSI. Beschleunigeranlagen. Website, 2022. URL https://www.gsi.de/work/beschleunigerbetrieb/beschleuniger.

[95] J. Ullmann, Z. Andelkovic, C. Brandau, A. Dax, W. Geithner, C. Geppert, C. Gorges, M. Hammen, V. Hannen, S. Kaufmann, K. König, Y. A. Litvinov, M. Lochmann, B. Maaß, J. Meisner, T. Murböck, R. Sánchez, M. Schmidt, S. Schmidt, M. Steck, T. Stöhlker, R. C. Thompson, C. Trageser, J. Vollbrecht, C. Weinheimer, and W. Nörtershäuser. High precision hyperfine measurements in bismuth challenge bound-state strong-field QED. *Nature Communications*, 8(1), May 2017. doi:10.1038/ncomms15484.

[96] Z. Andelkovic, F. Herfurth, N. Kotovskiy, K. König, B. Maaß, T. Murböck, D. Neidherr, S. Schmidt, J. Steinmann, M. Vogel, and G. Vorobjev. Beamline for low-energy transport of highly charged ions at HITRAP. *Nuclear Instruments and Methods in Physics Research Section A: Accelerators, Spectrometers, Detectors and Associated Equipment*, 795:109 – 114, 2015. doi:https://doi.org/10.1016/j.nima.2015.05.055.

[97] M. A. Levine, R. E. Marrs, J. R. Henderson, D. A. Knapp, and M. B. Schneider. The Electron Beam Ion Trap: A New Instrument for Atomic Physics Measurements. *Physica Scripta*, T22:157–163, Jan. 1988. doi:10.1088/0031-8949/1988/t22/024.

[98] J. Bernard, J. Alonso, T. Beier, M. Block, S. Djekić, H.-J. Kluge, C. Kozhuharov, W. Quint, S. Stahl, T. Valenzuela, J. Verdú, M. Vogel, and G. Werth. Electron and positron cooling of highly charged ions in a cooler penning trap. *Nuclear Instruments and Methods in Physics Research Section A: Accelerators, Spectrometers, Detectors and Associated Equipment*, 532(1-2):224–228, oct 2004. doi:10.1016/j.nima.2004.06.049.

[99] F. Herfurth, T. Beier, L. Dahl, S. Eliseev, S. Heinz, O. Kester, C. Kozhuharov, G. Maero, and W. Quint. Precision measurements with highly charged ions at rest: The HITRAP project at GSI. *International Journal of Mass Spectrometry*, 251 (2-3):266–272, apr 2006. doi:10.1016/j.ijms.2006.02.012.

[100] S. Bharadia, M. Vogel, D. M. Segal, and R. C. Thompson. Dynamics of laser-cooled Ca^+ ions in a Penning trap with a rotating wall. *Applied Physics B*, 107(4): 1105–1115, Mar. 2012. doi:10.1007/s00340-012-4871-6.

[101] Thorlabs. WTSQ11050-A Datasheet, 2022. URL https://www.thorlabs.de/catalogpages/obsolete/2018/WTSQ11050-A.pdf.

[102] F. Bonaccorso, Z. Sun, T. Hasan, and A. C. Ferrari. Graphene pho-

tonics and optoelectronics. *Nature Photonics*, 4(9):611–622, Aug. 2010. doi:10.1038/nphoton.2010.186.

[103] J. Warbinek, D. Leimbach, D. Lu, K. Wendt, D. J. Pegg, A. Yurgens, D. Hanstorp, and J. Welander. A graphene-based neutral particle detector. *Applied Physics Letters*, 114(6):061902, Feb. 2019. doi:10.1063/1.5080517.

[104] S. Guan and A. G. Marshall. Stored waveform inverse Fourier transform axial excitation/ejection for quadrupole ion trap mass spectrometry. *Analytical Chemistry*, 65(9):1288–1294, May 1993. doi:10.1021/ac00057a029.

[105] M. Shaaban. Master's thesis, TU Darmstadt, 2018.

[106] A. Martin. *Laser Spectroscopic Investigation of Exotic States in Noble Gases*. PhD thesis, Technische Universität Darmstadt, Darmstadt, 2017.

[107] P. Baus. *Forthcoming title*. PhD thesis, Technische Universität Darmstadt, Forthcoming.

[108] C. Smorra, K. Blaum, L. Bojtar, M. Borchert, K. Franke, T. Higuchi, N. Leefer, H. Nagahama, Y. Matsuda, A. Mooser, M. Niemann, C. Ospelkaus, W. Quint, G. Schneider, S. Sellner, T. Tanaka, S. V. Gorp, J. Walz, Y. Yamazaki, and S. Ulmer. BASE – the baryon antibaryon symmetry experiment. *The European Physical Journal Special Topics*, 224(16):3055–3108, Nov. 2015. doi:10.1140/epjst/e2015-02607-4.

[109] S. Sturm, I. Arapoglou, A. Egl, M. Höcker, S. Kraemer, T. Sailer, B. Tu, A. Weigel, R. Wolf, J. C. López-Urrutia, and K. Blaum. The ALPHATRAP experiment. *The European Physical Journal Special Topics*, 227(13):1425–1491, Feb. 2019. doi:10.1140/epjst/e2018-800225-2.

[110] P. S. Yesley. *The Road to Antihydrogen*. PhD thesis, Harvard Universit, 2001.

[111] P. Mandal, G. Sikler, and M. Mukherjee. An einzel lens with a diagonal-slit central electrode to combine steering and focusing of a low energy ion beam. 2010. doi:10.48550/ARXIV.1007.1592.

[112] K. L. Brown and G. W. Tautfest. Faraday-cup monitors for high-energy electron beams. *Review of Scientific Instruments*, 27(9):696–702, sep 1956. doi:10.1063/1.1715674.

[113] J. L. Wiza. Microchannel plate detectors. *Nuclear Instruments and Methods*, 162 (1-3):587–601, jun 1979. doi:10.1016/0029-554x(79)90734-1.

[114] H. Häffner, T. Beier, S. Djekić, N. Hermanspahn, H.-J. Kluge, W. Quint, S. Stahl, J. Verdú, T. Valenzuela, and G. Werth. Double penning trap technique for precise g factor determinations in highly charged ions. *The European Physical Journal D*, 22(2):163–182, feb 2003. doi:10.1140/epjd/e2003-00012-2.

Acknowledgments

What one fool can do, another can too.

Ancient simian proverb
(Silvanus P. Thompson)

As with any endeavor of this kind, it would not have been possible without a chain of support of countless other people, too many to even know, yet I will name a few.

To Wolfgang Quint, I would have neither begun nor completed this project without your trust, guidance, and seemingly endless patience. You have created a beautiful space for the growth of knowledge at ARTEMIS. You encouraged me to try my own ideas and to find their flaws with clear insight and powerful suggestion. I have learned, of course, a great deal about physics from you, but also a great deal more about how to help others learn, and I hope to carry that influence long into the future.

I would especially like to thank Manuel Vogel, who has an encyclopedic knowledge of all things regarding ion trap experiments. You consistently provided the most thoughtful feedback on any writing and ensured that the work of the group was always able to move forward, when it would otherwise seem to be stuck. Thank you for your leadership and encouragement.

Gerhard Birkl was invariably a source of interesting and productive lines of query for our group meetings, and was often able to foresee possible issues before they could occur. He was a familiar and kind presence in many social settings. I thank you for your guiding influence on the ARTEMIS project and your wonderful Christmas parties.

I am grateful to the members of my defense committee who were willing to work with me to make the submission of this work possible. I was fortunate to share some thought provoking conversations with Yuri Litvinov and for his role as a referee of this thesis. It was my pleasure to see Norbert Frank provide excellent undergraduate lectures, which generated an informed and curious cohort of pupils, some of whom I was lucky to tutor. Tilman Plehn very graciously agreed to join the committee on short notice, and I am looking forward to his perspectives on this project.

ARTEMIS is made possible as a part of the atomic physics department at GSI under the efficient leadership of Thomas Stöhlker, as well as a part of the HITRAP project. There are many members of this community I would like to thank for their especially close role with either ARTEMIS or the HITRAP low energy beamline: Zoran Andelkovic, Gleb Vorobjev, Max Horst, and Simon Rausch. I am also thankful for the invaluable support of those who ensure the department keeps running: Tatiana Litvinova, Ömer Güelsever and Nina Bauer. I would like to especially thank Lea Wunderlich, who is an uncanny solver of all kinds of problems, and Davide Racano, without whom many critical components would undoubtedly still be unmade. Finally, I would like to thank the department as a whole for making a welcome environment for students outside of their universities.

Outside of the department, GSI provides support through several groups specializing in electronics, vacuum and cryogenic technology, and manufacturing. I appreciate the special assistance of several people from theses groups that contributed to the final products used in the construction of the beamline: Herald Hahn, Dennis Neidherr, Markus Romig, and Stephan Teich.

I am grateful to the Accelerators Validating Antimatter Innovative Training Network, which was proposed and lead by Carsten Welsch. The project funded a large portion of my work and made it possible for me to join an experiment so far from home. My co-fellows at AVA were always a joy to visit after months of working apart, and I still consider them friends long after the project is complete. I am also thankful to Stefan Ulmer, Stefan Stahl, and Martin Simon who hosted interesting and informative secondments for me as a part of the network.

In particular this work would not have been possible without the foundation laid by the veterans of the ARTEMIS experiment. Zhexi Guo was an excellent boss, and clearly a student of Wolfgang's patience. His attention to detail ensured that ARTEMIS ceased to function as infrequently as possible. Kanika, no colleague could possibly replace you for a midnight dive into detailed discussions regarding ARTEMIS, physics or anything. You have also been one of the most compassionate coworkers I have ever known. This project and ARETMIS as a whole are fortunate to have your contributions and moral support. To the rest of the ARTEMIS team, past present and future, thank you for your contributions and best wishes for continued success: Patrick Baus, Bianca Reich, Arya Krishnan, Manasa Chambath, Khwaish Anjum, Jan Hellmann, Mouwafak Shaaban, Anahita Khodaparast and all the other unnamed teammates I was not so lucky to have worked with directly.

Thank you also to my friends outside of ARTEMIS who made life in Darmstadt and at GSI so enjoyable: Nils Stallkamp, Bela Arndt, Esther Menz, Dimitrios Zisis, Markus

Kiffer, Stefan Ringleb, and anyone who has ever attempted *the challenge*. Life presents so many challenges and the support of my friends made it possible to work though each one of them and learn from them over the last four years. Please know that you will all have an open invitation to visit anytime. I can only hope to support you as well as you have me. My deepest gratitude goes to Tino Morgenroth and his family. You treated my family as your own when we needed it and taught me so much about life in Germany. Your kindness is inspiring. And a special thank you to David Haider and his family, for hosting so many excellent evenings with the most delicious desserts. Secret Agent T, Special Agent N, and Agent Z, you know what you did. Thank you.

Finally, I would never have reached this point without the endless support of my family. To my wife, Michelle Myers, you always push me to be better than I think that I can be, and you don't settle for any excuses. I appreciate the bravery and tenacity you have shown during this adventure. You are such a source of strength, wit, and inspiration to me, that without your partnership I could never have made it this far. To Marilyn and her siblings, I used to think that this was for me, but now I know it was always for you. To my parents, David and Elizabeth Klimes, you have supported this goal resolutely and without hesitation for seventeen years. More than that, you made it possible to dream by the life you provided long before. If I can provide to my own family just a fraction of what you have given to me, it would still only be thanks to you.

Jeffrey William Klimes
Greenwood, IN
13 March, 2023